

Verena Theußl, Bsc.

**Transition Metal Oxides
as Bifunctional Oxygen Catalysts for
Secondary Zinc-Air Batteries**

MASTER'S THESIS

to achieve the university degree of

Diplom-Ingenieurin

Master's degree programme: Technical Chemistry

submitted to

Graz University of Technology

Supervisor

Ass. Prof. Dipl.-Ing. Dr. techn. Waltraud Taucher-Mautner

Institute for Chemistry and Technology of Materials

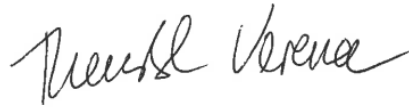
Graz, July 2019

Affidavit

I declare that I have authored this thesis independently, that I have not used other than the declared sources/resources, and that I have explicitly indicated all material which has been quoted either literally or by content from the sources used. The text document uploaded to TUGRAZonline is identical to the present master's thesis.

30th July 2019

Date



Signature

Acknowledgement

Foremost, I would like to express my sincere gratitude to my advisor Waltraud Taucher-Mautner for the continuous support of my master's thesis and research, for the useful comments, remarks and motivation. Her guidance helped me in all the time of research and writing of this thesis. I could not have imagined having a better advisor and mentor for my master's thesis.

Besides my advisor, I would like to thank Brigitte Bitschnau and Franz Mautner for the XRD measurements and data analysis. My sincere thanks also go to Sigrid Wolf, Sandra Steiner, Verena Maier-Mohammed, Daniel Schloffer, Wei Yang and Christian Zelger for the great support and constant advice as well as the great talks and all the fun we had in the last year.

Last but not least, I would like to thank my loved ones, who have supported me throughout the entire process, their continuous encouragement and for their help throughout my years of study and through the process of reasearching and writing this thesis. I will be grateful forever for your love. Thank you!

Zusammenfassung

In dieser Masterarbeit wurden bifunktionelle Katalysatoren (CoMn_2O_4 , MnCo_2O_4) für die Sauerstoffelektrode der sekundären Zink-Luft Batterie hergestellt, sowie ihre elektrochemischen und physikalisch-chemischen Eigenschaften untersucht. Lithium-Ionen Batterien sind die derzeit am häufigsten benutzten Batterien am Markt. Da aber ihre Bestandteile (Lithium, Kobalt) nur sehr gering in der Erdkruste vorhanden sind und insbesondere Lithium hoch reaktiv gegenüber Wasser und Luft ist, sucht man nach einem geeigneten Ersatz. Metall-Luft Batterien, insbesondere Zink-Luft Batterien, sind vielversprechende Kandidaten, um diese zu ersetzen. Die Vorteile der Zink-Luft Batterie sind ihre Umweltfreundlichkeit, die geringen Kosten im Vergleich zur Lithium-Ionen Batterie, sowie ihre hohe theoretische spezifische Energie, da Sauerstoff aus der Umgebungsluft als aktives Material eingesetzt wird. Ungeachtet dieser Vorteile weist diese Batterie noch Verbesserungsbedarf auf, da die Sauerstoffentwicklungs- (OER) und Sauerstoffreduktionsreaktionen (ORR) sehr langsam ablaufen. Dies führt zu hoher Überspannung, und der Einsatz eines Katalysators ist unabdingbar.

Der CoMn_2O_4 Katalysator ist nach zwei verschiedenen Methoden hergestellt worden, der MnCo_2O_4 Katalysator nach einer Methode. Im ersten Syntheseweg wurde der CoMn_2O_4 Katalysator durch die Reduktion von MnO_2 erhalten. Bei der zweiten Methode sind die Katalysatoren (CoMn_2O_4 , MnCo_2O_4) durch Tempern der Zwischenprodukte ($\text{Co}_{0.33}\text{Mn}_{0.67}\text{CO}_3$, $\text{Mn}_{0.33}\text{Co}_{0.67}\text{CO}_3$) hergestellt worden. Die physikalisch-chemischen Eigenschaften der bifunktionellen Katalysatoren wurden mittels XRD, REM/EDX und BET/BJH Messungen untersucht. Für die Charakterisierung der elektrochemischen Eigenschaften wurden die Zyklische Voltammetrie und Linear-Sweep-Voltammetrie (für OER, ORR) in 0.1 M und 8 M KOH verwendet. Dafür wurde der Katalysator auf eine rotierende Scheibenelektrode aufgebracht.

Die XRD-Messungen ergaben, dass es sich um phasenreine Produkte handelt. Die SEM-Messungen zeigten eine plattenartige Morphologie für den CoMn_2O_4 Katalysator und eine mikrosphärenartige Struktur für die nach der zweiten Methode hergestellten Katalysatoren. Bei den BET-Messungen wurde herausgefunden, dass man mit der zweiten Methode viel höhere spezifische Oberflächen als mit der ersten erzielen konnte.

Die Ergebnisse der Zyklischen Voltammetrie (CV) ergaben, dass der Anstieg der Stromdichte im anodischen Bereich auf Grund der Sauerstoffentwicklung erfolgt. Der nach der ersten Methode hergestellte CoMn_2O_4 Katalysator zeigte zusätzlich einen kleinen anodischen Peak. Dieser war auf die Änderung der Oxidationszahl des Kobalts zurückzuführen. Bei den CV-Messungen in 8 M KOH wurden höhere Stromdichten erzielt als in der niedrigeren Elektrolytkonzentration. Die Ergebnisse der OER in 0.1 M KOH zeigten, dass der nach der ersten Methode synthetisierte CoMn_2O_4 Katalysator die höchste Stromdichte erzielen konnte und dass die Katalysatoren, die mit der zweiten Methode hergestellt wurden, die höchste Überspannung aufwiesen. Bei den OER-Messungen in 8 M KOH waren die Überspannungen bei allen drei Katalysatoren ungefähr gleich, und die höchsten Stromdichten erzielte der MnCo_2O_4 Katalysator. Die ORR-Messungen in 0.1 M KOH zeigten, dass die Katalysatoren vom zweiten Syntheseweg niedrigere Überspannungen als der Katalysator nach der ersten Methode hatten. Der MnCo_2O_4 Katalysator konnte wiederum die höchsten Stromdichten erzielen. In der 8 M KOH konnte man keine genaue Aussage über den besten Katalysator treffen, da dies von der Katalysatorbeladung der rotierenden Scheibenelektrode abhing. Grundsätzlich wurden bei den ORR-Messungen in der 8 M KOH aufgrund der geringeren Sauerstofflöslichkeit viel niedrigere Stromdichten als in 0.1 M KOH erzielt. Die Koutecky-Levich Analyse ergab, dass die ORR in 0.1 M KOH über einen vier-Elektronen Mechanismus und in der 8 M KOH über einen zwei-Elektronen Mechanismus abläuft.

Abstract

In this master's thesis, bifunctional catalysts (CoMn_2O_4 , MnCo_2O_4) for the air electrode of secondary zinc-air batteries were synthesized and investigated concerning their physicochemical properties and bifunctional catalytic activities. Lithium-ion batteries are the most used batteries at the moment. A replacement is needed due to the scarcity of lithium and cobalt in the earth crust and in particular, lithium is highly reactive to water and air. Metal-air batteries, especially zinc-air batteries, are promising candidates as replacement. Advantages of the zinc-air battery are its environmental benignity, low costs compared to the lithium-ion battery, as well as its high specific energy, due to the fact that oxygen from the ambient air is taken as active material. Despite of all these advantages, there is still some development needed, due to the slow kinetics of the oxygen evolution- (OER) and oxygen reduction reactions (ORR). This can result in large overpotentials and the use of a catalyst is indispensable.

The CoMn_2O_4 catalyst was synthesized according to two different methods and the MnCo_2O_4 catalyst was prepared with one method. In the first method, the MnO_2 precursor is reduced to obtain the CoMn_2O_4 catalyst. In the second method, the catalysts (CoMn_2O_4 , MnCo_2O_4) were received through annealing of the intermediates ($\text{Co}_{0.33}\text{Mn}_{0.67}\text{CO}_3$, $\text{Mn}_{0.33}\text{Co}_{0.67}\text{CO}_3$). The physicochemical properties of the bifunctional catalysts were obtained by XRD, SEM/EDX and BET/BJH measurements. The electrochemical characterisation methods cyclic voltammetry and linear sweep voltammetry (for OER, ORR) were carried out in 0.1 M and 8 M KOH. The catalyst was applied on a rotating disc electrode (RDE).

The results of the XRD measurements show phase-pure catalyst products. The SEM measurements revealed that CoMn_2O_4 , synthesized with the first method, had a plate-like morphology and the catalysts of the second method are microspheres. By means of the BET measurements, it was determined that much higher specific surface areas were obtained with the second method than with the first one.

In the CV measurements, all three catalysts showed an increase of the anodic current density, which is caused by the OER. The CoMn_2O_4 catalyst synthesized with the first method, showed an additional small anodic peak, which was due to the change of the oxidation state of cobalt. In the CV measurements in 8 M KOH, much higher current densities were obtained than in the lower electrolyte concentration. In case of the OER measurements in 0.1 M KOH, the CoMn_2O_4 catalyst synthesized with the first method achieved the highest current density and the catalysts synthesized with the second method showed the highest overpotential. Concerning the OER measurements in 8 M KOH, all three catalysts reached approximately the same overpotential and the highest current density was achieved by the MnCo_2O_4 catalyst. In case of the ORR in 0.1 M KOH, the catalysts of the second method obtained a lower overpotential. The MnCo_2O_4 catalyst achieved again the highest current density. In 8 M KOH, none of the catalysts clearly outperformed the others, because of the dependence on the catalyst loading. In general, the achieved current densities of the ORR in 8 M KOH are much lower than in 0.1 M KOH, due to reduced oxygen solubility in highly concentrated electrolyte. The results of the Koutecky-Levich analysis in 0.1 M KOH suggest that the ORR mechanism occurs in the four-electron pathway and in the 8 M KOH, the two-electron mechanism is more likely.

TABLE OF CONTENTS

1	INTRODUCTION	1
2	THEORY	3
2.1	Metal-Air Battery	3
2.1.1	Zinc-Air Battery	4
2.1.1.1	Electrolyte.....	6
2.1.1.2	Separator	7
2.1.1.3	Zinc electrode	8
2.1.1.4	Air electrode	9
2.1.1.5	Bifunctional catalysts: CoMn_2O_4 and MnCo_2O_4	11
2.2	Physicochemical Measurements	12
2.2.1	Scanning Electron Microscopy (SEM).....	12
2.2.2	Energy-Dispersive X-ray Analysis (EDX).....	14
2.2.3	X-Ray Diffraction (XRD)	15
2.2.4	Brunauer-Emmett-Teller (BET).....	18
2.2.5	Barrett-Joyner-Halenda analysis (BJH).....	20
2.3	Electrochemical Measurements	23
2.3.1	Potential Sweep Voltammetry	23
2.3.1.1	Linear Sweep Voltammetry (LSV)	24
2.3.1.2	Cyclic Voltammetry (CV).....	25
2.3.2	Rotating disc electrode (RDE)	27
2.3.3	Koutecky-Levich Analysis	29
3	EXPERIMENTAL PROCEDURE	32
3.1	Catalyst Preparation	32
3.1.1	Method 1.....	32
3.1.1.1	Synthesis of amorphous MnO_2	32
3.1.1.2	Synthesis of the nanocrystalline CoMn_2O_4 catalyst.....	33
3.1.2	Method 2.....	33
3.1.2.1	Synthesis of $\text{Co}_{0.33}\text{Mn}_{0.67}\text{CO}_3$ and $\text{Mn}_{0.33}\text{Co}_{0.67}\text{CO}_3$	34
3.1.2.2	Synthesis of spherical CoMn_2O_4 and MnCo_2O_4	35

3.2	Physicochemical Characterisation	35
3.2.1	X-Ray Diffraction (XRD)	35
3.2.2	Scanning electron microscopy (SEM)	36
3.2.3	Energy dispersive X-ray analysis (EDX)	36
3.2.4	Brunauer-Emmett-Teller and Barrett-Joyner-Halenda analysis (BET/BJH)	36
3.3	Electrochemical Characterisation	37
3.3.1	Working electrode preparation	37
3.3.2	Electrochemical Measurements (CV, LSV)	39
3.3.3	Koutecky-Levich Analysis	40
4	RESULTS AND DISCUSSION	41
4.1	Physicochemical characterisation	41
4.1.1	X-Ray diffraction (XRD)	41
4.1.2	Scanning electron microscopy (SEM)	43
4.1.3	Energy dispersive X-ray analysis (EDX)	45
4.1.4	Brunauer-Emmett-Teller (BET) and Barrett-Joyner-Halenda analysis (BJH)	47
4.2	Electrochemical measurements	48
4.2.1	Cyclic Voltammetry (CV)	48
4.2.2	Oxygen Evolution Reactions (OER)	52
4.2.3	Oxygen Reduction Reactions (ORR)	59
4.2.4	Koutecky-Levich Plot	68
5	CONCLUSION	72
6	REFERENCES	75
7	APPENDIX	80

1 Introduction

In the days of global warming and increasing demand in energy as well as an awareness of climate change, a transition from a fossil fuel based to a clean energy economy is needed ¹. The world energy demand is predicted to raise more than a double until 2050 and will be more than a triple until the end of the century ². Nowadays, still over 80% of the total energy supply is obtained from fossil fuels, such as oil, gas and coal. These fossil fuels are causing a dramatic build-up of greenhouse gases in the atmosphere and environmental pollution ³. The so-called “clean energy”, which is generated from renewable resources such as solar or wind, only provides 4% of the electricity production and they are rather intermittent and intrinsically fluctuant, because of their dependence on the weather conditions ^{3, 4}. It is estimated that they will grow by more than 25% until 2030. The conventional power grids will become unstable under those fluctuating conditions, when an imbalance between supply and demand is predominant. The challenge now is to find a proper energy storage system, which is environmentally friendly, has low cost and is capable of storing production surplus and of coping with higher demands ^{2, 4, 5}.

Among the large-scale energy storage technologies, secondary batteries are one of the most efficient, simplest and reliable systems, due to their mechanism of direct conversion from chemical into electrical energy by electrochemical redox processes. They are an excellent energy storage technology for the integration of renewable resources into the power grid because they are operated pollutant-free, have a high round-trip efficiency, a high energy density and a long cycle life ^{3, 6, 7}.

Even though lithium-ion batteries are the most used batteries at the moment, a replacement is needed, due to their high costs and concerns regarding their safety and supply of their components (lithium and cobalt)⁸. Metal-air batteries, especially zinc-air batteries, are promising candidates as replacement because of their high specific energy, which is due to the utilization of their cathode material from the air (O₂) instead of storing heavy active materials as in other battery systems ⁹. Further advantages of the secondary zinc-air batteries are that they are rather inexpensive ($< 10 \text{ \$ kW}^{-1} \text{ h}^{-1}$) ¹, zinc is the most stable metal in aqueous electrolytes, and the second most abundant material in the earth crust as well as its environmental friendliness ⁷.

The main challenges of this type of battery are to find a suitable bifunctional catalyst, which is able to boost both, oxygen evolution-(OER) and oxygen reduction reactions (ORR), as well as the carbonation of the alkaline electrolyte and the short cycle life because of zinc-dendrite growth¹⁰.

The aim of this master's thesis is the development of a promising transition metal oxide catalyst for the air electrode of the secondary zinc-air battery. Three catalysts are synthesized according to two different methods (M1 and M2): CoMn_2O_4 (M1/M2) and MnCo_2O_4 (M2)^{11,12}. For both methods, a precursor is synthesized first. In case of method one, it is an amorphous MnO_2 and in case of method two, carbonate precursors ($\text{Co}_{0.33}\text{Mn}_{0.67}\text{CO}_3$ and $\text{Mn}_{0.33}\text{Co}_{0.67}\text{CO}_3$) are prepared. Then, a reduction reaction (for M1) or annealing (for M2) is carried out to obtain the catalysts. Since the physicochemical properties of the catalyst play a crucial role concerning their activity, x-ray diffraction (XRD) measurements are conducted to obtain the crystal structure. Moreover, the secondary electron microscopy technique with an energy dispersive x-ray analyser (SEM/EDX) is carried out to illustrate the morphology and to analyse the chemical composition. The specific surface area has a great impact on the catalytic activity as well and therefore, Brunauer-Emmett-Teller (BET) measurements are also conducted. The properties of the catalysts concerning their bifunctional activity for the air electrode are examined via cyclic voltammetry and linear sweep voltammetry experiments (for OER and ORR).

2 Theory

2.1 Metal-Air Battery

The development of sustainable electrochemical energy storage devices is more urgent than ever, since the fossil fuel resources on earth are limited. Secondary batteries, especially metal-air batteries, are promising candidates for the transition to a clean energy economy. In general, there are several types of metal-air batteries, primary, reserve and secondary ones. Primary metal-air batteries cannot be recharged after use and secondary batteries are rechargeable. The secondary devices can be further divided into electrically and mechanically rechargeable. In mechanically rechargeable batteries, the discharged metal electrode and the electrolyte are replaced after the discharge process and in principle, they function as a primary battery. The electrically rechargeable battery requires a bifunctional air electrode, which is able to perform both, oxygen reduction and oxygen evolution reaction¹³. Nowadays, the most used batteries are lithium-ion batteries, due to their long cycle life (>5000 cycles) and high energy efficiency (>90%)³. Apart from the advantages, the battery is limited due to its high costs and concerns regarding its safety and the supply of lithium and cobalt (only 20 parts per million of earth crust)^{8,14}. Thus, the research is leading into the direction of alternative rechargeable technologies. Metal-air batteries are promising candidates as replacement for lithium-ion batteries since their theoretical specific energy is extremely high compared to that of other secondary batteries¹⁵ and comparable to the one of gasoline (13000 Wh · kg⁻¹¹⁶), as can be seen in Figure 1.

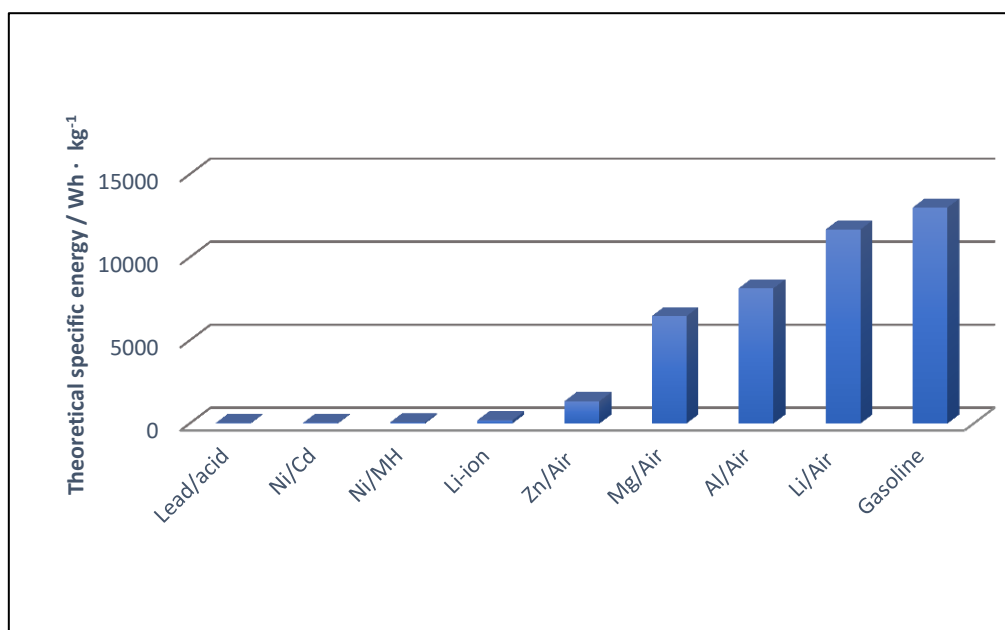


Figure 1: Comparison of the theoretical energy densities of different secondary battery types with gasoline^{16, 17, 18}.

Metal-air batteries generate electricity through a redox reaction between the metal and the oxygen from the air. Due to their open cell structure, the supply of the active material at the cathode is almost infinite. This feature makes them similar to a fuel cell, with the fuel being oxygen. In general, they consist of a metal anode, an air cathode and a separator soaked in ion conducting electrolyte. Metal-air batteries can be classified according to their electrolyte. On the one hand, there are aqueous systems, which are not sensitive to moisture like the zinc-air system, and on the other hand, there are the water-sensitive systems with aprotic electrolytes, such as the lithium-air system. Several metals can be used as anode, including zinc, lithium, aluminium and iron. A promising candidate is lithium since it has the highest theoretical specific energy (11680 Wh kg^{-1})¹⁶ and a high cell voltage (nominal 2.96 V). But in the metallic form it is impaired by its instability if exposed to air and aqueous electrolytes¹⁵ and apart from this, the metal's scarcity and high costs limits the usability. In contrast to aprotic electrolytes, aqueous ones are favoured because of their wide availability, low costs and high ionic conductivity³. Zinc is a promising candidate, because it is the most stable metal in aqueous electrolytes. Further promising features of the zinc metal are its high abundance in the earth crust, its low cost and high specific energy. The largest producers of zinc are China, Peru, Australia and the USA¹⁹. It is the most active material that can be electrodeposited from an aqueous electrolyte, is environmental benign, has a flat discharge curve and a long shelf life to conclude the long list of benefits.^{3, 6, 10, 15, 13, 17, 18, 20}

2.1.1 Zinc-Air Battery

Zinc-air batteries generally consist of four main parts, an air cathode, a zinc metal anode, an alkaline electrolyte and a separator, which is between cathode and anode to prevent a short circuit. The cathode consists of a catalyst coated gas diffusion layer (GDL), as it can be seen in the schematic illustration in Figure 2. During the discharge process, zinc cations are produced (reaction (1)) at the zinc metal electrode and the generated electrons are transferred through an external load to the air electrode.

Atmospheric oxygen diffuses into the air electrode and at the three-phase zone, oxygen is reduced to hydroxide ions via the oxygen reduction reaction (ORR, reaction (4)). The three-phase zone is the interface of the solid (catalyst), liquid (electrolyte) and gaseous (oxygen) components of the battery. Then, the hydroxide ions migrate to the zinc metal electrode through the separator and there, zincate ions (Zn(OH)_4^{2-} , reaction (2)) are formed. If the electrolyte is saturated with zincate ions, zinc oxide (ZnO) precipitates (reaction (3)). The overall reaction can be simply described as zinc combining with oxygen to form zinc oxide (reaction 5). In case of the charging process, the aforementioned electrochemical reactions are reversed. The battery is capable of storing electric energy through the oxygen evolution reaction (OER), which is the backward reaction of reaction (4). This reaction also happens at the three-phase zone where the oxygen leaves the battery via the GDL and zinc deposition occurs^{10, 15, 21}. A schematic illustration of the zinc-air battery can be seen in Figure 2.

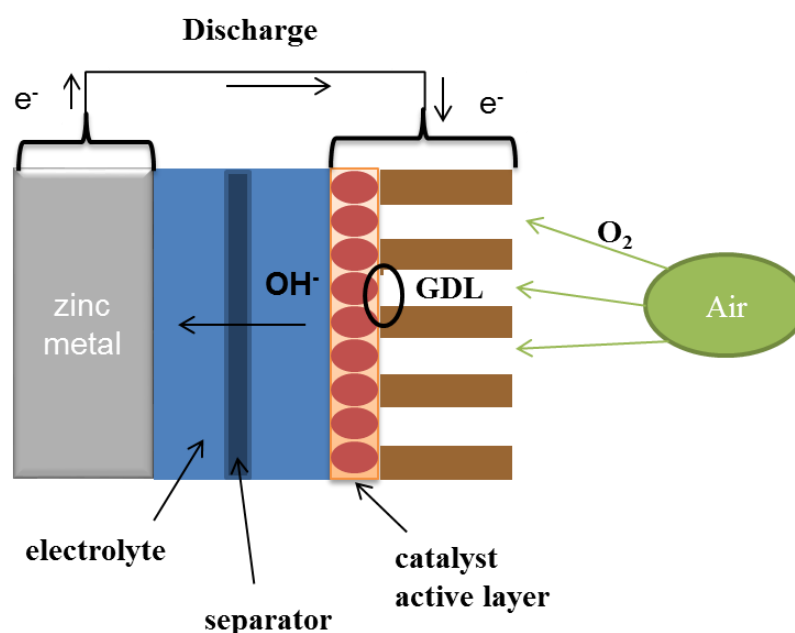
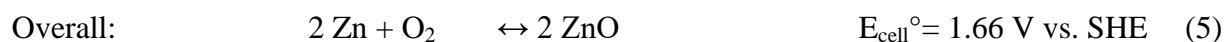
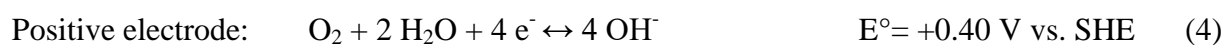
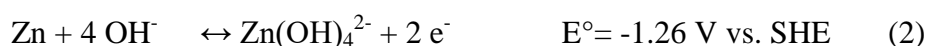


Figure 2: A schematic illustration of the secondary zinc-air battery.¹⁵



2.1.1.1 Electrolyte

The electrolyte is one of the most underestimated components of the secondary zinc-air battery compared to the electrode materials. It can profoundly affect the battery performance in many aspects, such as capacity retention, rate capability and cycling efficiency. In metal-air batteries mostly potassium hydroxide (KOH), sodium hydroxide (NaOH) and lithium hydroxide (LiOH) are used as electrolyte. The most promising one is potassium hydroxide, since it has the lowest viscosity, low cost and superior ionic conductivity (K^+ $73.50 \Omega^{-1} \text{ cm/equiv}$) compared to Na^+ ($50.11 \Omega^{-1} \text{ cm/equiv}$)⁹. Usually, concentrations around 30 wt% KOH or 7 M KOH are used, because at this concentration the electrolyte has its maximum ionic conductivity, the zinc oxide solubility is at its maximum and the zinc corrosion at its minimum. A further impact on the battery performance shows the resistance of the electrolyte. It can be reduced by increasing the electrolyte concentration, but only to a certain point, since a too high concentration causes an increase of the viscosity. The high electrolyte concentration further leads to ZnO formation (according to reaction (3)) and decreases the active surface area of the Zn metal and the battery performance.

Another reason for decreased cell capacity is the sensitivity of the electrolyte against CO_2 . Since the battery is operated with an alkaline solution and exposed to air, carbonates can be formed by the reaction with hydroxyl ions. Those carbonates are formed inside the pores of the air electrode and reduce the lifetime of the air electrode. The blocking occurs because the carbonates are less soluble in potassium hydroxide and the concentration of hydroxyl ions decreases. A further reason to use KOH instead of NaOH, is the higher solubility of the reaction products K_2CO_3 or $KHCO_3$ in the electrolyte compared to their sodium counterparts. Thus, the carbonate precipitation problem is alleviated. An additional cause of performance degradation is the water loss, due to the open system structure. During the operation of the secondary zinc-air battery, a regular filling up with water is required. The gelling of the electrolyte helps to minimize the water loss and enhances battery performance and cycle life. Such gelling agents are hydroponic gels, like agar, and they are able to store solution 20-100 times of their weight¹.

In the last years, also ionic liquids have been proposed and evaluated for zinc-air batteries. They are beneficial for the cyclability of the zinc electrode because they attain dendrite-free zinc deposition. Moreover, they are able to slow down the drying out of the electrolyte, suppress the self-corrosion of zinc as well as eliminate the carbonation problem. Despite all these advantages of ionic liquids, they do not work well with the current air electrode that is designed in particular for aqueous electrolytes. Ionic liquids are too viscous to effectively wet the gas diffusion layer (GDL), which gives rise to a quick voltage decrease in the zinc-air battery during discharge. So far, the best performance of zinc-air batteries is yielded with KOH as electrolyte and could not yet be approached by any aprotic electrolyte ^{1, 7, 10, 15}.

2.1.1.2 Separator

In general, the separator is used as a physical barrier between the electrodes and prevents short circuits. Its characteristics should include stability in strong alkaline electrolytes ($\text{pH} \geq 13$), being inert against redox processes, stability during charging and discharging as well as electrochemical stability within a wide working potential window (≥ 2.5 V). The separator needs an appropriate pore size and porosity to sustain the electrolyte in the pores. Another important characteristic is the high ionic conductivity, allowing OH^- ions to pass. Due to this, most separators are made of polyethylene, polypropylene, polyvinyl alcohol and polyolefin. The porosity of the separator also enables the migration of $\text{Zn}(\text{OH})_4^{2-}$ and this results in a decreased capacity of the cell ^{1, 10, 15}.

2.1.1.3 Zinc electrode

The zinc electrode, which is the anode of the secondary zinc-air battery, is usually made of pure zinc metal. It is one of the most abundant metals in the earth crust, has a low toxicity and is the most active metal, which can be electrodeposited from aqueous electrolytes. Additional characteristics of zinc include low equivalent weight, high specific energy density, its capability of highly efficient recharging and its stability in alkaline media without significant corrosion. The capacity is sustained over long time periods and several hundred charge and discharge cycles. During the charging process, oxidation occurs on the zinc metal and an insulating layer can be formed. Hence, many commercial zinc batteries are using a gelled mixture of granulated zinc powders as electrode material. The zinc granules increase the active surface area and achieve better inter-particle contact and therefore, a better interaction with the electrolyte can be obtained. Furthermore, the zinc granules can lower the internal resistance because of their larger surface area and thus, increases the electrochemical performance.

The performance of a zinc electrode is limited by several phenomena that can occur during the operation: dendrite growth, shape change, passivation and internal resistance as well as hydrogen evolution (Figure 3). Zinc dendrites are sharp, needle-like metallic protrusions which can be formed during the charging processes. The critical factor about dendrites is that they can punctuate the separator and make contact to the positive electrode, which leads to a short circuit. The shape change occurs when zinc is dissolved in the electrolyte during discharge and deposits at a different location on the zinc electrode during charging. This leads to densification of the electrode and loss of usable capacity. In case of the passivation, an insulating layer is formed on the zinc electrode surface, which blocks the migration of the discharge product and/or OH^- ions and therefore, cannot be recharged anymore. The passivation layer consists of precipitated ZnO, which is formed when the electrolyte is saturated with $\text{Zn}(\text{OH})_4^{2-}$,^{1, 10, 15}.

Hydrogen evolution occurs because of its more electropositive potential (-0.83 V vs. SHE) compared to the standard reduction potential of Zn/ZnO (-1.26 V vs. SHE at pH 14). Thus, it is thermodynamically favoured and the zinc electrode starts to corrode. Strategies to decrease the rate of hydrogen evolution are needed to improve the charging efficiency and reduce the rate of self-discharge of the zinc electrode ^{1, 7, 10, 15}.

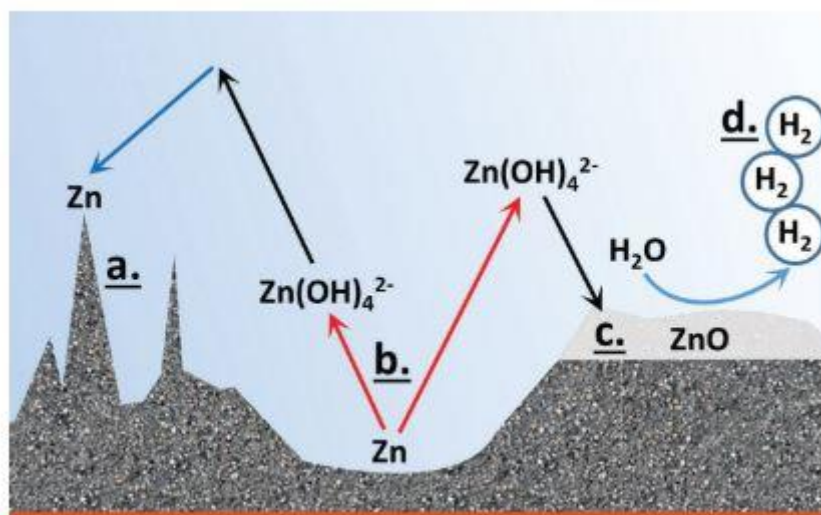


Figure 3: A schematic illustration of the performance-limiting phenomena that can occur on the zinc electrode: a) dendrite formation, b) shape change, c) passivation and d) hydrogen evolution. ¹⁰

2.1.1.4 Air electrode

The air electrode of a secondary zinc-air battery consists of a hydrophobic gas diffusion layer (GDL) and a moderately hydrophilic bifunctional catalyst layer, which are laminated together with a metal grid as a current collector. The catalyst layer of the GDL is very crucial since the electrochemical reactions during the charging and discharging process of the battery (OER, ORR) are in fact both thermodynamically spontaneous but the reaction kinetics are sluggish. Therefore, a bifunctional catalyst which accelerates both reactions is needed.

The oxygen reduction reactions in aqueous solutions may occur by two pathways – the direct 4-electron transfer from O₂ to OH⁻ and the 2-electron path from O₂ via HO₂⁻ to OH⁻ (reactions (6) – (8)).

4-electron process:



2-electron process:



Catalysts, which can promote the ORR through the direct four-electron process, are highly preferred, because oxygen is directly reduced to OH⁻ without the production of peroxide in the solution. Further, the peroxide not only reduces the efficiency of the ORR catalysis but also poisons the catalyst or the carbon support, due to its high oxidizability. The OER (9) involves the reversed process of the ORR, where OH⁻ gets reduced to O₂ and H₂O: ^{1, 10, 22}



The requirements of the electrode materials are stability concerning highly oxidative conditions upon oxygen evolution, as well as strong reducing conditions under oxygen reduction at high current rates. The GDL plays an important role in the performance of bifunctional catalysts, because it is the physical support for the catalyst. It allows the transportation of air to the catalyst, as well as prevents the electrolyte from leaking out and it possesses a high electrical conductivity. Further requirements of the GDL are to be thin and highly porous, to have a high mechanical integrity (with optimum bending stiffness in the case of flexible designs), reliable electrochemical oxidation stability and chemical durability in strong alkaline electrolytes. The hydrophobicity is realized by impregnating the GDL with hydrophobic agents such as PTFE, PVDF and fluorinated ethylene propylene (FEP). The GDL typically consists of carbon materials, such as activated carbon or carbon nanotubes (CNT). ^{1, 10, 15}

2.1.1.5 Bifunctional catalysts: CoMn_2O_4 and MnCo_2O_4

The kinetics of the electrochemical oxygen evolution (OER) and oxygen reduction reactions (ORR) are rather sluggish. Therefore, a bifunctional catalyst is needed in order to boost both. The noble metal oxides of ruthenium (Ru) and iridium (Ir) are excellent OER catalysts and the noble metal platinum (Pt) exhibits a superior activity for the ORR. Since they are noble metals and very expensive and their durability is still far from being satisfied under rechargeable zinc-air battery operation, as well as their scarcity, a replacement is needed. The research has led to the class of earth-abundant transition-metal (e.g. Co, Ni, Mn) oxides and (oxo)hydroxides. These spinel type catalysts are favoured in contrast to precious metals because of their low cost, easy preparation and structural stability. And within these types, the Co- and Mn- based materials have been favoured due to their activity for ORR and OER. Menezes et al.¹² were able to synthesize microspheres of tetragonal CoMn_2O_4 and cubic MnCo_2O_4 spinel. They stated that the octahedral sites of spinels (cubic MnCo_2O_4 phase) favour the OER and the tetrahedral sites of the tetragonal CoMn_2O_4 improves the ORR activity via the four-electron transfer path.

The bifunctional catalysts CoMn_2O_4 and MnCo_2O_4 belong to the structural group of spinels (Figure 4). The name spinel originates from the mineral spinel MgAl_2O_4 and now describes a whole structural group. This group has the general formula AB_2X_4 ²³, where X are mostly the chalcogenides oxygen or sulphur and A (=Mn, Zn, Cd, Co, Cu, Ni, Mg, Fe, etc.) and B (=Al, Cr, Mn, Fe, Co, Ni, Ga etc.) are positive charged metal ions. The metal A occupies every eighth of the centres of tetrahedral coordinated positions (in total 8 out of 64), whereas the octahedral coordinated positions (in total 32) are filled to the half with the metal B and the anion is located at the polyhedral vertexes in case of normal spinels. There is also a second group of spinels, the inversed ones.

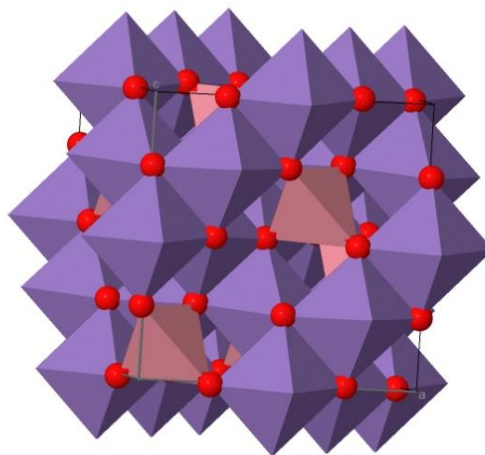


Figure 4: Crystal structure of the CoMn_2O_4 and MnCo_2O_4 catalyst with different octahedral and tetrahedral sites (ICSD⁵⁵)

In this case, the occupation of the metal atoms is changed. The B is located at the tetrahedral coordinated positions and the octahedral positions are occupied by both, A and B. Since the anion X has usually the oxidation state -2, the cation A can be in the +2 or +4 oxidation state and the cation B in the +2 or +3. The cubic unit cell consists of 56 atoms in total, there are 32 anions and 24 cations and it is a conventional fcc unit cell. MnCo_2O_4 is an inverse spinel, in which the Mn shows a preference for the octahedral site. CoMn_2O_4 is a normal spinel^{24, 25, 26}.

2.2 Physicochemical Measurements

2.2.1 Scanning Electron Microscopy (SEM)

The scanning electron microscopy (SEM) is a visualization technique for bulk specimen. It is a valuable tool for the analysis of micro- and nanostructures of surface areas. With this method, visualization of the morphology is possible and information about the topography and the composition of the surface area can be acquired. In contrast to the light microscope, whose resolution is limited to the visible light radiation (400-700 nm), the electron microscope offers an atomic level resolution and only depends on the energy of the electrons. A typical SEM consists of an electron gun, which is the electron source, an anode and electromagnetic lenses for the focusing of the electrons. Furthermore, there is a vacuum chamber, where the specimen holder is located as well as detectors for the collection of the signals emitted from the specimen. Figure 5 is a schematic representation of a typical SEM assembly. The electrons are generated thermionically from a tungsten- or a lanthanum hexaboride (LaB_6) cathode, accelerated towards an anode, and focused by the Wehnelt cylinder as they are accelerated to the anode. Alternatively, they can also be emitted via field emission. Tungsten is used, because it is the metal with the highest melting point and the lowest vapour pressure, which enables the heating for electron emission. The generated electrons are then highly focused to a spot with a diameter of a few nanometres by electromagnetic condenser lenses and then scanned sequentially in a line-by-line manner (“raster”) across the specimen. At each location, where signals are emitted, a detector collects them and synchronizes it with the location and the signal intensity is used to modulate the corresponding pixel image.

The primary electrons of the incident electron beam interact with the specimen, either elastically (no energy is lost) or inelastically (energy is lost). Due to this interaction a variety of signals can be collected including secondary electrons (SE), Auger electrons (AE), backscattered electrons (BSE) and X-rays (Figure 5).

From a volume close to the surface, auger and secondary electrons are emitted. Secondary electrons possess a low energy (3 – 50 eV) and arise as a result of inelastic scattering of the primary electrons with weakly bonded electrons of the outer shells of atoms. In case of the Auger electrons, the excited atom returns to its ground state by donating energy to another electron within the atom, which is then ejected as an Auger electron. X-rays and backscattered electrons are signals, which are emitted from deeper regions of the specimen. Backscattered electrons still have 60% to 80% of their primary energy and thus, they are able to escape from deeper regions. They are generated through elastic scattering of the primary electrons with the sample atoms^{27, 28, 29, 30}.

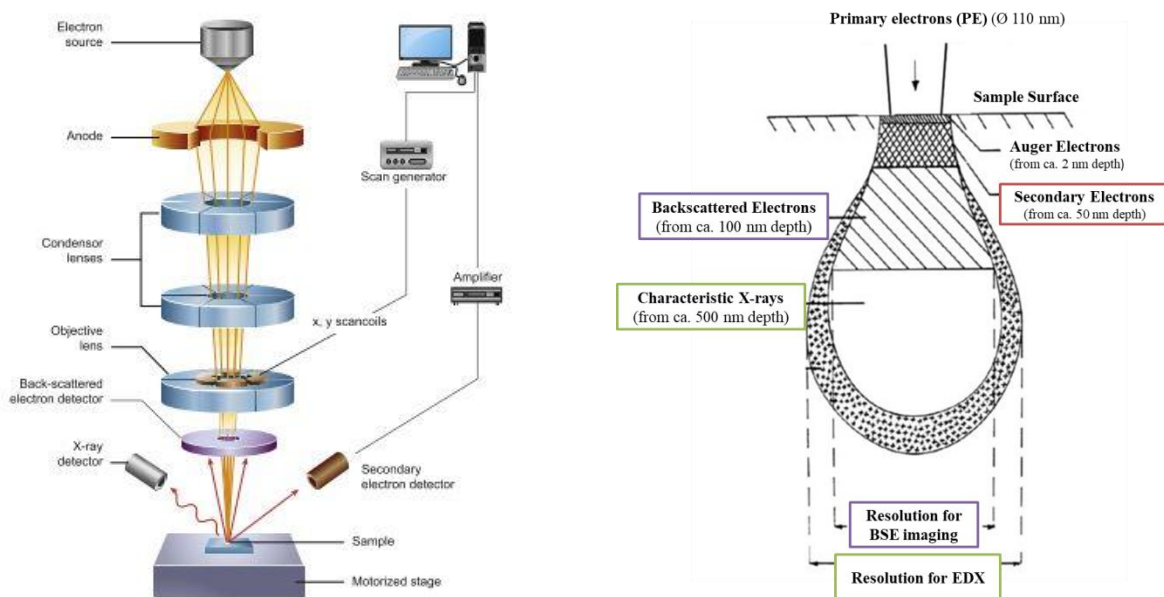


Figure 5: A schematic illustration of a secondary electron microscope (left) and a scheme of the interaction volume of the primary electrons with the specimen (right)^{27, 28}.

2.2.2 Energy-Dispersive X-ray Analysis (EDX)

Scanning electron microscopes often have an energy dispersive x-ray analyser attached, to obtain simultaneously the chemical composition during the examination of the surface area. This technique is known as a microanalysis, since it performs a chemical analysis on a small portion of the sample providing data about the local chemical composition.

The X-rays are generated as the primary beam collides with another electron and removes it from its orbit. Thus results in a vacancy, which is filled by an electron from an outer shell of higher energy and the energy difference is emitted in the form of characteristic X-ray radiation. The energy value of the X-rays is characteristic for each chemical element, electronic shells (K, L, M) and electronic transition (α , β , γ , δ). A typical EDX spectrum is shown in Figure 6. The EDX detectors are based on semiconductor chips that convert X-rays into electron hole pairs, which can form an electrical current. The generated electronic signal is proportional to the energy of the X-rays.^{28, 29, 30}

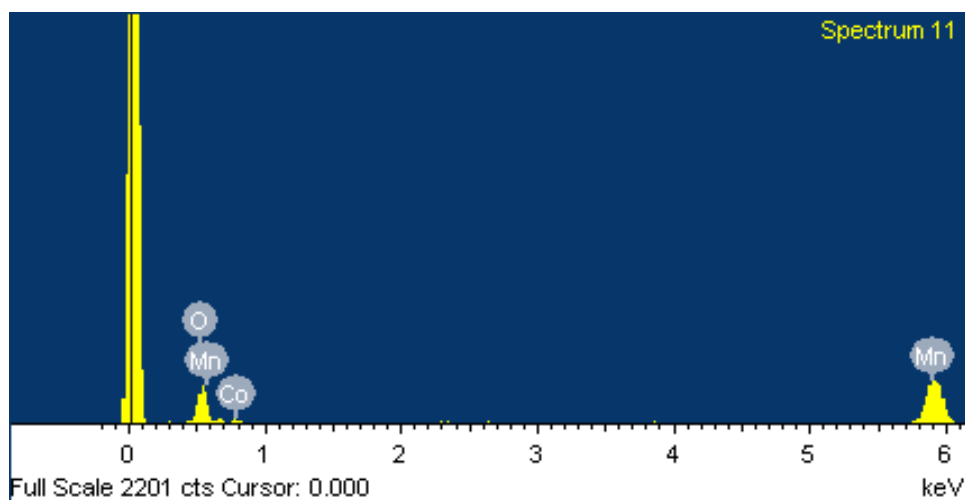


Figure 6: A typical EDX spectrum of the CoMn₂O₄ (M2) catalyst.

2.2.3 X-Ray Diffraction (XRD)

X-ray diffraction is a powerful tool for the determination of chemical composition, space groups, information about crystal structure (atomic positions, temperature factor or occupancy) as well as texture and quantitative and qualitative phase analyses of materials. A crystalline material is a three-dimensional repetition of atoms or molecules. X-rays are electromagnetic waves with wavelengths in the range of 0.01 nm to 1 nm and they are generated through “Bremsstrahlung” or ionization of the material, when electrons hit the target.

These electrons are generated by heating a tungsten filament in a vacuum and are accelerated through a high potential field into the direction of a target. “Bremsstrahlung” is emitted, when the accelerated electrons are decelerated on the target and parts of the kinetic energy is transformed into X-rays. In case of the second effect, the impinged atom ejects electrons from inner shells and those from outer ones “jump” into these gaps. The energy difference between the electron energies of the inner shell and the one of the incoming electron is emitted in form of photons. These photons have a characteristic energy, which depends on the initial and final shell position of the electrons and on the material (Figure 7)³¹. Since through the emitting of the radiation a lot of heat (up to 3 kW) is produced, the anode has to be cooled with water on the back³². A schematic illustration of a X-ray tube can be seen in Figure 7³³.

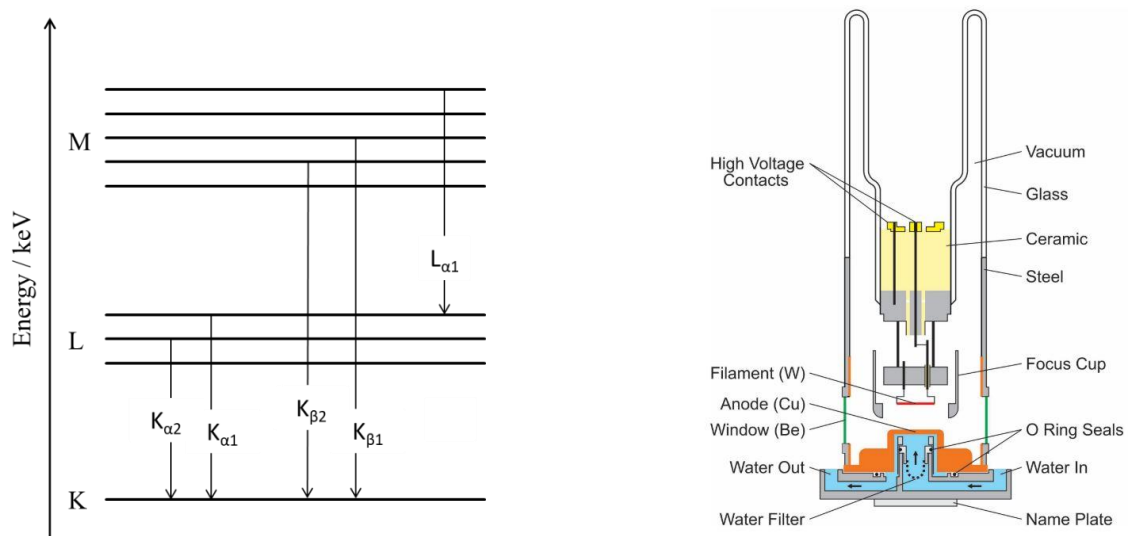


Figure 7: An illustration of the atomic energy levels according to the emission of characteristic X-ray radiation (left) and a schematic illustration of the setup of a X-ray tube (right).

In XRD methods, only the characteristic radiation with the highest intensity is used, the $K\alpha$ radiation. Thus, to remove the remaining radiation, a filter or a monochromator is used. The monochromatic radiation is then focused on the crystalline material and either constructive or destructive interference occurs.

The easiest way to describe the principle of X-ray diffraction, which is a reflection of X-rays by sets of lattice planes, is with the Bragg equation. Lattice planes are crystallographic planes, which are characterized by the Miller indices (hkl). Parallel planes have the same indices and are separated by the distance d_{hkl} . In the Bragg analysis, X-rays are seen as visible light being reflected by the surface of a mirror, which are the lattice planes of the crystal. Since the X-rays penetrate deep inside the material, diffraction occurs at several consecutive parallel planes at the same time. The way of the second wave (Figure 8) is longer than the one of the first wave and if the difference (Δs) between them is an integer multiple of the wavelength, constructive interference occurs. The difference of the path of the two waves depends on the angle of incidence and the distance d . With the help of geometric considerations, the following equation can be stated:

$$\Delta s = 2 * d * \sin\theta \quad (10)$$

It is twofold, because the wave has a longer way before and after the diffraction. Since the condition of a constructive interference also has to be valid, Δs needs to be an integer multiple of the wavelength, and the combination of the two conditions results in the Bragg equation:

$$n * \lambda = 2 * d * \sin\theta \quad (11)$$

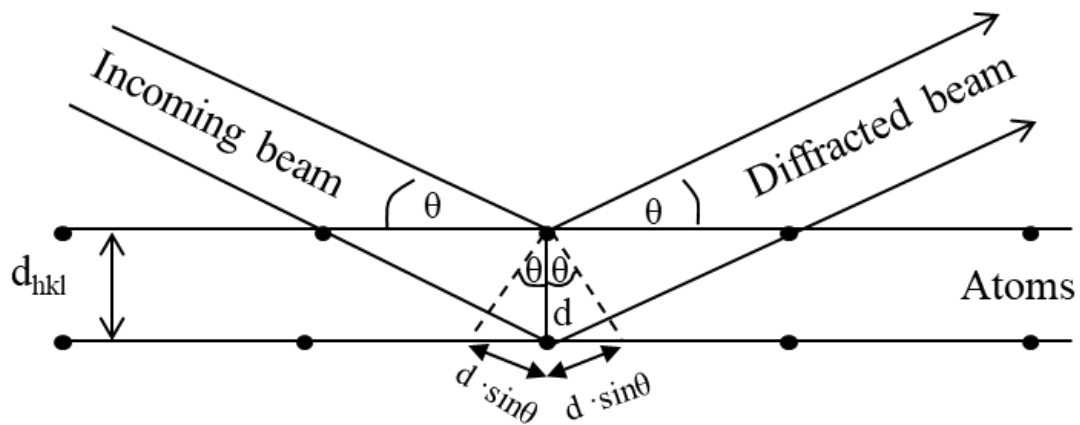


Figure 8: Geometrical illustration for the derivation of the Bragg equation.

The resulting diffraction data can then be used to make a diffractogram, where the intensity is plotted against the 2θ angle and before that, the background needs to be subtracted. In Figure 9, the diffractograms of an amorphous and a crystalline material are plotted. The crystalline material (which has periodically spaced atoms) has well-defined peaks at particular scattering angles, whereas the amorphous material (whose atomic structure is close to that of a liquid) shows an intensity maximum that spans several degrees 2θ ^{31, 32, 33, 34}.

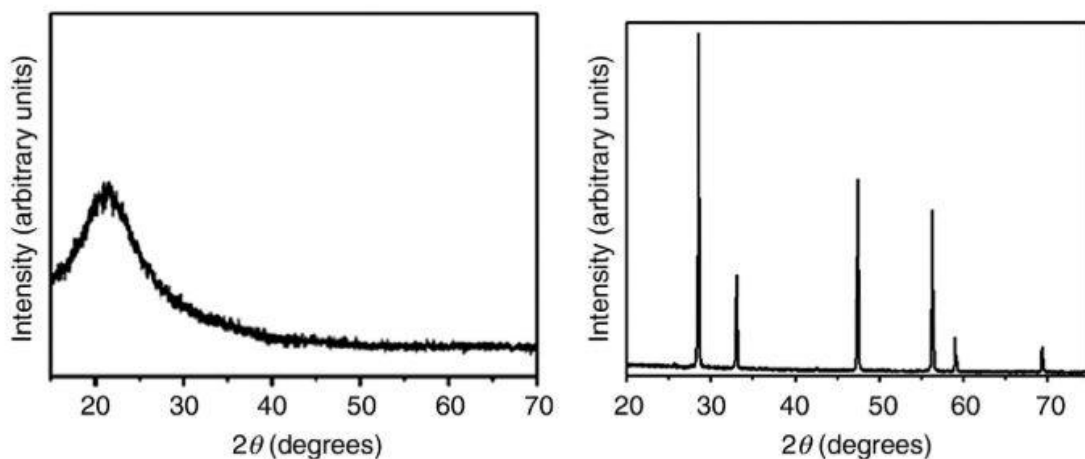


Figure 9: X-ray diffractograms of an amorphous material (left) and a crystalline material (right).

2.2.4 Brunauer-Emmett-Teller (BET)

The Brunauer-Emmett-Teller method (BET) is the most used method for acquiring information about the surface area of porous and finely divided materials ³⁵. The specific surface area (SSA) has a great impact on the catalytic activity of the catalyst, because it determines how much oxygen can be adsorbed. The higher the SSA, the better is the catalytic activity ³⁶. The surface area can be increased through decreasing of particle size like grinding and milling. Negative impacts on the particle size have high temperature processes like melting. The SSA can be determined by physical adsorption of gas (N₂, Ar, Kr) on the surface of the solid and the adsorbed amount of gas corresponding to a monomolecular layer on the surface can be calculated. There are two different types of adsorption: chemical and physical. In case of the chemical adsorption, also called chemisorption, chemical bonds are formed, whereas the physisorption involves weak van der Waals forces.

Several experimental determined adsorption isotherms can be distinguished depending on the physicochemical interactions. The five major types, according to IUPAC ³⁷, are plotted in Figure 10. The adsorption isotherm of type I is called Langmuir and the one of type II is the S-shaped or also sigmoidal-shaped called isotherm. The other types (type III – V) are unnamed ³⁸. The type I isotherms are related to microporous solids, which have relatively small external surfaces, like some activated carbon, molecular sieve zeolites and certain porous oxides. Type II isotherms are reversible and unrestricted multilayers of physical adsorption on nonporous (aluminium) or macroporous solids. After the adsorption of the monolayer, a further increase in partial pressure results in extensive adsorption and a multilayer coverage is obtained. In case of the type III isotherms, the adsorbent-adsorbate interactions are weak and results in clustered adsorbed molecules around the most favourable site on the surface of a nonporous or macroporous solid. Type IV is similar to type II, which has an inflection (or knee) at the monolayer formation. This adsorption isotherm occurs in mesoporous adsorbents like many oxide gels, industrial adsorbents and mesoporous molecular sieves. And in case of type V isotherms, commonly observed for flat, homogenous adsorbents, the adsorbate interacts with the monolayer instead of the adsorbent surface due to the lower heat of adsorption. Those isotherms are useful for the prediction of the gas sorption properties ^{35, 36, 37, 39}.

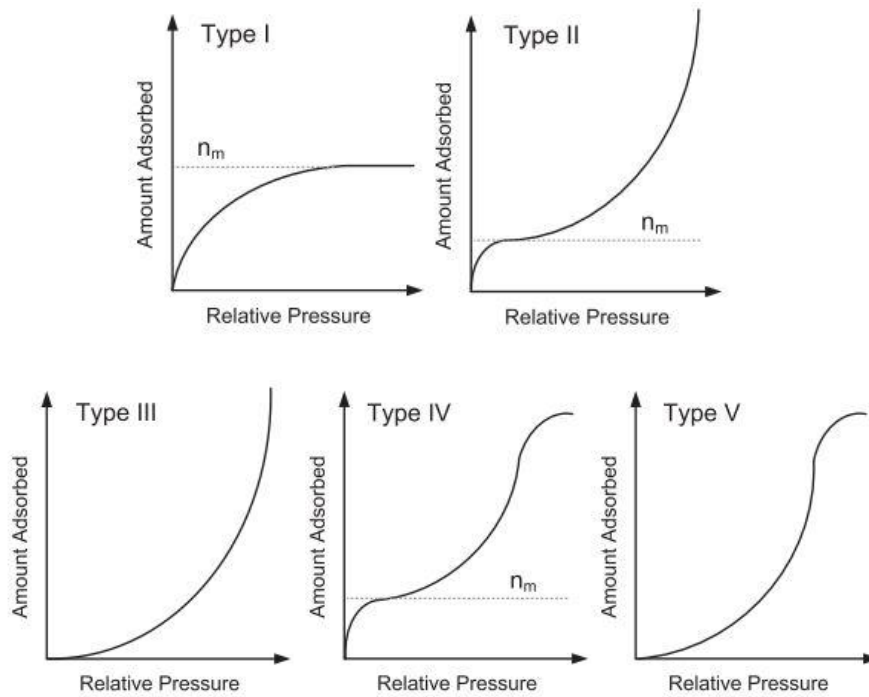


Figure 10: The five types of adsorption isotherms according to Brunauer-Emmett-Teller ³⁶.

The BET equation (12) can be used to determine the monolayer and specific surface area in various physicochemical areas in case of a type II or type IV isotherm ^{35,39}:

$$\frac{1}{V} \frac{x}{1-x} = \frac{c-1}{c V_m} x + \frac{1}{c V_m} \quad (12)$$

V	volume of adsorbed molecules (cm ³)
V _m	volume of the monolayer (cm ³)
c	constant
x	relative pressure (p/p ₀)

The BET constant c is related to the average heat of adsorption of the monolayer. The constant is related to the adsorbate–adsorbent interaction strength, and therefore to the heat of adsorption. With increasing c_{BET} value, also the interaction increases.

The plot of $x/V(1-x)$ versus x should result in a straight line over a certain x (p/p_0) range. With the slope and the intercept of the resulting linear plot, V_m , the amount of adsorbed gas of a monolayer, can be determined³⁶. This can be seen in the following equations 13 – 16.

$$Slope = \frac{c_{BET} - 1}{V_m * c_{BET}} \quad (13)$$

$$Intercept = \frac{1}{V_m * c_{BET}} \quad (14)$$

$$Vm = \frac{1}{Slope + Intercept} \quad (15)$$

$$SSA = \frac{V_m * N_A * a_m}{v_m * m_s} \quad (16)$$

N_A	Avogadro's number ($6.022 * 10^{23} \text{ mol}^{-1}$)
a_m	effective cross section area of one adsorbed molecule ($\text{m}^2 \text{ molecule}^{-1}$)
v_m	molar volume of one adsorbed molecule ($\text{cm}^3 \text{ g}^{-1} \text{ mol}^{-1}$)
m_s	mass of substrate (g)
SSA	specific surface area ($\text{m}^2 \text{ g}^{-1}$)

2.2.5 Barrett-Joyner-Halenda analysis (BJH)

The Barrett-Joyner-Halenda analysis is a widely used method for the determination of the particle size distribution of the type IV adsorption isotherm of mesopores (Ø 2-50 nm) and micropores (Ø <2nm)⁴⁰. The BJH equation, which is based on the Kelvin equation, can be seen in equation (17).

$$V_{pn} = R_n \Delta V_n - R_n \Delta t_n \sum_{j=1}^{n-1} c_j A_{pj} \quad (17)$$

V_{pn}	pore volume
R_n	$= r_p^2 / (r_k + \Delta t)^2$
r_p	radius of the mesopore
r_k	radius of the meniscus
V_n	volume of the desorbed gas
t_n	thickness of the adsorbed layer
c_j	ratio of $(r_p - t) / r_p$
A_{pj}	area of each pore

In case of the type IV adsorption isotherm, hysteresis occurs in adsorption and desorption. This hysteresis depends on the shape of the mesopore and the particle size distribution can be acquired. During the adsorption and desorption process, the formation of the monolayer and also capillary condensation of N_2 gas happens in the mesopores. Due to this, a difference in the meniscus between adsorption and desorption process occurs (Figure 11).

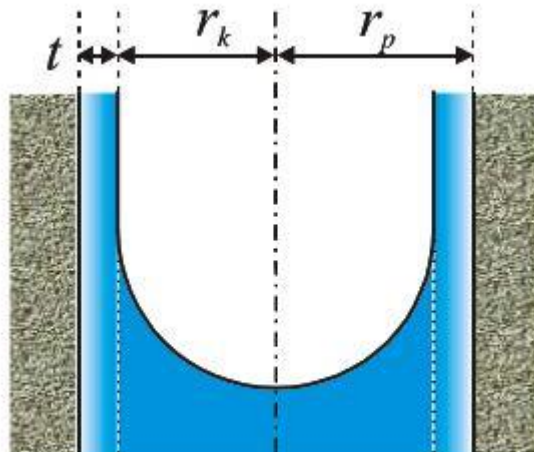


Figure 11: Illustration of the meniscus which appears during the capillary condensation⁴¹.

The Kelvin equation represents the relationship between mesopore size and critical condensation pressure and can be used to calculate the pore size distribution (equation 18) but only for particles bigger than 1 nm^{35, 40, 41, 42, 43}.

$$r_k = \frac{2 \gamma V_L}{RT \ln(p/p_0)} \quad (18)$$

r_k	radius of the meniscus
V_L	molar volume of liquid adsorbate
γ	surface tension
R	gas constant
T	absolute temperature
p/p_0	relative pressure

In the following equation (19), it can be seen that the radius r_p of the mesopore is the sum of the adsorbed layer thickness t , which can be obtained from the adsorption isotherm, and the radius of the meniscus r_k .

$$r_p = t + r_k \quad (19)$$

The determination of r_k can be derived from the Kelvin equation, using γ and V_L values of nitrogen at liquid nitrogen temperature (77 K) and the assumption that the mesopore has a cylindrical shape (equation (20)).

$$r_k = \frac{0.953}{\ln p/p_0} \quad (20)$$

The pore size distribution can now be obtained by plotting $\Delta V/\Delta r$ against the pore radius. The pore volume is obtained with the BJH equation and the radius with equation 19. Figure 12 shows a typical illustration of a pore size distribution^{39, 41}.

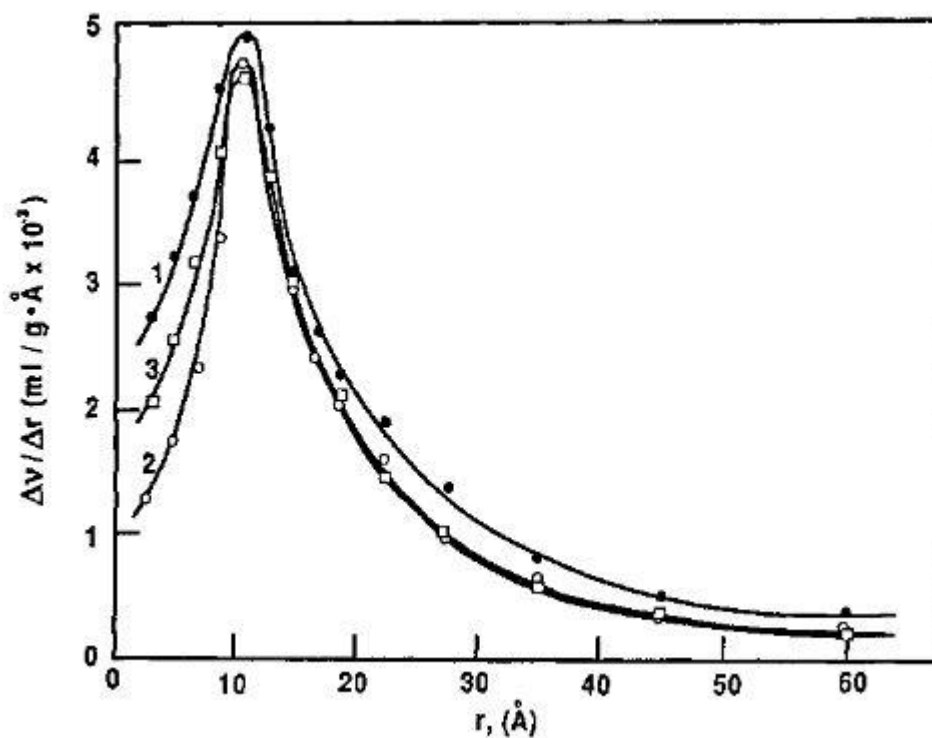


Figure 12: A typical pore size distribution graph from samples with different pore sizes.³⁹

2.3 Electrochemical Measurements

2.3.1 Potential Sweep Voltammetry

In potential sweep voltammetry experiments, as cyclic voltammetry and linear sweep voltammetry, the electrode potential is changed linearly with time and the current is recorded. Cyclic voltammetry is used for acquiring information about reduction and oxidation processes of molecular species, as well as for studying electron transfer-initiated electrochemical reactions. While cyclic voltammetry experiments can be conducted in most cases where linear sweep voltammetry is also used, there are circumstances in which linear sweep voltammetry is more useful, as for instance for irreversible reactions.^{44, 45, 46}

2.3.1.1 Linear Sweep Voltammetry (LSV)

The most common form of voltammetry is linear sweep voltammetry (LSV). In this method, the electrode potential is swept from an initial value (E_1) to a final value (E_2) at a constant scan rate, as well as at a constant rotation rate in the case of a rotating disc electrode (RDE)⁴⁷(Figure 13). The starting potential E_1 , is usually one where no electrochemical activity occurs and at the stopping potential E_2 the reaction is mass transport controlled⁴⁴. The potential of the working electrode is plotted against the resulting current and the theoretical voltammetry response is a peak-shaped wave⁴⁶(Figure 13, right).

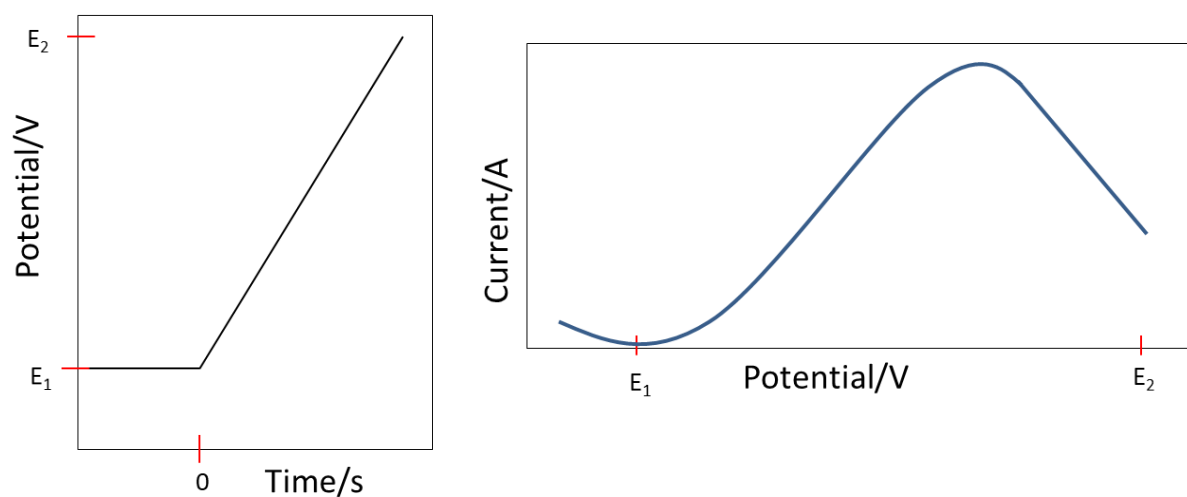


Figure 13: Potential-time curve of the linear sweep voltammetry (left) and a linear sweep voltammogram of a reversible reaction ($O + ne^- \leftrightarrow R$) (right).⁴⁸

2.3.1.2 Cyclic Voltammetry (CV)

In cyclic voltammetry experiments, the potential of a stationary working electrode (in an unstirred solution) is scanned linearly from E_{initial} to E_{final} as in LSV, but after reaching a maximum the potential is reversed which results in a triangular potential waveform (Figure 14, left) ⁴⁶.

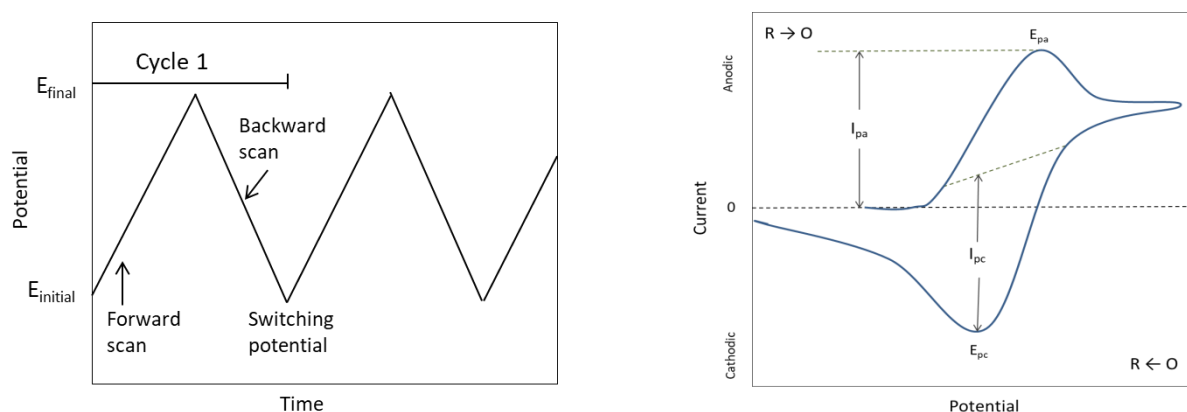


Figure 14: Potential-time signals during a cyclic voltammetry experiment (left) ⁴⁶ and an illustration of a cyclic voltammogram of a reversible reaction (right) ^{44, 49}.

At the beginning of the experiment, it is assumed that only the reduced form R is present. Thus, a positive going potential scan is chosen for the first half cycle starting from a value where no oxidation occurs. When the applied potential reaches the characteristic E° for the redox process, the anodic (oxidation) current begins to increase until a peak is reached. After the oxidation process, the direction of the potential sweep is reversed and during the reverse reaction the oxidized species O is reduced to R and a cathodic (reduction) peak occurs ⁴⁶. The characteristics of a cyclic voltammogram, which includes the anodic peak current (I_{pa}), the cathodic peak current (I_{pc}) as well as the anodic (E_{pa}) and cathodic peak potentials (E_{ca}), can be seen in Figure 14 (right). A further impact on the shape of the CV has the scan rate, since it controls how fast the applied potential is scanned. A high scan rate leads to a decrease of the diffusion layer and thus, higher currents are observed ⁴⁵.

For a reversible electron transfer reaction, the peak currents can be determined with the Randles-Sevcik equation ⁴⁶. The equation 21 shows the linear increase of the peak current I_p with the square root of the scan rate ν at 25°C. The relation of the peak current to the concentration of the electroactive species as well as to the square root of the diffusion coefficient is described ⁴⁹.

$$I_p = (2.69 * 10^5) n^{3/2} A C D^{1/2} \nu^{1/2} \quad (21)$$

I_p	Peak current (A)
ν	scan rate ($V s^{-1}$)
n	number of electrons
A	electrode surface area (cm^2)
D	Diffusion coefficient of analyte ($cm^2 s^{-1}$)
C	bulk concentration of analyte ($mol cm^{-3}$)

For the determination of a reversible system, the following characteristics can be obtained: the cathodic and anodic peak potentials are independent of the scan rate and the ratio of I_{pa} to I_{pc} is always one. In equation 22, the separation between the peak potentials is given ⁴⁶:

$$\Delta E_p = E_{p,a} - E_{p,c} = \frac{0.059}{n} \quad (22)$$

For a simple, reversible one electron process, the peak separation is 59 mV. If those requirements are not fulfilled, an irreversible system is present, indicated by the shape change of the cyclic voltammogram. ⁴⁹

2.3.2 Rotating disc electrode (RDE)

For the determination of kinetic data ⁴⁹ during the electrochemical measurements, a rotating disc electrode (RDE) is used as working electrode. The rotating disc electrode consists of a disc made of Pt, Ni, Cu, Au, Fe, Si, CdS, GaAs, glassy carbon or graphite ⁴⁴. The disc is imbedded in a rod of insulating material (PTFE, epoxy resin) and attached to a motor which rotates the RDE at desired frequencies. The electrical connection to the electrode is made through a brush contact. A schematic illustration of the RDE and its flow pattern caused due to convection, can be seen in Figure 15.

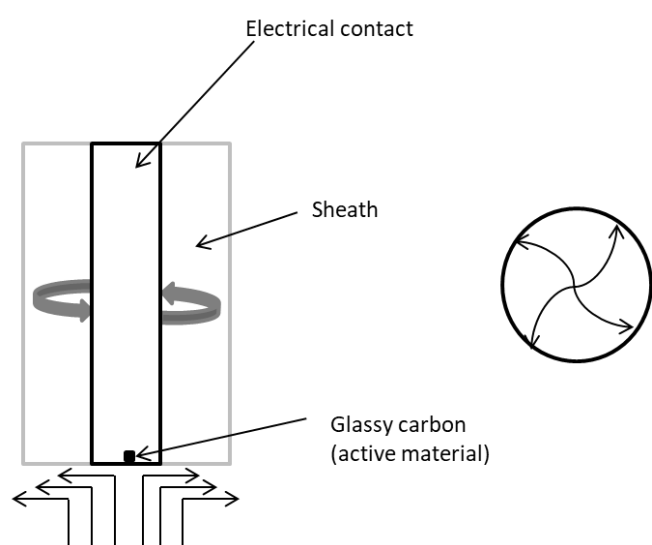


Figure 15: Illustration of the RDE and the resulting convective stream lines, side view (left) and from below the disc (right) ⁴⁹

In experiments with a rotating disc electrode, the RDE acts as a pump pulling solution up to the disc and slinging it away across the teflon cover of the glassy carbon disc, which results in a concentration gradient due to diffusion and convection. During the RDE measurements, the electrolyte can be divided into two zones according to the Nernst diffusion layer model. The region close to the surface of the electrode is assumed to be a totally stagnant layer, with a thickness δ_H , and diffusion is the only type of transport.

In the second zone, adjacent to the first one, a strong convection occurs and all species concentrations are constant⁵⁰. The thickness δ_H of the first zone, which is known as hydrodynamic boundary layer, can be determined with the following equation (23).^{44, 47}.

$$\delta_H = 3.6 (\nu/\omega)^{1/2} \quad (23)$$

- ν kinematic viscosity ($\text{cm}^2 \text{s}^{-1}$)
- ω angular rotation rate ($\omega = 2 \pi f/60$) (s^{-1})
- f rotation rate (revolutions min^{-1})

In an aqueous solution at a moderate rotation rate (~ 1000 rpm) δ_H is about 300-400 μm thick^{44,47}. The thickness of the diffusion layer δ_F , immediately adjacent to the electrode, can be described with equation (24), where D_F is the diffusion coefficient of a molecule or ion. The diffusion layer is much thinner than the hydrodynamic boundary layer. With a diffusion coefficient of $10^{-5} \text{cm}^2 \text{s}^{-1}$, δ_F is approximately 0.05 δ_H .

$$\delta_F = 1.61 D_F^{1/3} \nu^{1/6} \omega^{-1/2} \quad (24)$$

2.3.3 Koutecky-Levich Analysis

The Koutecky-Levich analysis is a study to investigate kinetic processes. In this study, a series of voltammograms at different rotation rates (100, 400, 900, 1600, 2500 rpm) are conducted with a rotating disc electrode, as it can be seen in Figure 16. In the potential range of 0.85 – 0.93 V vs. RHE, the current density is not dependent on the electrode rotation rate, which means that the current density is only controlled by the electron transfer kinetics. At the plateau, in the voltage range between ~0.63 V - 0.30 V vs. RHE, the reaction is controlled by diffusion-convection processes and the current density is increasing with increasing rotation rates^{47,51}.

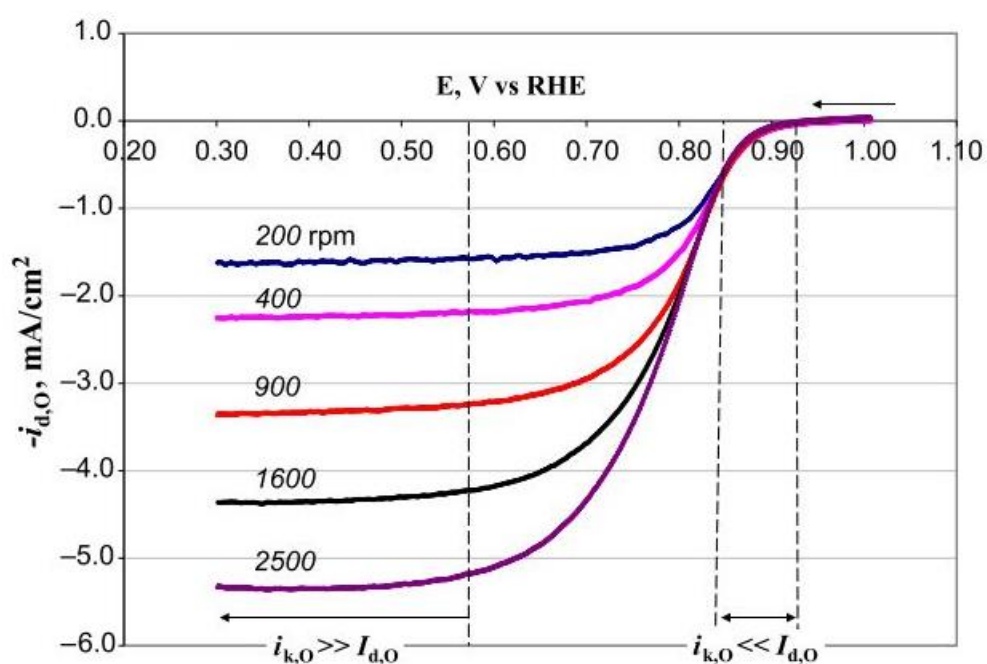


Figure 16: Voltammograms at different rotation rates acquired with a Pt disk electrode, in O_2 saturated 0.5 M H_2SO_4 solution, $v = 5 \text{ mV/s}$ ⁵¹.

Figure 17 (left) shows an ORR voltammogram at different rotation rates, whose data is used to create the Koutecky-Levich plot on the right. The reciprocal limiting current (obtained in Figure 17, right) is plotted against the reciprocal angular rotation rate (rad/s). If the extrapolation back to the vertical axis (to infinite rotational rate) intersects the x-axis at zero, the currents of the half-cell reactions are only limited by mass transport (red line in Figure 17). But if the extrapolation do not intersect the x-axis at zero, the currents are limited by kinetics, which means that the rate of the half-cell reactions is limited by slow kinetics at the electrode surface (violet and blue lines in Figure 17) ⁴⁷.

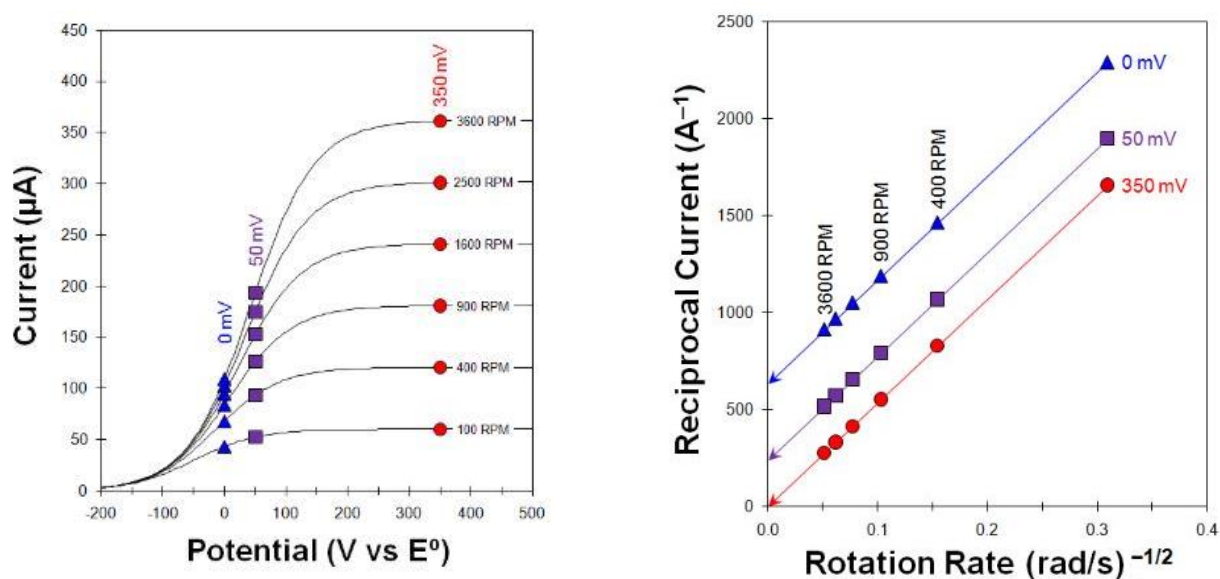


Figure 17: ORR Voltammograms at different rotation rates (left) and the Koutecky-Levich plot determined at different potentials (right).

The linear portion of the data of a Koutecky-Levich plot can be described with the following equation (25). The number of transferred electrons (n) can be acquired from the slope (equation (26)) of the linear portion and calculated with equation 27.

$$\frac{1}{i} = \frac{1}{i_K} + \left(\frac{1}{0.62 n F A D^{\frac{2}{3}} \nu^{-\frac{1}{6}} C} \right) \omega^{-\frac{1}{2}} \quad (25)$$

$$\text{Slope} = \frac{1}{0.62 n F A D^{\frac{2}{3}} \nu^{-\frac{1}{6}} C} \quad (26)$$

$$n = \frac{1}{\text{Slope} \cdot 0.62 F A D^{\frac{2}{3}} \nu^{-\frac{1}{6}} C} \quad (27)$$

i	Current (A)
i_K	Kinetic current (A)
n	number of electrons
F	Faraday constant (96485 C mol ⁻¹)
A	active area of the electrode
D	Diffusion coefficient (cm ² s ⁻¹)
ν	kinematic viscosity (cm ² s ⁻¹)
ω	rotation rate of the electrode (rad s ⁻¹)
C	Bulk concentration (mol cm ⁻³)

3 Experimental Procedure

Three different spinel catalysts (CoMn_2O_4 (M1/M2) and MnCo_2O_4 (M2)) are prepared in this work, according to two different synthesis methods found in the literature^{11, 12}. The CoMn_2O_4 catalyst can be synthesized with method one and two, and with the second method the MnCo_2O_4 catalyst can be obtained. Afterwards, different physicochemical characterisations (SEM/EDX, XRD, BET/BJH) are conducted to analyse the surface morphology, to obtain the crystal structure and the specific surface area. The electrochemical activity is investigated with cyclic voltammetry and linear sweep voltammetry experiments.

3.1 Catalyst Preparation

3.1.1 Method 1

3.1.1.1 Synthesis of amorphous MnO_2

The first step of the preparation of CoMn_2O_4 catalyst is the synthesis of the amorphous MnO_2 precursor. For this, a 0.03 M $\text{Mn}(\text{CH}_3\text{COO})_2$ solution (100 mL) is mixed slowly with a 0.04 M KMnO_4 solution (50 mL) on a magnetic stirrer for several minutes at room temperature. Before the mixing, the KMnO_4 solution is adjusted with a 25% ammonia solution to pH 12. The resulting brown deposit is collected via centrifugation (Hermle, Z 323 K) and washed several times with distilled water. Afterwards, the deposit is dried in the drying cabinet (Heraeus, T 5042) at 60°C overnight. The result is a fine-grained, dark brown, shiny powder that can be seen in Figure 18.



Figure 18: The dried amorphous MnO_2 precursor.

3.1.1.2 Synthesis of the nanocrystalline CoMn_2O_4 catalyst

For the synthesis of the nanocrystalline CoMn_2O_4 spinel catalyst, 0.348 g (0.004 mol) of amorphous MnO_2 and 0.714 g (0.002 mol) $\text{CoCl}_2 \cdot 6 \text{H}_2\text{O}$ are mixed in 20 mL of distilled water on a magnetic stirrer for several minutes at room temperature. A violet/dark brown suspension is formed immediately. With a 1 M NaBH_4 solution (0.227 g diluted in 6 mL 0.01 M NaOH (pH=11.55)), the educts are reduced to CoMn_2O_4 and the suspension turned immediately colourless (Figure 19). The resulting precipitate is then collected via centrifugation, washed several times with distilled water to remove residual ions and then dried at 80°C for 12 hours in the drying cabinet ¹¹.



Figure 19: MnO_2 precursor mixed with $\text{CoCl}_2 \cdot 6 \text{H}_2\text{O}$ (left), the resulting product after the reduction with NaBH_4 (right).

3.1.2 Method 2

With method two, it is possible to synthesize both catalysts (CoMn_2O_4 and MnCo_2O_4). This method also starts with the synthesis of a precursor, $\text{Co}_{0.33}\text{Mn}_{0.67}\text{CO}_3$ and $\text{Mn}_{0.33}\text{Co}_{0.67}\text{CO}_3$, respectively. Afterwards, these precursors are annealed at 400°C in a high temperature furnace from Schröder (S13).

3.1.2.1 Synthesis of $\text{Co}_{0.33}\text{Mn}_{0.67}\text{CO}_3$ and $\text{Mn}_{0.33}\text{Co}_{0.67}\text{CO}_3$

In case of the synthesis of CoMn_2O_4 , 2.24 g (0.013 mol) cobalt acetate tetrahydrate ($\text{Co}(\text{CH}_3\text{COO})_2 \cdot 4\text{H}_2\text{O}$) and 4.41 g (0.018 mol) manganese acetate tetrahydrate ($\text{Mn}(\text{CH}_3\text{COO})_2 \cdot 4\text{H}_2\text{O}$) are mixed together in 200 mL distilled water. Afterwards, a 0.49 M ammonium sulfate solution (13.2 g $(\text{NH}_4)_2\text{SO}_4$ in 200 mL) is added slowly and stirred for two hours. Then, 0.49 M ammonium bicarbonate (7.9 g $(\text{NH}_4)\text{HCO}_3$ in 200 mL), is added slowly to the mixture and stirred for four hours. At first, when the solution only contains cobalt and manganese acetate, it is light pink and clear but when the other two solutions are added it gets more and more cloudy (Figure 20).

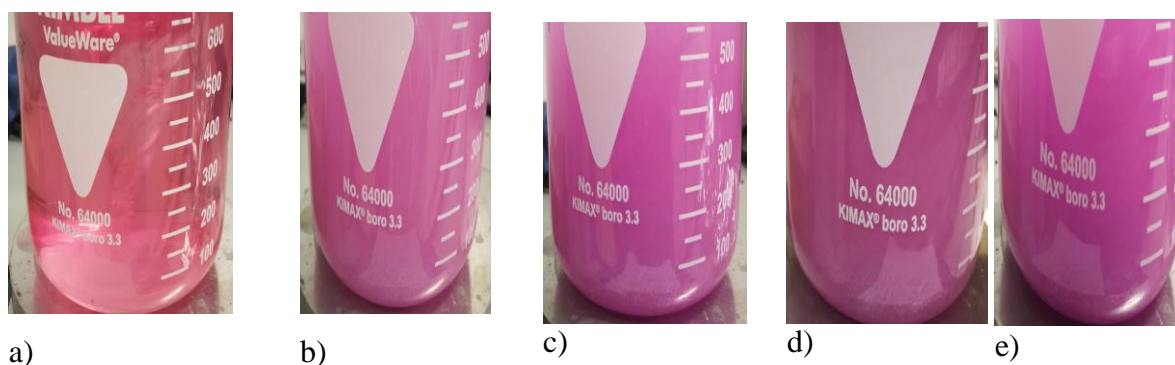


Figure 20. The synthesis of $\text{Co}_{0.33}\text{Mn}_{0.67}\text{CO}_3$ at different stages: a) the mixture at the beginning, containing only $\text{Co}(\text{CH}_3\text{COO})_2 \cdot 4\text{H}_2\text{O}$ and $\text{Mn}(\text{CH}_3\text{COO})_2 \cdot 4\text{H}_2\text{O}$, b) after the addition of $(\text{NH}_4)_2\text{SO}_4$, c) after 2 h of stirring, d) after the addition of $(\text{NH}_4)\text{HCO}_3$, e) after 4h of stirring.

After four hours of stirring, a pink precipitate is obtained and separated via centrifugation. The precipitate was washed with distilled water and ethanol and dried at 60°C for 12 hours in the oven (Figure 21 a) and b)). For the synthesis of $\text{Mn}_{0.33}\text{Co}_{0.67}\text{CO}_3$, the same procedure is conducted but the molar ratios of $\text{Co}(\text{CH}_3\text{COO})_2 \cdot 4\text{H}_2\text{O}$ and $\text{Mn}(\text{CH}_3\text{COO})_2 \cdot 4\text{H}_2\text{O}$ are reversed (4.48 g (0.018 mol) and 3.18 g (0.013 mol), respectively).



Figure 21: The $Co_{0.33}Mn_{0.67}CO_3$ precipitate before (a) and (b) after drying at $60^\circ C$ and (c) after annealing at $400^\circ C$ to obtain $CoMn_2O_4$.

3.1.2.2 Synthesis of spherical $CoMn_2O_4$ and $MnCo_2O_4$

The carbonate intermediates are annealed in a high temperature oven from Schröder (S13) at $400^\circ C$ with a heating rate of $2^\circ C\ min^{-1}$ for 8 hours and are kept there for additional 8 hours, followed by cooling down to RT with the same rate (Figure 21 c))¹².

3.2 Physicochemical Characterisation

Different physicochemical characterisations of the three catalysts $CoMn_2O_4$ (M1/M2) and $MnCo_2O_4$ (M2) are conducted. For the structural analysis, X-ray powder diffraction is used. Moreover, the surface morphology and their homogeneity as well as the elemental composition is examined by scanning electron microscopy (SEM) and energy dispersive x-ray analysis (EDX). Furthermore, the specific surface area (SSA) is determined with the Brunauer-Emmett-Teller analysis, since it has an impact on the catalytic activity of the catalyst samples.

3.2.1 X-Ray Diffraction (XRD)

The characterisation of the structure is done with a X-ray powder diffractometer Bruker D8 Advance, with a $Cu-K\alpha$ X-ray source in the range of 20° to $100^\circ\ 2\theta$. For data analysis, the software program X'Pert HighScore plus (PANanalytical) is used and the evaluation of the diffractograms is done by Rietveld refinement.

3.2.2 Scanning electron microscopy (SEM)

For the investigation of the surface morphology and the particle size of the catalysts, the Secondary Electron Microscope ESEM Tescan 500 PA is used. The catalyst powder is fixed on the sample holder via a double-sided adhesive carbon tape. The SEM pictures are taken at different magnifications.

3.2.3 Energy dispersive X-ray analysis (EDX)

In addition to the SEM images, the elemental composition is determined with the Energy Dispersive X-Ray Spectroscopy (EDX) using an analyser from Oxford Instruments. The EDX spectra are recorded at different areas to obtain the average atomic and weight percentages of elements present on the surface area of the catalyst powders.

3.2.4 Brunauer-Emmett-Teller and Barrett-Joyner-Halenda analysis (BET/BJH)

The specific surface area (SSA) is determined with the Brunauer-Emmett-Teller (BET) analysis. Since the catalytic activity is related to the specific surface area, it can be stated that the higher the SSA the better the catalytic activity. The measurements are conducted with a TriStar II 3020 (V1.03) at the Research Centre for Pharmaceutical Engineering (RCPE) at Graz University of Technology. The samples are outgassed for 24h and the measurement is started at 77 K. The amount of N₂ adsorbed is recorded in a relative pressure range of 0.009 to 0.99. In addition, the pore volume is determined between 1.7 nm and 250 nm diameter as well as the pore size with the Barrett-Joyner-Halenda (BJH) method.

3.3 Electrochemical Characterisation

For the investigation of the electrochemical activity of the catalysts CoMn_2O_4 (M1/M2) and MnCo_2O_4 (M2), half-cell experiments including cyclic voltammetry (CV) and linear sweep voltammetry (LSV) are conducted. The measurements are performed with a glassy carbon rotating disc electrode (RDE) from Pine Instruments Co. (AFMSRCE) in a typical three-electrode setup. The Autolab Potentiostat PGSTAT128N/100/300 (AUT83568, AUT72179, AUT86739) with the software NOVA 1.11 is used for data analysis. The cyclic voltammetry experiments (CV) are conducted for the investigation of reduction and oxidation processes of the catalysts. The bifunctional activity is examined with linear sweep voltammetry (LSV) experiments to study the oxygen evolution- (OER) and oxygen reduction reactions (ORR).

3.3.1 Working electrode preparation

The transfer of the catalyst onto the RDE ($\text{Ø}=5$ mm, $A=0.196$ cm²) is implemented with a suspension containing the catalyst and Vulcan XC72, which is added to enhance the electronic conductivity. The suspension is prepared according to the work of Cheng et. al.¹¹ but with a small modification. Instead of isopropanol (1 mL), a mixture of isopropanol and distilled water (7:3, v:v, 1 mL) is used in this work. Due to the higher surface tension of water, a precise application of the slurry onto the RDE is possible. In Table 1, the composition of the catalyst suspension, which consists of 70% Vulcan XC72 and 30% catalyst, is listed.

Table 1: The composition of the catalyst suspensions.

Slurry	CoMn ₂ O ₄ (mg)	MnCo ₂ O ₄ (mg)	Vulcan XC72 (mg)	catalyst loading (mg)	
1 CoMn ₂ O ₄ (M1)	1.5	-	3.5	0.015	0.0196
2 CoMn ₂ O ₄ (M2)	1.5	-	3.5	0.015	0.0196
3 MnCo ₂ O ₄ (M2)	-	1.5	3.5	0.015	0.0196
4 Vulcan XC72	-	-	3.5	0.035	0.045

All suspensions are ultrasonically blended for 30 minutes. Ahead of each measurement, the RDE is polished with corundum powder (Al₂O₃, particle size 0.3 μm), moisturized with distilled water, cleaned in the ultrasonic bath for ~30 seconds and dried under the infrared (IR) lamp. Subsequently, two times 5 μL (catalyst loading = 0.015 mg, Vulcan XC72 = 0.035 mg) or two times 6.54 μL (catalyst loading = 0.0196 mg, Vulcan XC72 = 0.045 mg) of the suspension are transferred onto the glassy carbon disc of the RDE. After each application, the RDE is dried under the IR lamp. The final step is the application of a Nafion layer (15 μL, 1 wt% Nafion in distilled water) to prevent the destruction of the catalyst layer. The catalyst suspension (left) and the drying step (right) can be seen in Figure 22.

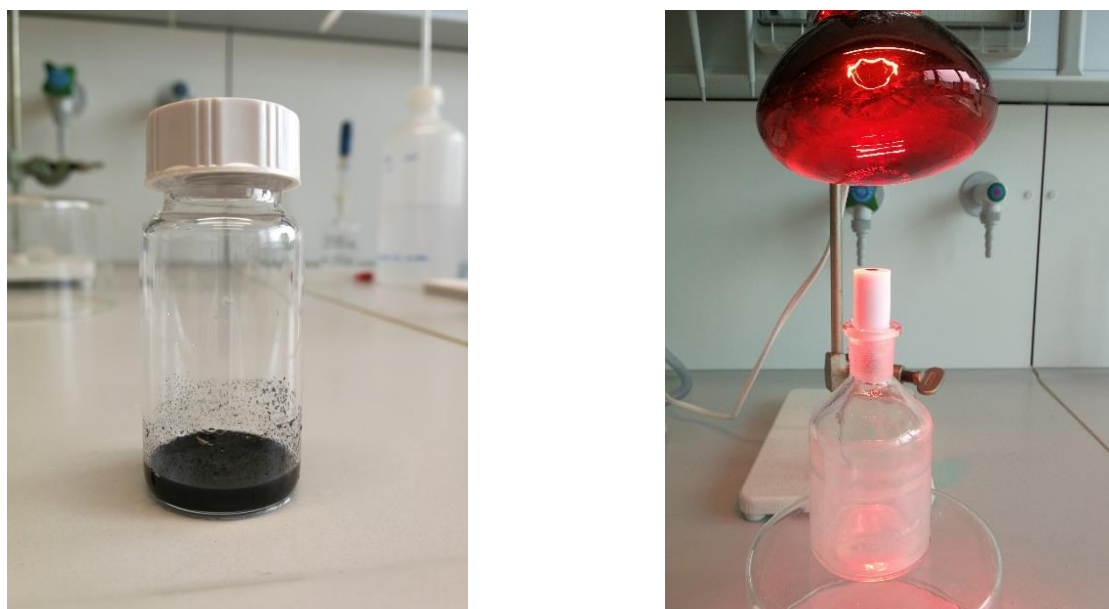


Figure 22: The catalyst suspension after 30 min of ultrasonically mixing (left) and the drying step of the applied catalyst (right).

3.3.2 Electrochemical Measurements (CV, LSV)

All electrochemical measurements in this work are carried out in a typical three-electrode setup, which consists of working electrode (WE), counter electrode (CE) and reference electrode (RE), as it can be seen in Figure 23. The working electrode (WE), that is a coated RDE, is in the middle of the electrochemical glass cell. On the left and on the right hand side are the RE, a Hg/HgO reference electrode filled with 1 M or 8 M KOH in a Haber-Luggin capillary and the CE, a platinum net. Potassium hydroxide solution (0.1 M or 8 M) is used as alkaline electrolyte. Prior to each CV or OER measurement, the electrolyte is deaerated with nitrogen gas for 30 minutes to remove the oxygen from the solution. For investigations of the ORR, the electrolyte is saturated with oxygen for 30 minutes. During the measurements, the respective gas is blown over the electrolyte. All measurements are conducted at room temperature.

The cyclic voltammetry measurements are performed at a scan rate of 10 mV/s and 10 cycles are conducted. The second cycle is taken for data analysis. The voltammograms of OER and ORR measurements are conducted at a scan rate of 5 mV/s and a rotation rate of 1600 rpm. For data analysis, the fifth sweep of OER and ORR is taken. Additionally, a sixth sweep at 400 rpm is sometimes recorded in case of the OER. The rotation rates are also varied from 100 to 2500 rpm to see the impact of the rotation rate on the catalytic activity.

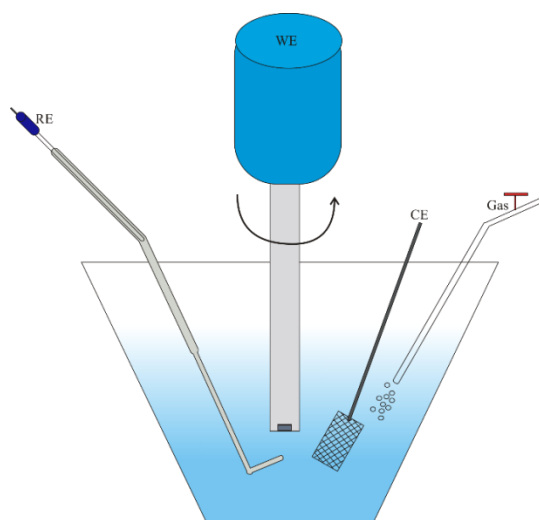


Figure 23: A schematic illustration of the three-electrode assembly.

3.3.3 Koutecky-Levich Analysis

The Koutecky-Levich analysis is used to determine the number of transferred electrons during the oxygen reduction reactions. The respective formula which is used for the calculation of the transferred electrons can be seen in 2.3.3. In the Koutecky-Levich plot, the reciprocal limiting currents are plotted against the reciprocal square root of the rotation rate and the number of electrons can be obtained from the slope. For the Koutecky-Levich study, a set of rotation rates are chosen, which are a multiple of perfect squares (such as 100, 400, 900, 1600 and 2500 rpm) to facilitate the construction of the plot. The values of the diffusion coefficient, the bulk concentration and the kinematic viscosity, which are used for the calculation of the transferred electrons during the ORR, can be seen in Table 2 and are taken from the literature ^{52, 53, 54}.

Table 2: The used values for the calculation of the transferred electrons.

KOH	0.1 M ⁵²	8 M ^{53, 54}
Diffusion coefficient D_{O_2} ($\text{cm}^2 \text{s}^{-1}$)	$1.73 \cdot 10^{-5}$	$1.4 \cdot 10^{-5}$
Bulk concentration C_{O_2} (mol cm^{-3})	$1.14 \cdot 10^{-6}$	$8.4 \cdot 10^{-7}$
Kinematic viscosity ($\text{cm}^2 \text{s}^{-1}$)	0.01	0.01705

4 Results and discussion

4.1 Physicochemical characterisation

4.1.1 X-Ray diffraction (XRD)

The XRD pattern of CoMn_2O_4 (M1 and M2) as well as MnCo_2O_4 (M2) are shown in Figure 24. Additional diffractograms of the Inorganic Crystal Structure Database (ICSD)⁵⁵ are added for comparison, in case of CoMn_2O_4 (M1) ICSD #39197 and #164367, #31854 for CoMn_2O_4 (M2) and for MnCo_2O_4 (M2) #36256. Rietveld refinement of CoMn_2O_4 (M1) shows tetragonal structure of the type CdMn_2O_4 .

The CoMn_2O_4 catalyst, synthesized according to the second method, shows a rhombohedral structure which is contrary to the result obtained in the literature. It should have a body-centred tetragonal structure. The MnCo_2O_4 shows 100% cubic structure as it is assumed in the literature¹². The comparison of the obtained pattern with the one of the database, shows that almost all characteristic peaks are obtained.

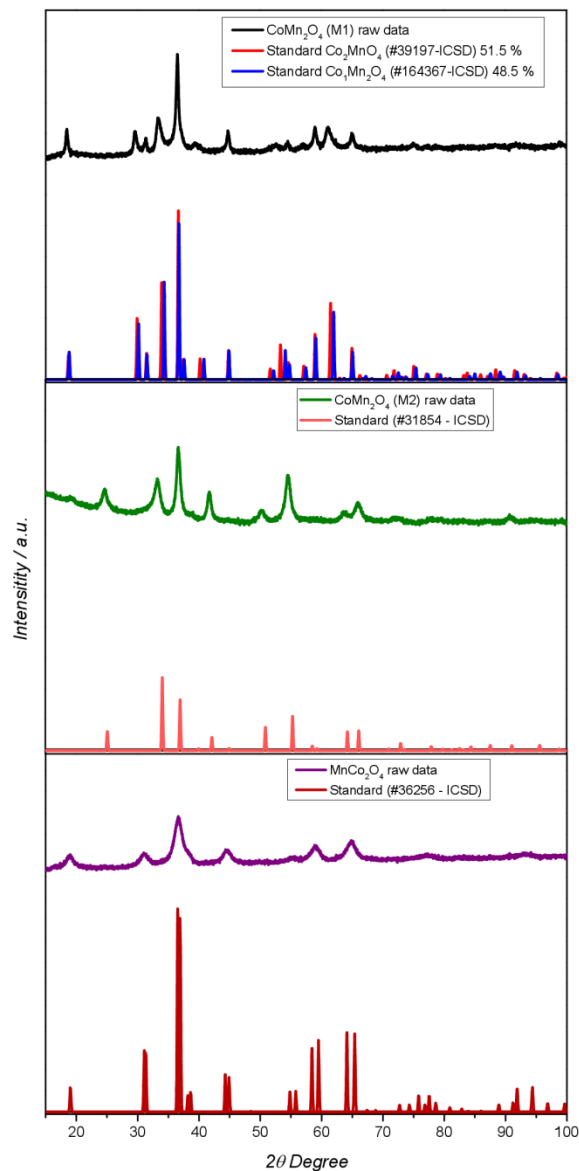


Figure 24: XRD diffractograms of the three catalysts, CoMn_2O_4 (M1/M2) and MnCo_2O_4 (M2) in comparison with literature data⁵².

Comparing the diffractograms with the literature ^{11,12}, almost every peak could be obtained. The catalysts prepared according to the second method, show rather broad peaks and a high background, which may indicate small crystallites and a high amount of amorphous parts. The space group of CoMn₂O₄ (M1) is I4₁/amd, for CoMn₂O₄ (M2) it is R-3 R (148) and for MnCo₂O₄ (M2) it is Fd-3mS (227) which is in accordance with the literature ^{11,12}.

With the Rietveld refinement, also the lattice constants of the catalysts are determined (Table 3). The obtained values of the lattice constants are in good agreement with the data from the ICSD and the literature values.

Table 3: Lattice constants of the catalysts CoMn₂O₄ (M1/M2) and MnCo₂O₄ (M2) compared to ICSD ⁵⁵ and literature ^{11,12}.

Sample	a = b [Å]	c [Å]
CoMn₂O₄ (M1)	5.75	9.22
CoMn₂O₄ (#39197, ICSD)	5.784	9.091
CoMn₂O₄ (#164367, ICSD)	5.775	8.958
literature value ¹¹	5.759	9.252
CoMn₂O₄ (M2)	4.8987	13.906
CoMn₂O₄ (#31854, ICSD)	4.933	13.7106
literature value ¹²	5.77	8.95
MnCo₂O₄ (M2)	8.13	8.13
MnCo₂O₄ (#36256, ICSD)	8.072	8.072
literature value ¹²	8.28	8.28

4.1.2 Scanning electron microscopy (SEM)

With scanning electron microscopy (SEM), information about the shape, morphology and particle size of the catalysts can be obtained. The following Figures 25 to 28 represent the SEM images of the amorphous MnO_2 precursor, the CoMn_2O_4 catalyst as well as the catalysts synthesized with the second method (CoMn_2O_4 and MnCo_2O_4). The first four pictures (Figure 25 and 26) show the amorphous MnO_2 and the CoMn_2O_4 (M1) catalyst at different magnifications. They both look like crushed stone plates, which have a size between $5\ \mu\text{m}$ and $50\ \mu\text{m}$. Figure 26 (right), shows some fine-grained powder on the crushed stone plates, which is due to the pestling in an agate mortar and the fine particles are in nm scale.

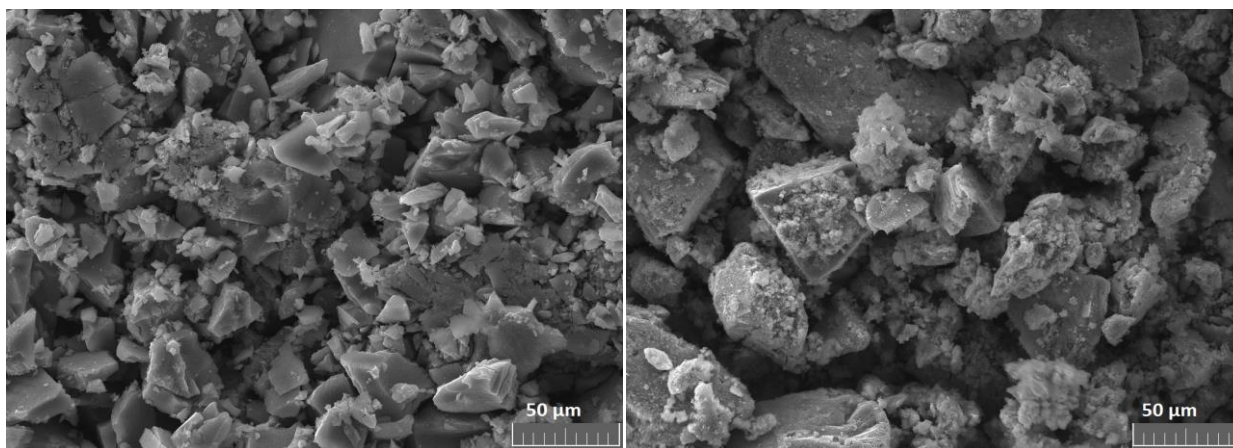


Figure 25: SEM images of amorphous MnO_2 (left) and CoMn_2O_4 (M1, right) at 1.000 fold magnification.

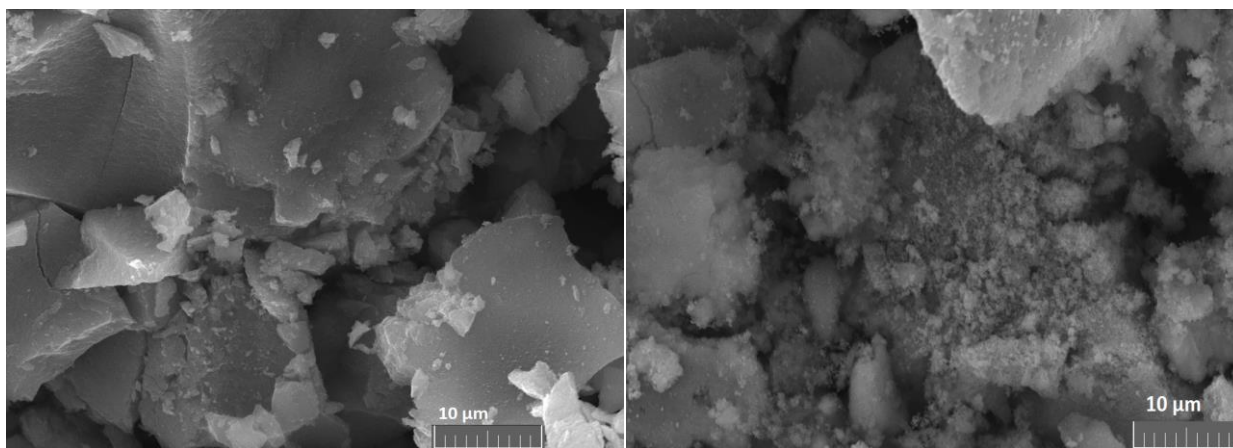


Figure 26: SEM images of amorphous MnO_2 (left) and CoMn_2O_4 (M1, right) at 5.000 fold magnification.

The Figures 27 and 28 represent the SEM images of the catalysts (CoMn_2O_4 and MnCo_2O_4) synthesized with the second method. The images show that both catalysts formed microspheres. In case of the CoMn_2O_4 , the microspheres are in the range of 5 μm and the MnCo_2O_4 has even smaller particles ($< 4 \mu\text{m}$). The CoMn_2O_4 catalyst tends to form numerous agglomerates, which can be seen in Figure 27 on the left, whereas the MnCo_2O_4 catalyst is only forming a few. In Figure 28 (left), the agglomerates of the CoMn_2O_4 catalyst are shown very well and the surface area of the particles looks “furry”. Figure 28 verifies the assumption that MnCo_2O_4 forms less agglomerates than CoMn_2O_4 .

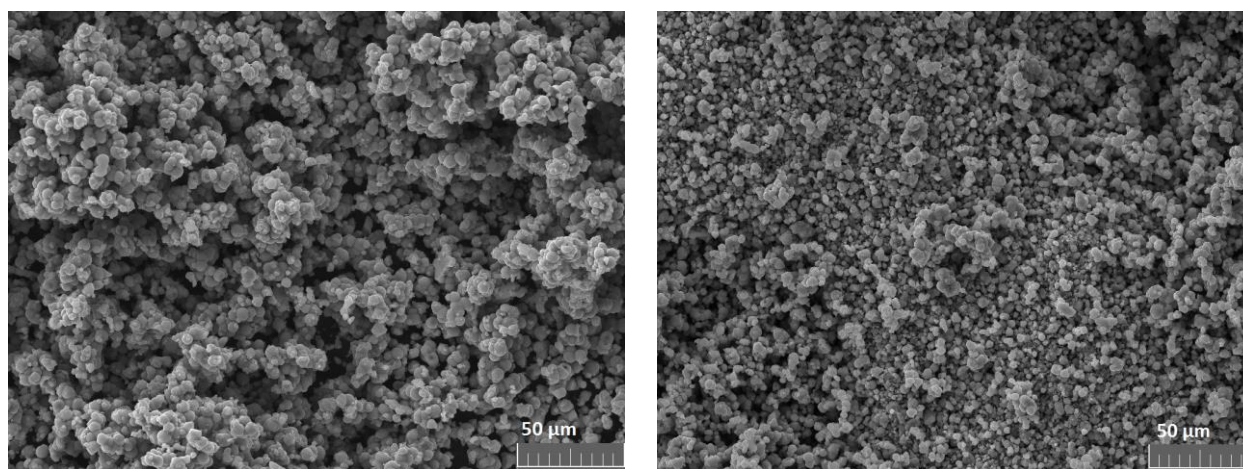


Figure 27: SEM images of CoMn_2O_4 (M2, left) and MnCo_2O_4 (M2, right) at 1.000 fold magnification.

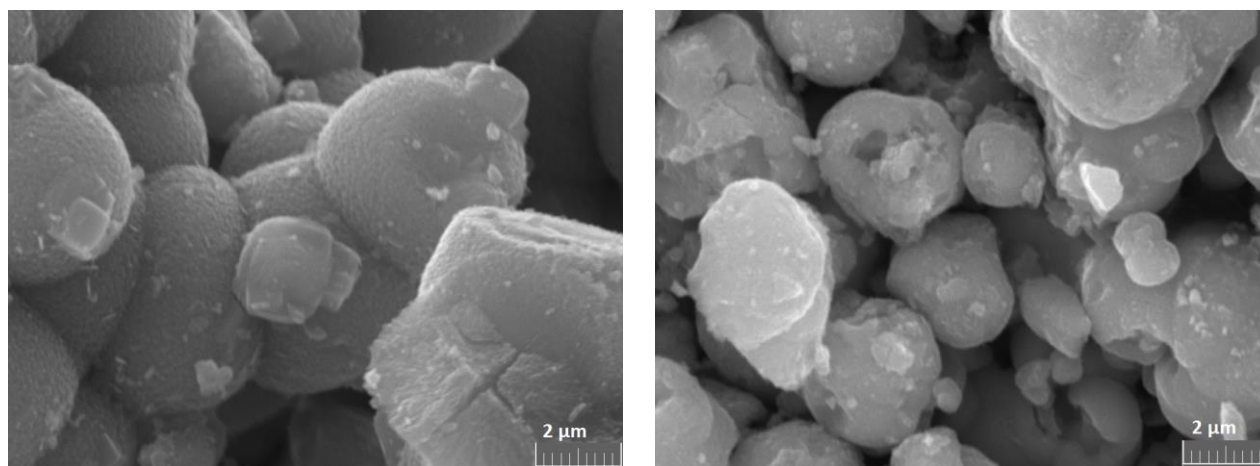


Figure 28: SEM images of CoMn_2O_4 (M2, left) and MnCo_2O_4 (M2, right) at 20.000 fold magnification.

4.1.3 Energy dispersive X-ray analysis (EDX)

The EDX spectra of the three catalysts (CoMn_2O_4 (M1/M2), MnCo_2O_4 (M2)) as well as of the amorphous MnO_2 precursor from the first catalyst are obtained at different areas (approximately 3-6) of the surface. The Figures 29 and 30 exemplify the area where the EDX spectra are obtained. The mean values of the chemical composition are presented in Table 4 and 5. The results show that all three catalysts only contain cobalt, manganese and oxygen at different ratios. The precursor contains only manganese and oxygen. Table 6 shows the Co:Mn ratios of the three catalysts and the Mn:O ratio of the amorphous MnO_2 precursor. According to the chemical composition, there should be a Co:Mn ratio of 1:2 in case of the CoMn_2O_4 , of 2:1 for MnCo_2O_4 and a Mn:O ratio of 1:2 for MnO_2 . The MnCo_2O_4 catalyst is in good agreement with the result of the literature (1.9:1¹²) but the CoMn_2O_4 catalyst synthesized with the second method, strongly deviates from the literature (1:2.04¹³). The CoMn_2O_4 catalyst, synthesized with the first method, also obtained a higher Co:Mn ratio of 1:2.5. The MnO_2 precursor yielded the expected Mn:O ratio.

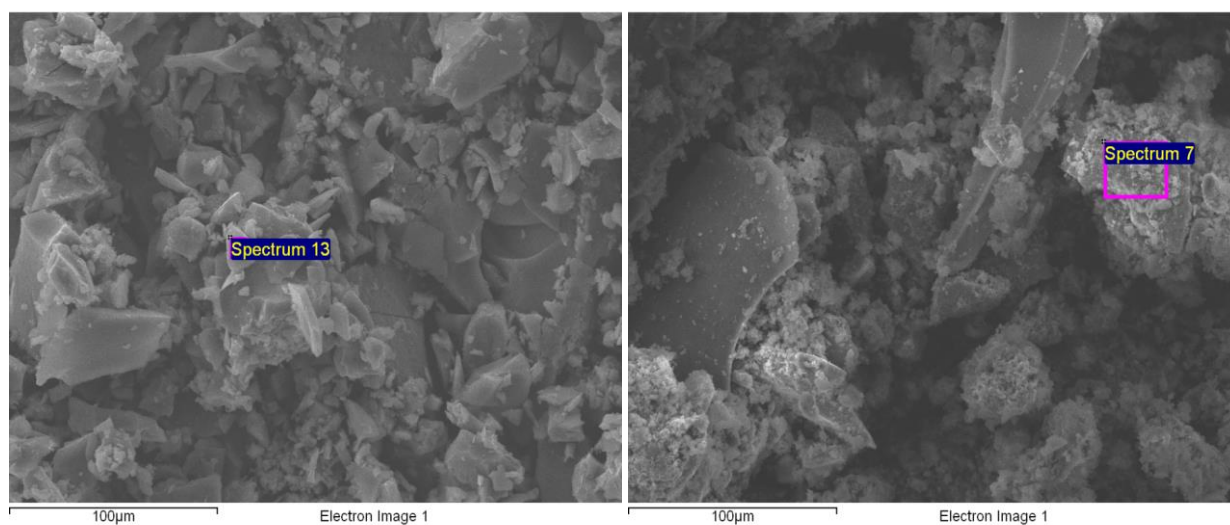


Figure 29: Area of the SEM picture, where the EDX spectrum of the amorphous MnO_2 (left) and CoMn_2O_4 (M1, right) is taken.

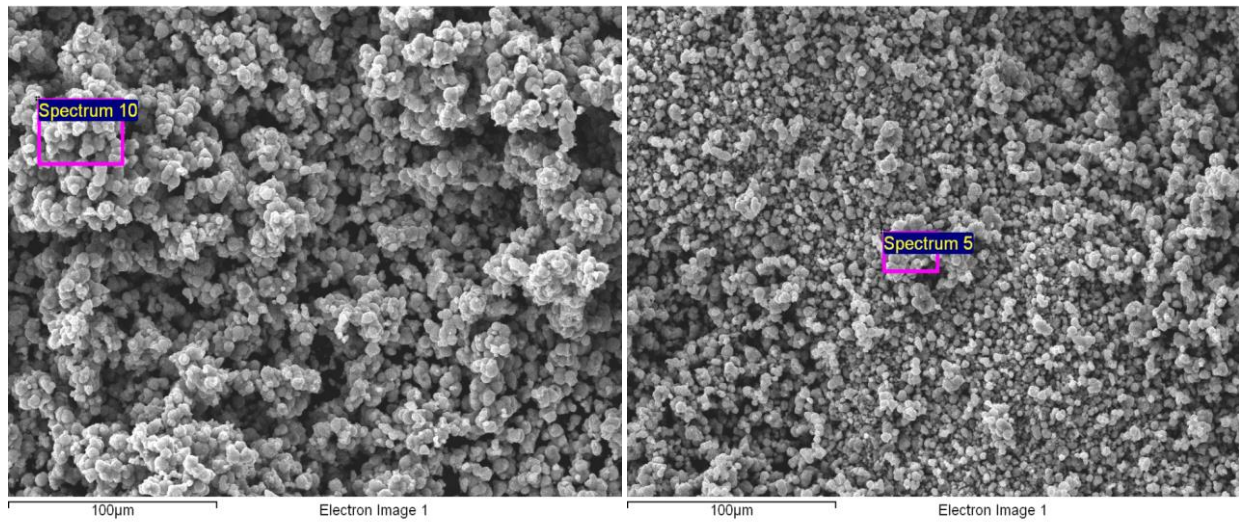


Figure 30: Area of the SEM picture, where the EDX spectrum of CoMn_2O_4 (M2, left) and MnCo_2O_4 (M2, right) is taken.

Table 4: The mean value of the chemical composition (at.%) of MnO_2 and the catalysts.

	amorphous MnO_2	CoMn_2O_4 (M1)	CoMn_2O_4 (M2)	MnCo_2O_4 (M2)
Co	-	12.16 ± 5.67	10.45 ± 0.80	28.29 ± 3.37
Mn	31.17 ± 13.48	31.70 ± 2.25	31.77 ± 3.43	15.11 ± 3.38
O	66.45 ± 13.73	44.91 ± 7.83	57.78 ± 3.82	52.85 ± 3.90

Table 5: The mean values of the chemical composition (wt.%) of MnO_2 and the catalysts.

	amorphous MnO_2	CoMn_2O_4 (M1)	CoMn_2O_4 (M2)	MnCo_2O_4 (M2)
Co	-	25.07 ± 6.16	18.75 ± 1.15	45.66 ± 1.59
Mn	57.81 ± 12.45	52.04 ± 1.71	52.97 ± 3.34	26.53 ± 2.85
O	38.92 ± 12.31	27.38 ± 6.33	28.28 ± 3.13	29.16 ± 0.75

Table 6: The chemical ratios of the three catalysts and of the amorphous MnO_2 precursor.

ratio	amorphous MnO_2	CoMn_2O_4 (M1)	CoMn_2O_4 (M2)	MnCo_2O_4 (M2)
Co:Mn	-	1:2.5	1:3.0	1.9:1
Mn:O	1:2.1	-	-	-

4.1.4 Brunauer-Emmett-Teller (BET) and Barrett-Joyner-Halenda analysis (BJH)

In the following Table 7, the results of the BET and BJH analysis are summarized. The N₂ adsorption of the three catalysts as well as of Vulcan XC72 as reference, are plotted in Figure 31. It is well known that a higher surface area indicates better electrochemical performance due to the fact that more active sites for oxygen adsorption are available. The specific surface area can be influenced by many factors, as for instance, particle size and particle shape. In Table 7, it can be seen that for the catalyst CoMn₂O₄ a much higher specific surface area (89.36 m²/g) can be obtained with the second synthesis method than with the first method (55.77 m²/g). In case of the first method, the obtained SSA is much smaller than the literature value. The measured SSA values for the second synthesis method are even much higher than in the literature ^{12,13}. This is in good agreement with the results from the electrochemical characterisation. The catalysts synthesized with the second method obtained much higher current density than the one synthesized with the first method (chapter 4.2). The Vulcan XC72, which is added to the catalyst slurry for enhancing the electronic conductivity, has the highest SSA (224.52 m²/g) of all measured samples and is in good agreement with literature.

Table 7: Specific surface area (SSA) compared with the literature and the results of the BJH analysis.

Sample	SSA (m ² · g ⁻¹)	SSA Literature (m ² · g ⁻¹)	Pore diameter (nm)	Pore volume (cm ³ · g ⁻¹)
CoMn ₂ O ₄ (M1)	55.77	112 ¹¹	12.18	0.179
CoMn ₂ O ₄ (M2)	89.36	11 ¹²	9.29	0.259
MnCo ₂ O ₄ (M2)	151.23	37 ¹²	5.06	0.263
Vulcan XC72	224.52	222 ⁵⁶	10.00	0.355

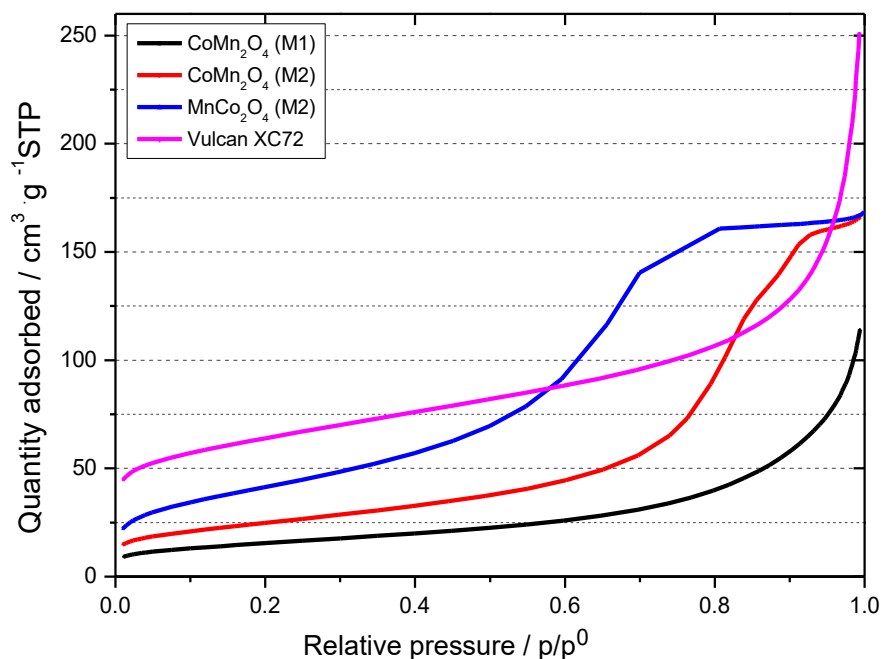


Figure 31: The adsorption isotherms of the catalysts and Vulcan XC72.

4.2 Electrochemical measurements

4.2.1 Cyclic Voltammetry (CV)

For the investigation of the redox processes of the three catalysts CoMn₂O₄ (M1/M2) and MnCo₂O₄ (M2), cyclic voltammetry experiments are conducted in N₂ saturated 0.1 M and 8 M KOH. The measurements are carried out with a scan rate of 10 mV/s at room temperature. Two different catalyst concentrations (0.015 and 0.0196 mg) are applied to the rotating disc electrode (RDE) to see the impact on the electrochemical activity. Additionally, also measurements with Vulcan XC72 only are conducted as reference.

In Figure 32 and 33, the voltammograms of the three catalysts (CoMn_2O_4 (M1/M2), MnCo_2O_4 (M2)) at both loadings (0.015 and 0.0196 mg), are pictured in 0.1 M KOH. At $\sim +0.7$ V, an increase of the current density of all three catalysts occurs, due to the oxygen evolution reactions (OER). Figure 33 shows a small peak of the catalyst CoMn_2O_4 (M1) at +0.3 V caused by the change of oxidation state of the cobalt ion: $\text{Co}^{\text{II}} \leftrightarrow \text{Co}^{\text{III}} + \text{e}^-$,⁵⁷. Figure 34 shows a cyclic voltammetry experiment in the voltage range of -0.7 V until +1.0 V. The experiment is carried out to demonstrate that the increase of the current density starting at -0.1 V is due to the oxygen reduction reactions (ORR). For this purpose, only the anodic sweep is conducted at first, started and ended at the OCV, and then, the electrolyte is purged with N_2 gas for 15 minutes to remove O_2 . After that, only the cathodic sweep is conducted, which is again started and ended at the OCV. Three cycles are operated in this manner. In the first cathodic sweep, there is still some oxygen available for reduction. Therefore, the peak at -0.3 V still occurred but it is smaller than in Figure 33. During the following sweeps, no oxygen was available and the peak vanished. This confirms that these peaks only occur due to the ORR.

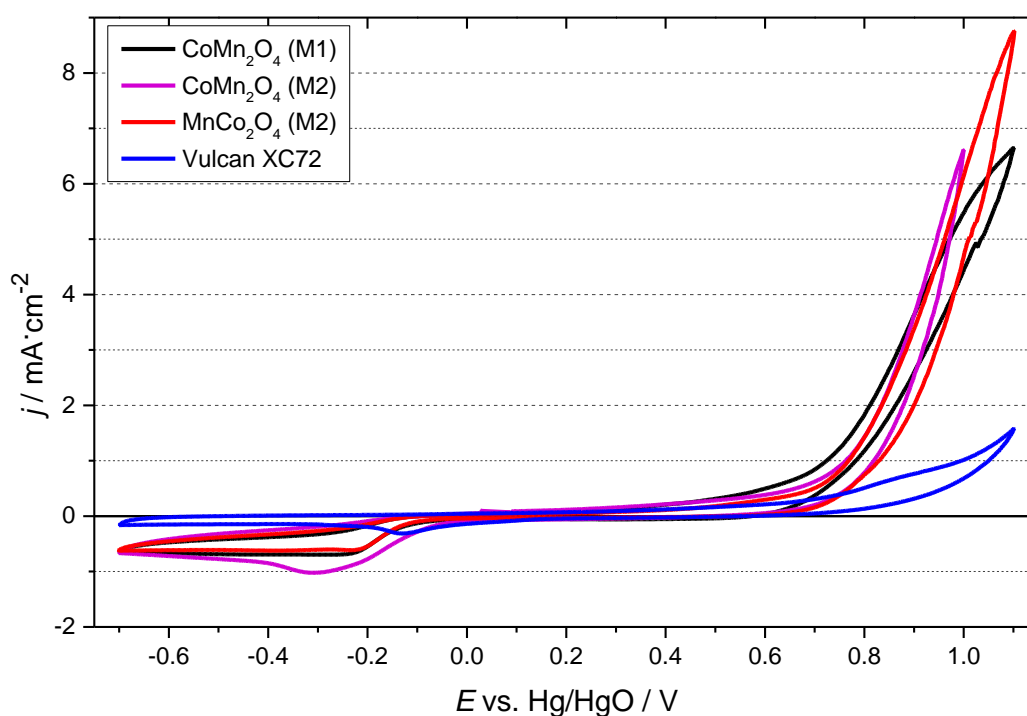


Figure 32: Comparison of the cyclic voltammograms of the three catalysts ($c = 0.015$ mg) and the pure electrode coated with Vulcan XC72 ($c = 0.035$ mg), 0.1 M KOH, $v = 10$ mV/s, cycle 2.

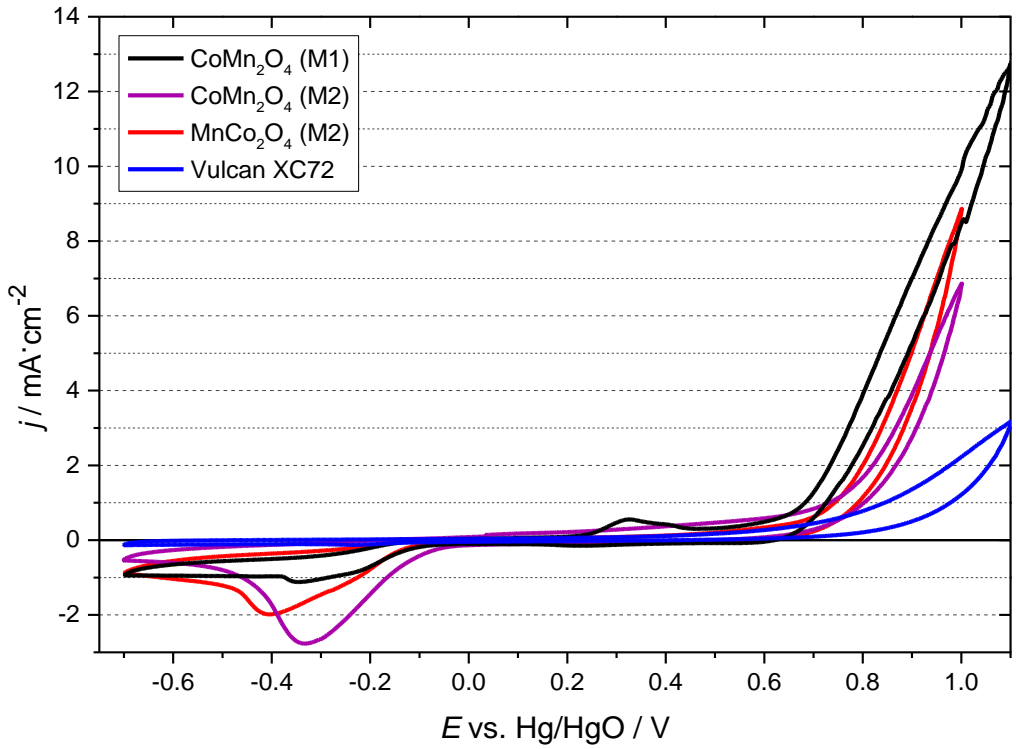


Figure 33: Comparison of the cyclic voltammograms of the three catalysts ($c = 0.0196$ mg) and the pure electrode coated with Vulcan XC72 ($c = 0.045$ mg), 0.1 M KOH, $v = 10$ mV/s, cycle 2.

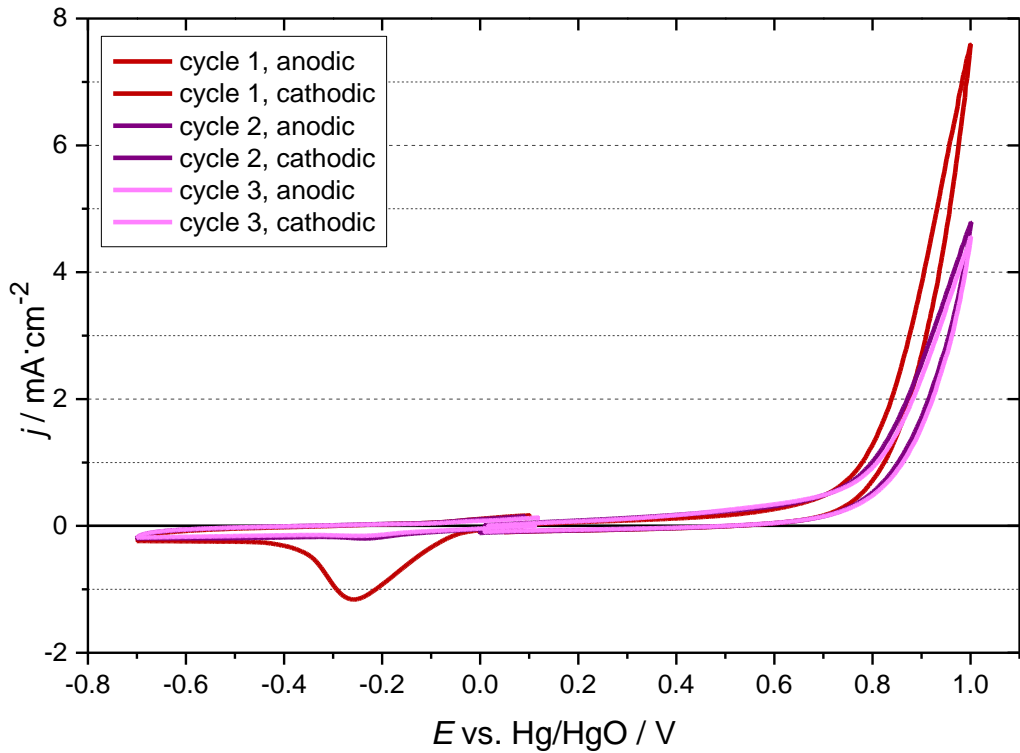


Figure 34: Cyclic voltammograms of CoMn_2O_4 (M2, $c = 0.0196$ mg), cathodic/anodic sweep only, 0.1 M KOH, $v = 10$ mV/s, 3 cycles.

Figures 35 and 36 show the results of the cyclic voltammetry experiments of the three catalysts at different loadings (0.015 and 0.0196 mg) and of Vulcan XC72 as reference (0.035 and 0.045 mg) conducted in 8 M KOH. The highest current density is achieved with the CoMn_2O_4 (M2) catalyst and a catalyst loading of 0.0196 mg. The second highest current density has the MnCo_2O_4 (M2) catalyst at the same catalyst loading. For the lower catalyst loading, a different behaviour is observed. The MnCo_2O_4 (M2) catalyst has the highest current density and the CoMn_2O_4 (M2) the second highest. In general, the current density is much higher in 8 M KOH than in 0.1 M KOH, since the ionic conductivity in 8 M KOH is increased.

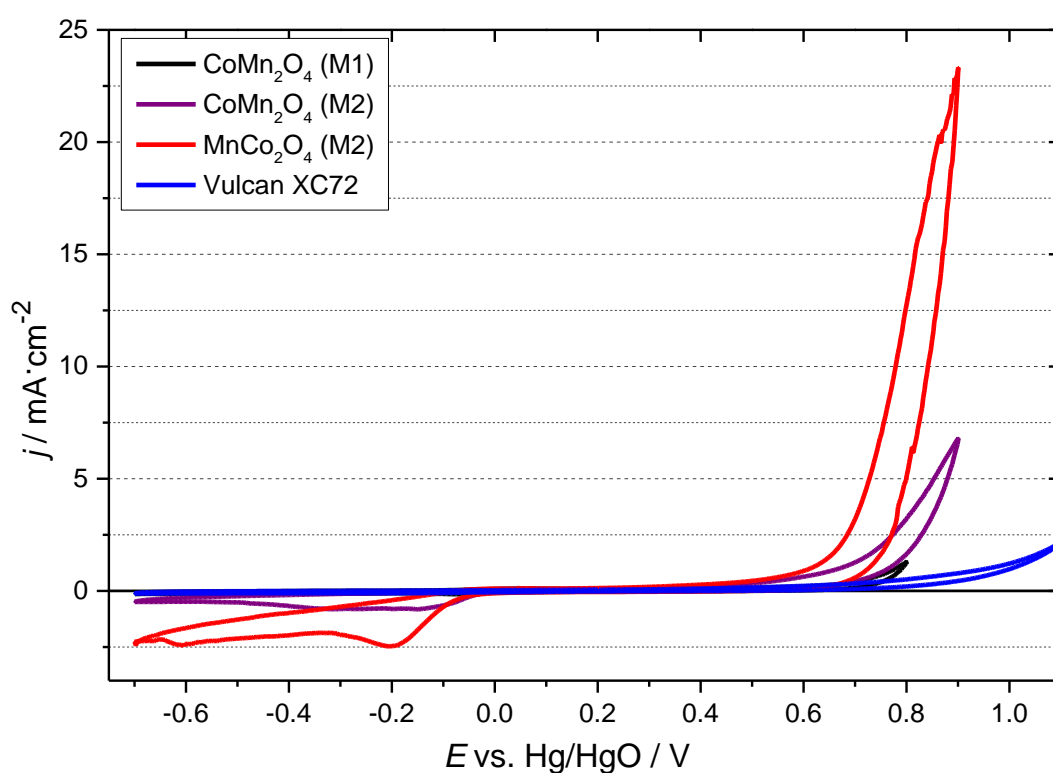


Figure 35: Comparison of the cyclic voltammograms of the three catalysts ($c = 0.015$ mg) and the pure electrode coated with Vulcan XC72 ($c = 0.035$ mg), 8 M KOH, $v = 10$ mV/s, cycle 2.

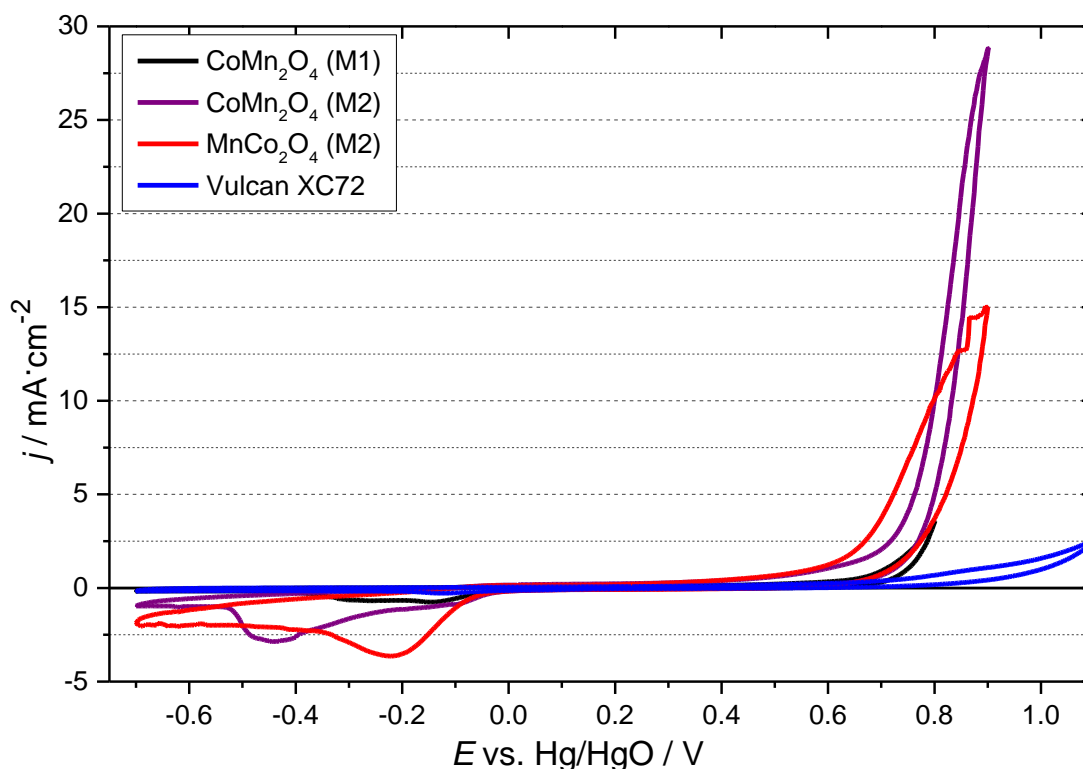


Figure 36: Comparison of the cyclic voltammograms of the three catalysts ($c = 0.0196$ mg) and the pure electrode coated with Vulcan XC72 ($c = 0.045$ mg), 8 M KOH, $v = 10$ mV/s, cycle 2.

4.2.2 Oxygen Evolution Reactions (OER)

In the following Figures 37-47, voltammograms of the oxygen evolution reactions (OER) of the three synthesized catalysts CoMn_2O_4 (M1/M2), MnCo_2O_4 (M2) and of Vulcan XC72 are shown. The measurements are conducted in N_2 saturated 0.1 M and 8 M KOH at room temperature. The Figures 37 and 38 show the OER voltammograms of the three catalysts at two different concentrations (0.015 and 0.0196 mg) and of the Vulcan XC72 (0.035 and 0.045 mg) in 0.1 M KOH. Since Vulcan XC72 is added to the catalyst slurry, measurements were also conducted with Vulcan XC72 as reference. In Figure 39, a comparison between the two catalyst loadings can be seen. The lowest overpotential, steepest slope and highest current density is achieved with the CoMn_2O_4 (M1) catalyst (Figure 39). The two other catalysts, synthesized with the second method (M2), are behaving rather similar except that the MnCo_2O_4 (M2) catalyst shows a steeper slope at higher loading than the CoMn_2O_4 (M2).

Figure 40 shows the first and fifth sweep of the OER measurements of the three catalysts with the higher catalyst loading in 0.1 M KOH at 1600 rpm. From the first to the fifth sweep, the overpotential increases and the current density decreases. The difference is even higher for measurements conducted at lower rotation rates (400 rpm), as it can be seen in Figure 41. At 1600 rpm, higher current density can be achieved compared to 400 rpm, since the diffusion layer is directly proportional to the rotation rate. The higher the rotation rate, the thinner the diffusion layer.

Figure 42 and 43 show the OER voltammograms in 8 M KOH at different catalyst loadings (0.015 and 0.0196 mg) and of Vulcan XC72 (0.035 and 0.045 mg) as reference. The two CoMn_2O_4 (M1/M2) catalysts have approximately the same overpotential. In Figure 44, a comparison of the two catalyst loadings can be seen. The best results are achieved with the MnCo_2O_4 (M2) catalyst, due to the highest specific surface area. The second highest current density obtained the CoMn_2O_4 (M2) catalyst at the higher catalyst loading.

Figure 45 shows the OER measurements in different electrolyte concentrations. The higher electrolyte concentration (8 M KOH) results steeper slopes and higher current density of the catalysts since the ionic conductivity is increased at higher OH^- concentration. The overpotentials in 8 M KOH are much lower (~ 0.65 V) than in 0.1 M KOH (~ 0.75 V).

Figure 46 pictures the first and fifth sweep of the voltammograms in 8 M KOH. The difference from the first to the fifth sweep in 8 M KOH is much smaller than in 0.1 M KOH (Figure 40). In Figure 47, the sweeps at different rotation rates (1600 and 400 rpm) in 8 M KOH can be seen. For the CoMn_2O_4 (M1), nearly the same behaviour is observed at 400 and 1600 rpm. In case of the catalysts synthesized with the second method, the sweeps conducted at 400 rpm achieve slightly higher current densities than the ones at 1600 rpm and even the overpotential is slightly lower at the lower rotation rate.

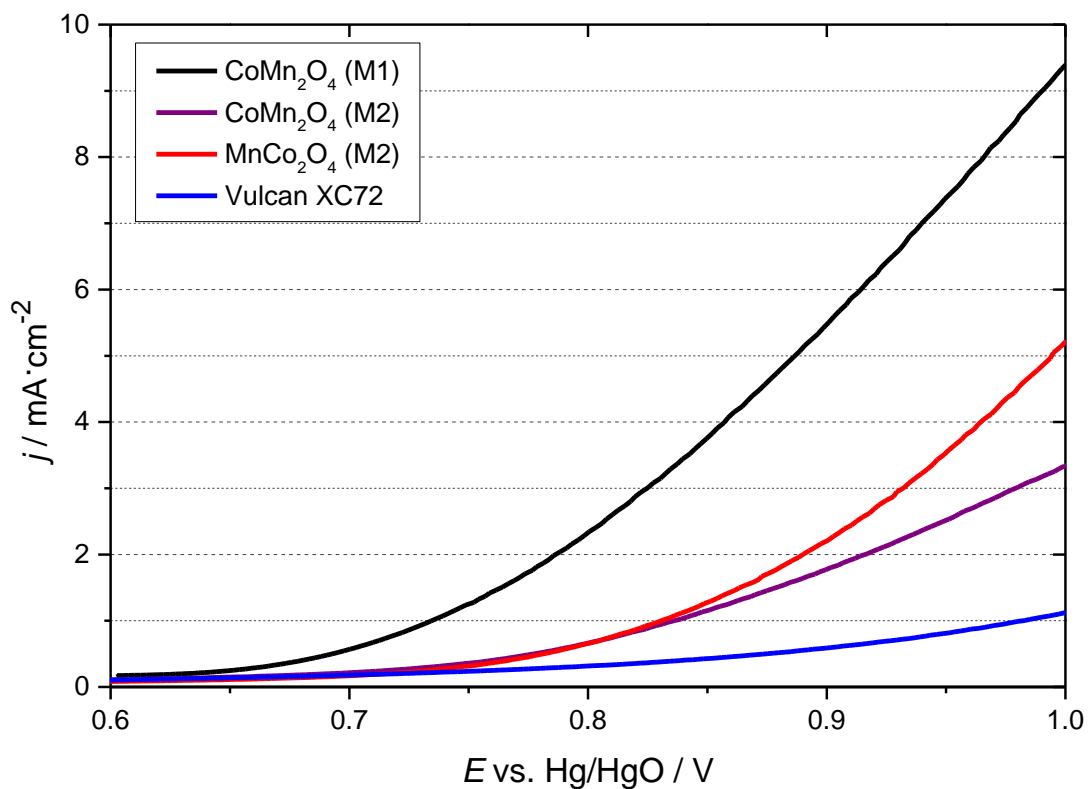


Figure 37: OER voltammograms of the three catalysts ($c = 0.015$ mg) and Vulcan XC72 ($c = 0.035$ mg), 0.1 M KOH, $v = 5$ mV/s, 1600 rpm, Sweep 5.

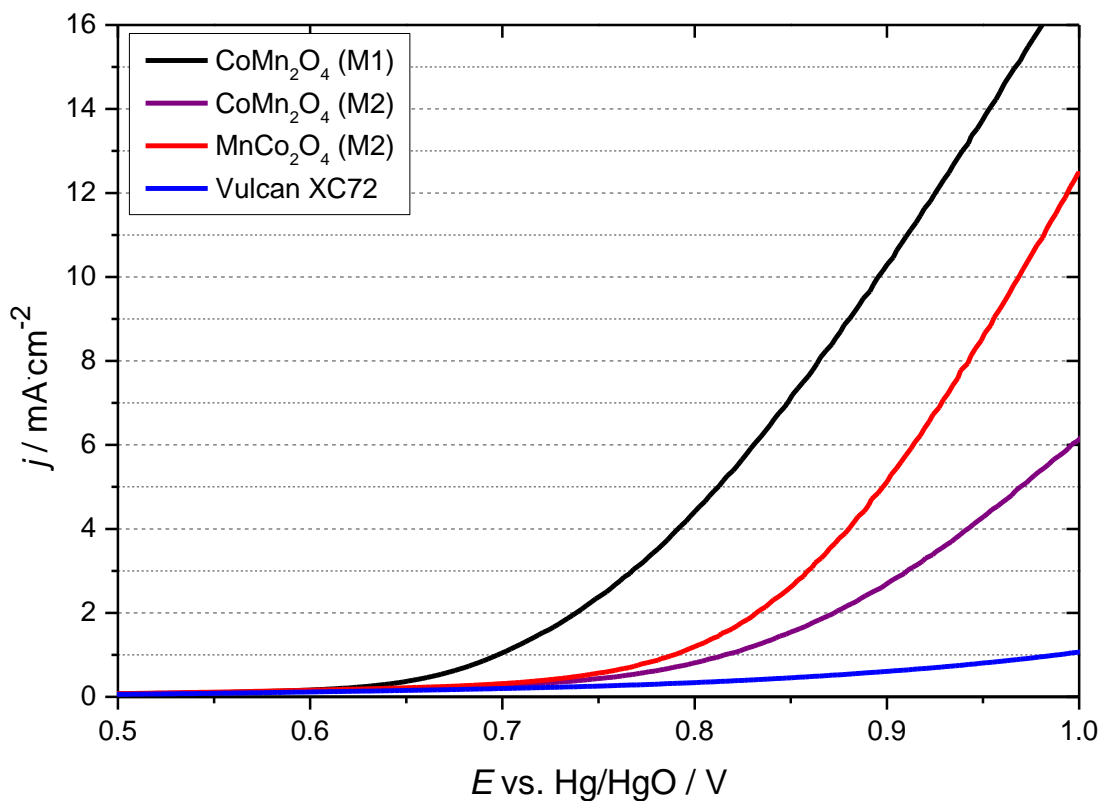


Figure 38: OER voltammograms of the three catalysts ($c = 0.0196$ mg) and Vulcan XC72 ($c = 0.045$ mg), 0.1 M KOH, $v = 5$ mV/s, 1600 rpm, Sweep 5.

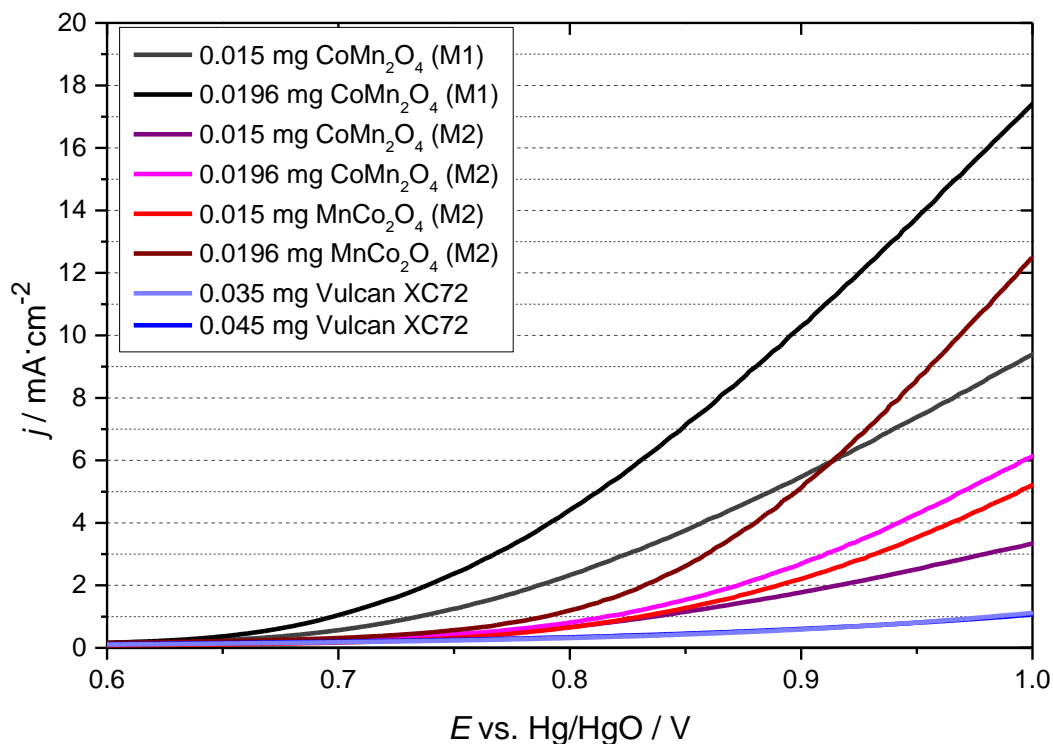


Figure 39: OER voltammograms of the catalysts and Vulcan XC72 at different catalyst loadings in 0.1 M KOH, $v = 5 \text{ mV/s}$, 1600 rpm, Sweep 5.

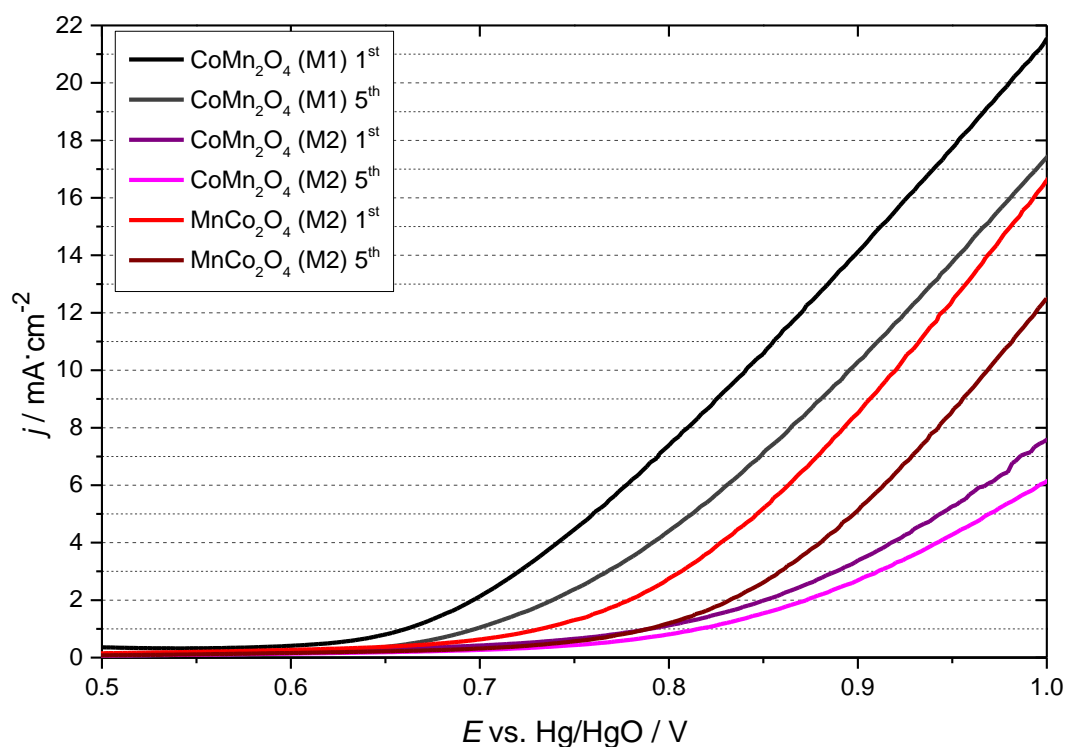


Figure 40: Comparison of the OER voltammograms of the first and fifth sweep of the three catalysts ($c = 0.0196 \text{ mg}$) in 0.1 M KOH, at 1600 rpm, $v = 5 \text{ mV/s}$.

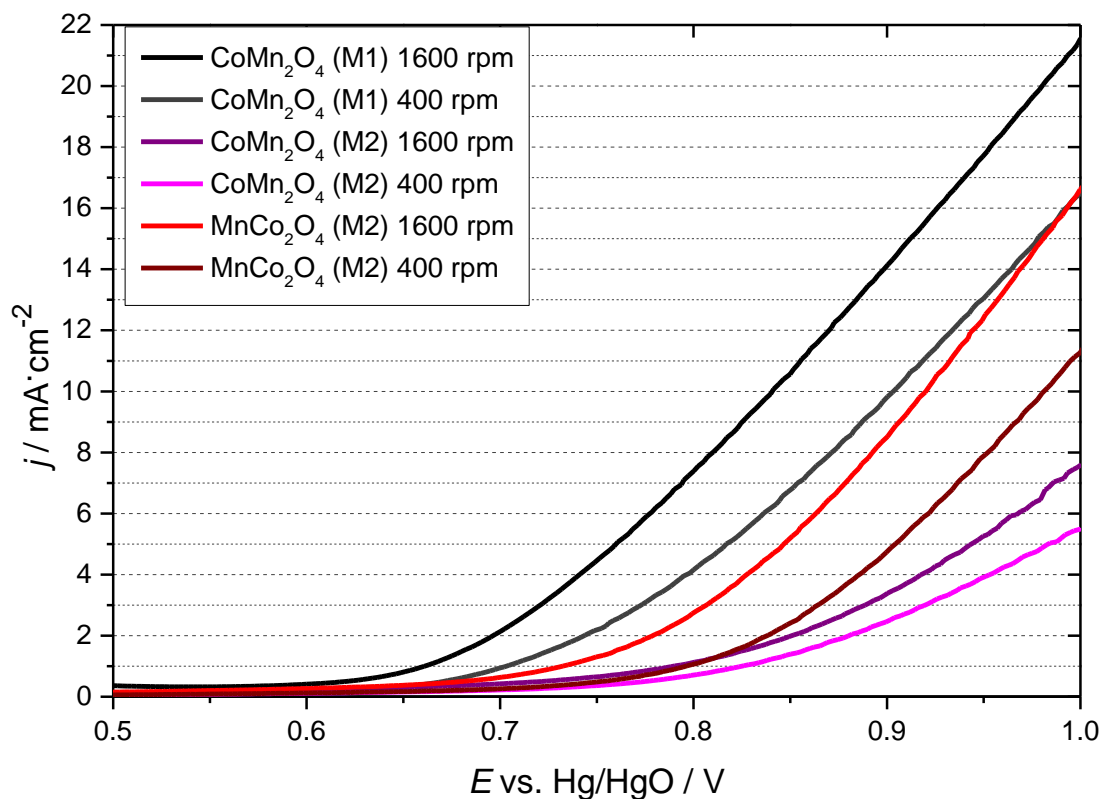


Figure 41: OER voltammograms of the three catalysts ($c=0.0196$ mg) at different rotation rates, 0.1 M KOH, $v = 5$ mV/s, Sweep 5 (1600 rpm) and Sweep 6 (400 rpm).

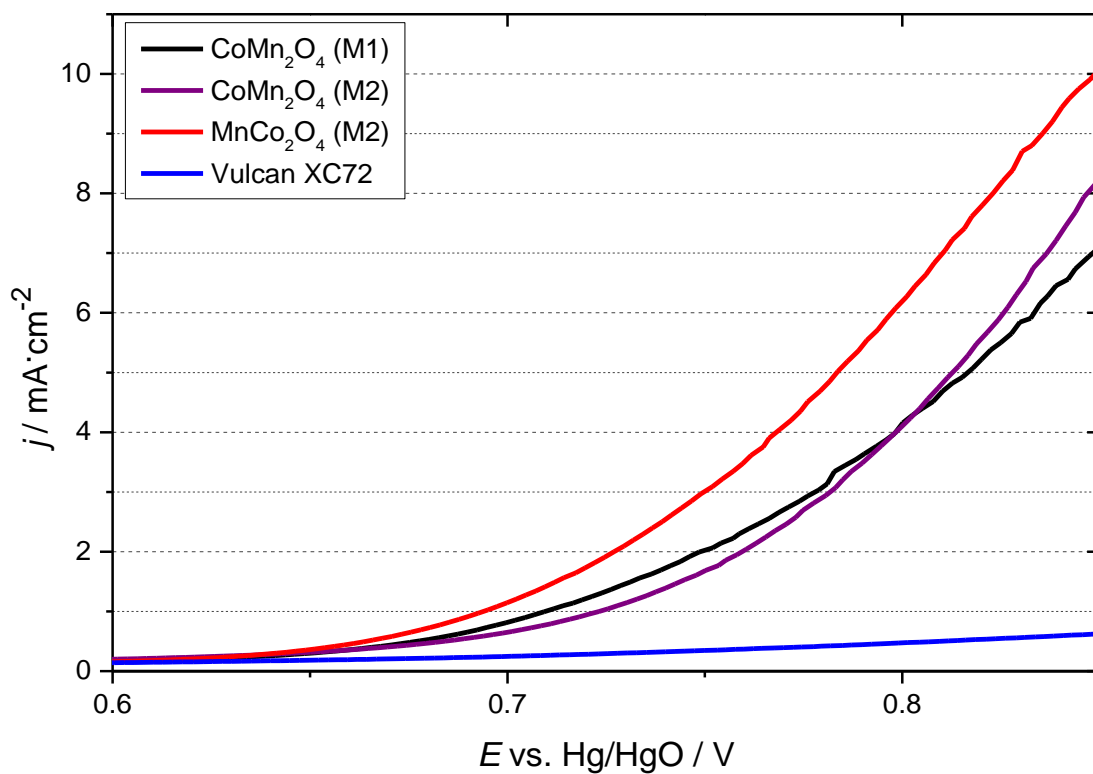


Figure 42: OER voltammograms of the three catalysts ($c = 0.015$ mg) and Vulcan XC72 ($c = 0.035$ mg), 8 M KOH, $v = 5$ mV/s, 1600 rpm, Sweep 5.

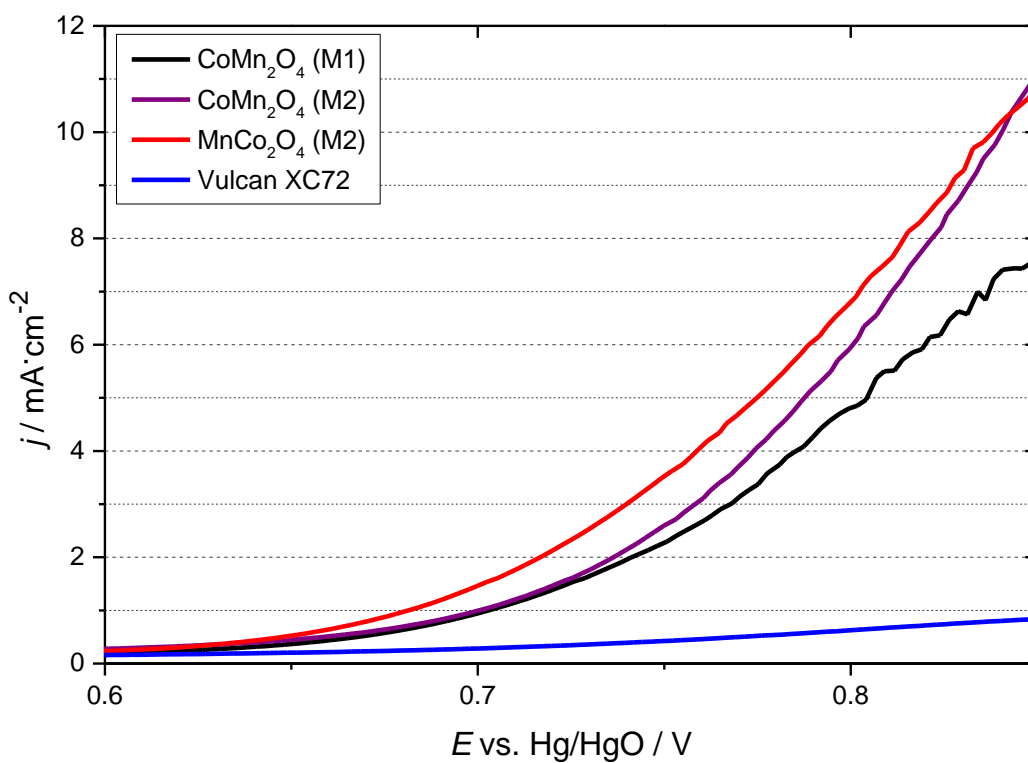


Figure 43: OER voltammograms of the three catalysts ($c=0.0196$ mg) and Vulcan XC72 ($c = 0.045$ mg), 8 M KOH $v = 5$ mV/s, 1600 rpm, Sweep 5.

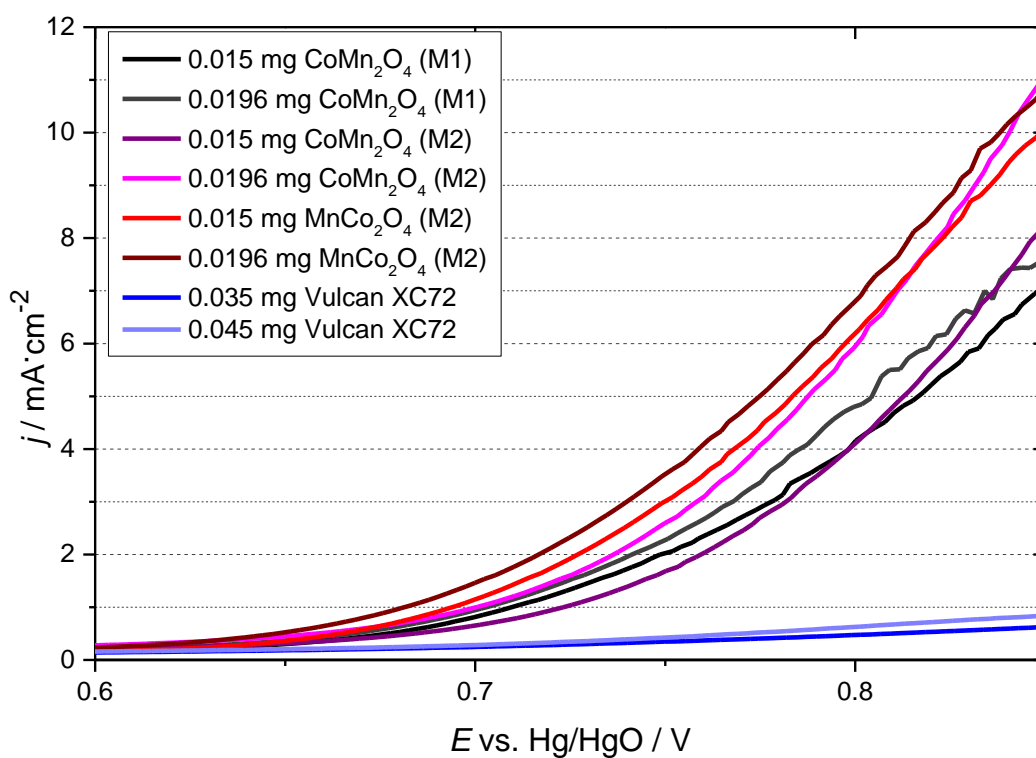


Figure 44: OER voltammograms of the catalysts and Vulcan XC72 at different loadings, 8 M KOH, $v = 5$ mV/s, 1600 rpm, Sweep 5.

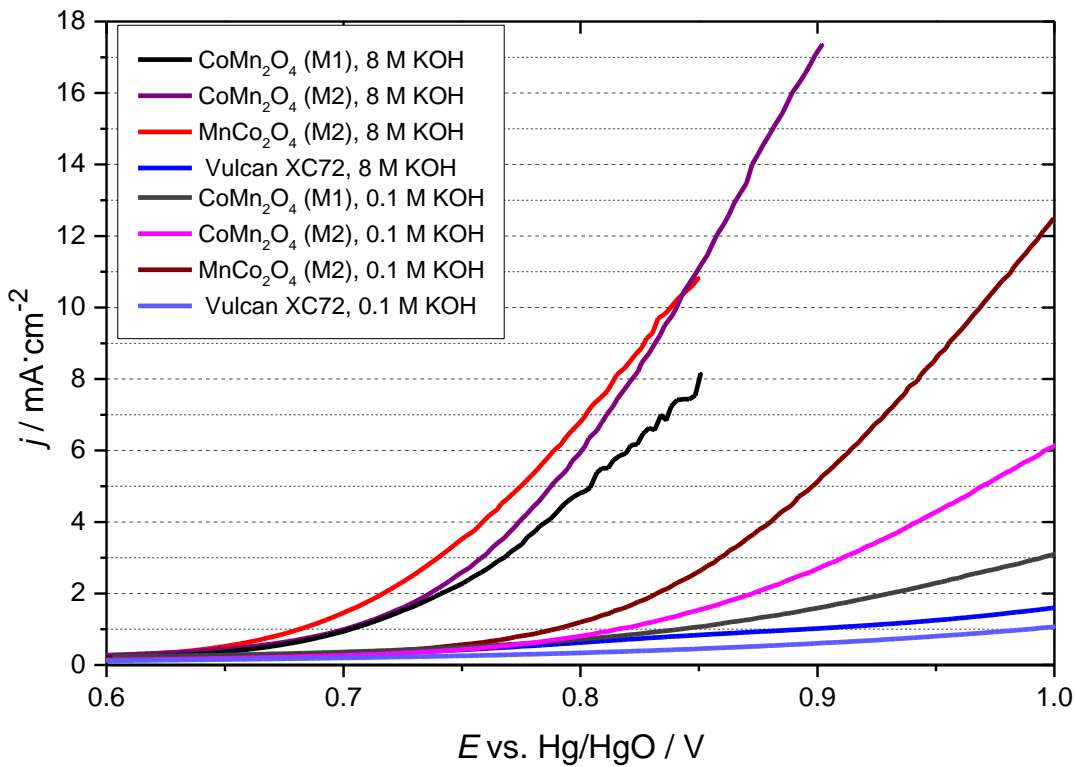


Figure 45: Comparison of the OER voltammograms of the catalysts ($c = 0.0196$ mg) in different electrolyte concentrations, $v = 5$ mV/s, 1600 rpm, Sweep 5.

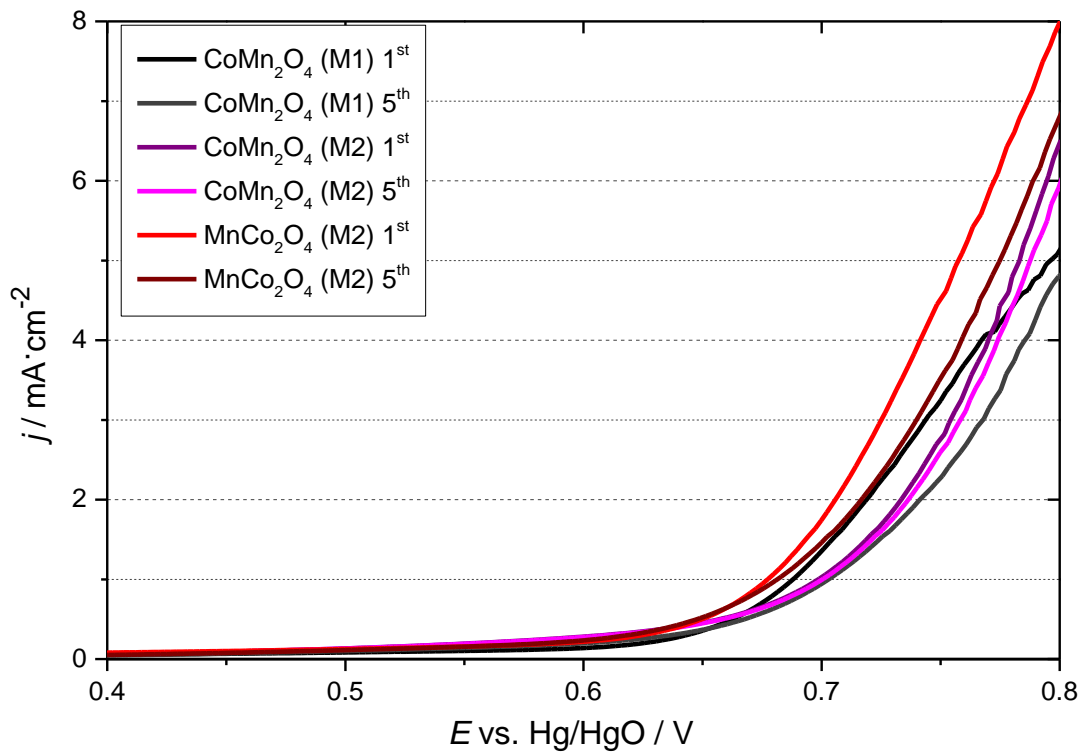


Figure 46: Comparison of the OER voltammograms at the first and fifth sweep of the three catalysts ($c = 0.0196$ mg), in 8 M KOH, $v = 5$ mV/s, 1600 rpm.

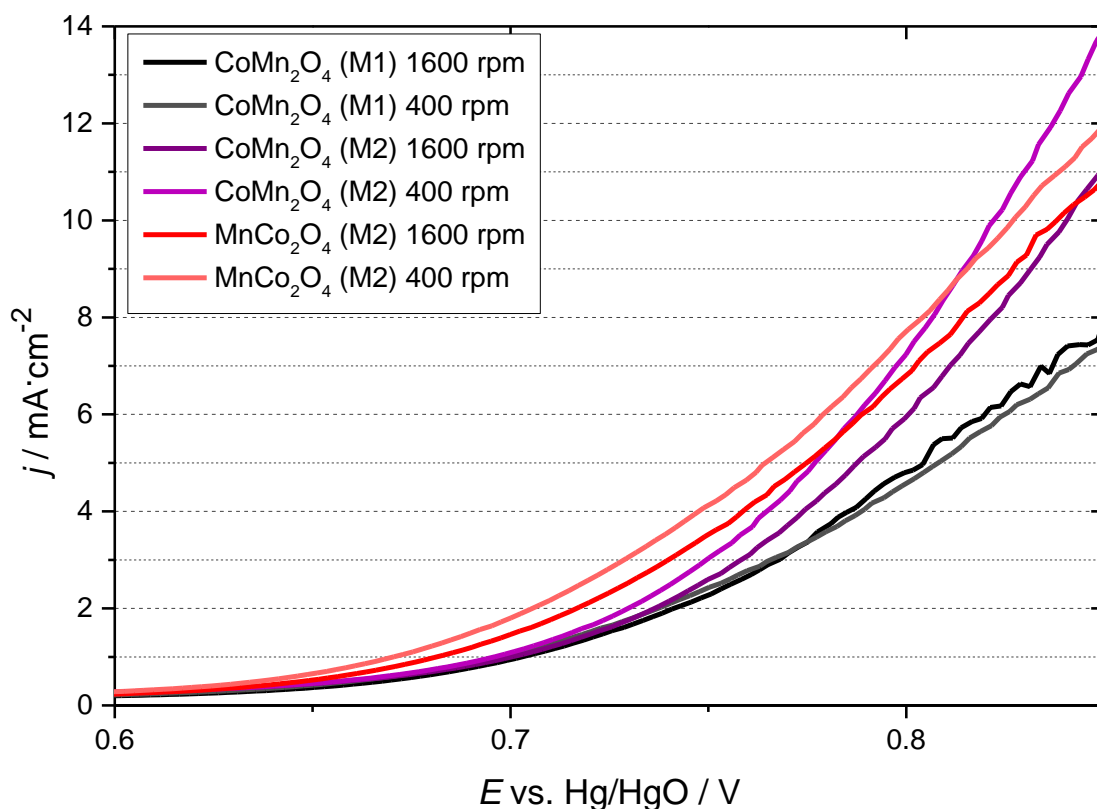


Figure 47: OER voltammograms of the three catalysts ($c = 0.0196$ mg) at different rotation rates, 8 M KOH, $v = 5$ mV/s, Sweep 5 (1600 rpm) and Sweep 6 (400 rpm).

4.2.3 Oxygen Reduction Reactions (ORR)

In Figures 48 and 49, the ORR measurements of the three catalysts (CoMn₂O₄ (M1/M2), MnCo₂O₄ (M2)) at two different catalyst loadings (0.015 and 0.0196 mg) are compared to the Vulcan XC72 (0.035 and 0.045 mg). In the lower catalyst loading, the achieved current density of the three catalysts is approximately the same (~ 2 mA/cm²) and that of Vulcan XC72 is much lower (Figure 48). The measurements with the higher catalyst loading (Figure 49) have increased current density and the individual catalysts differ more than in the lower loading. Figure 50 shows the comparison of the voltammograms of the different catalyst loadings. In the higher catalyst loading, CoMn₂O₄ (M2) and MnCo₂O₄ (M2) have the same overpotential (~ -0.05 V) and CoMn₂O₄ (M1) and Vulcan XC72 have the same one (-0.11 V), as well. The highest current density is achieved by the MnCo₂O₄ (M2) catalyst and the second highest by the CoMn₂O₄ (M2) catalyst for the higher catalyst loading.

In case of the CoMn_2O_4 (M1) catalyst, there is not much difference between the achieved current densities of both catalyst loadings and even the overpotential is the same.

Figure 51 shows the first and fifth sweep of the ORR measurements of the three catalysts in 0.1 M KOH. From the first to the fifth sweep, the current density decreases and the overpotential increases, but apart from this, the measurements are very regular.

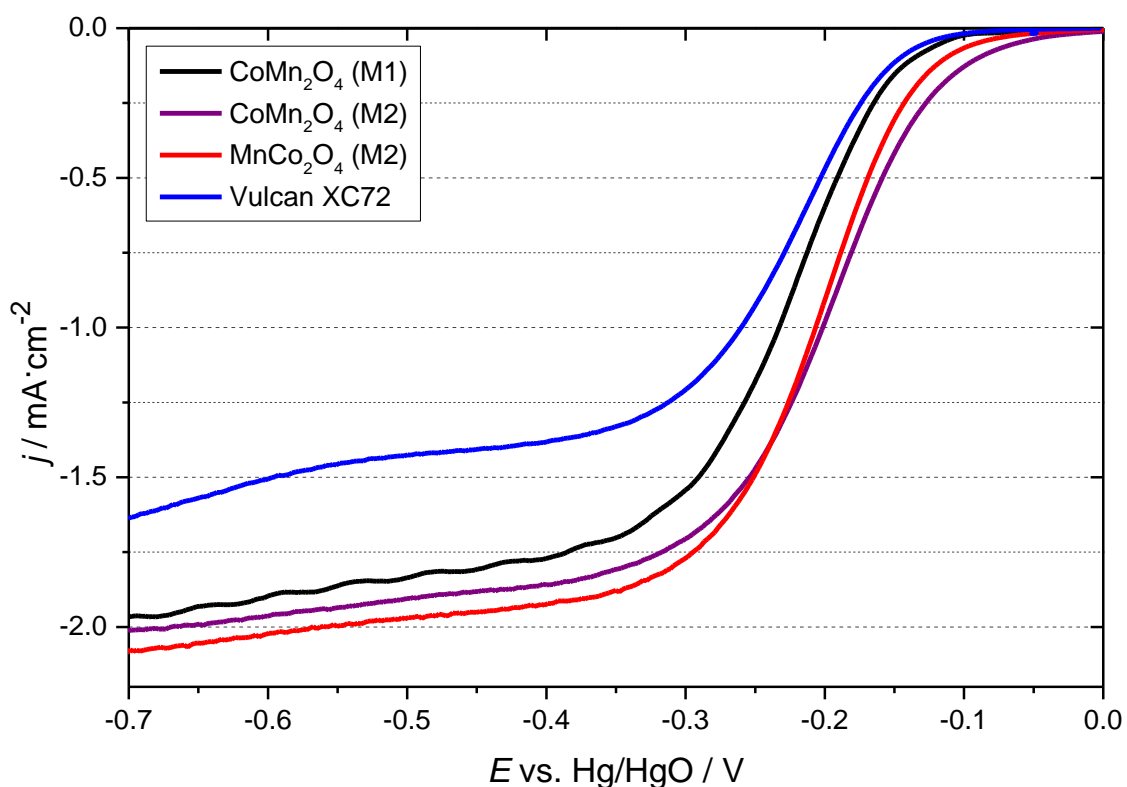


Figure 48: ORR voltammograms of the catalysts ($c = 0.015 \text{ mg}$) in comparison with Vulcan XC72 ($c = 0.035 \text{ mg}$), 0.1 M KOH, $v = 5 \text{ mV/s}$, 1600 rpm, Sweep 5.

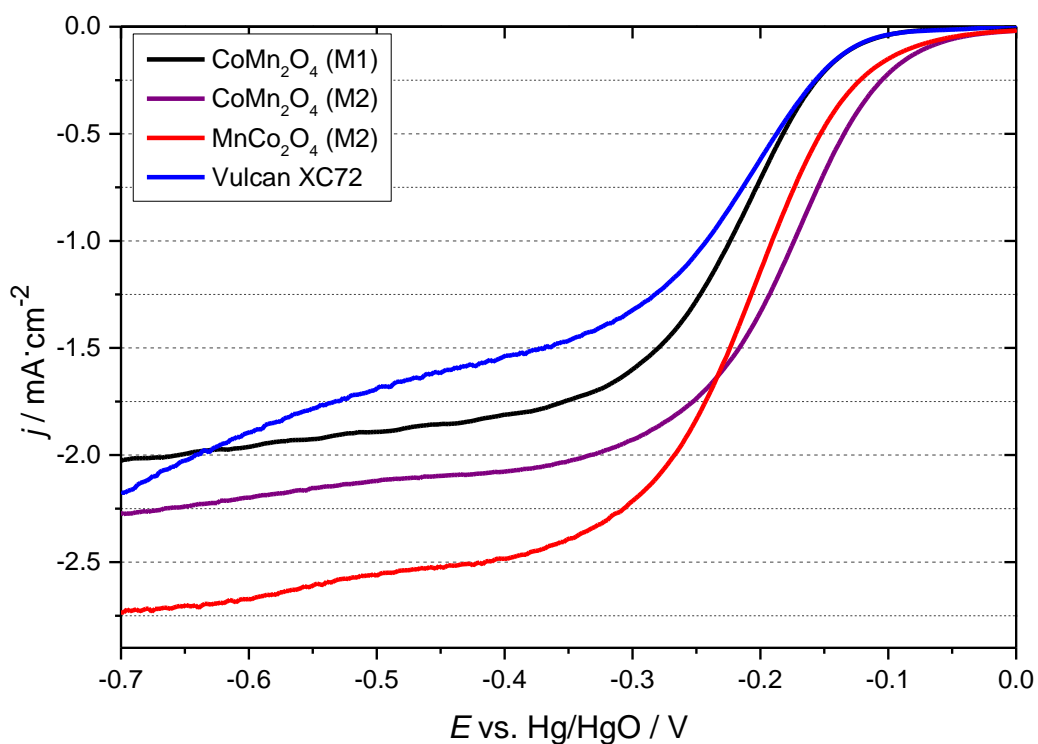


Figure 49: ORR voltammograms of the catalysts ($c = 0.0196$ mg) in comparison with Vulcan XC72 ($c = 0.045$ mg), 0.1 M KOH, $v = 5$ mV/s, 1600 rpm, Sweep 5.

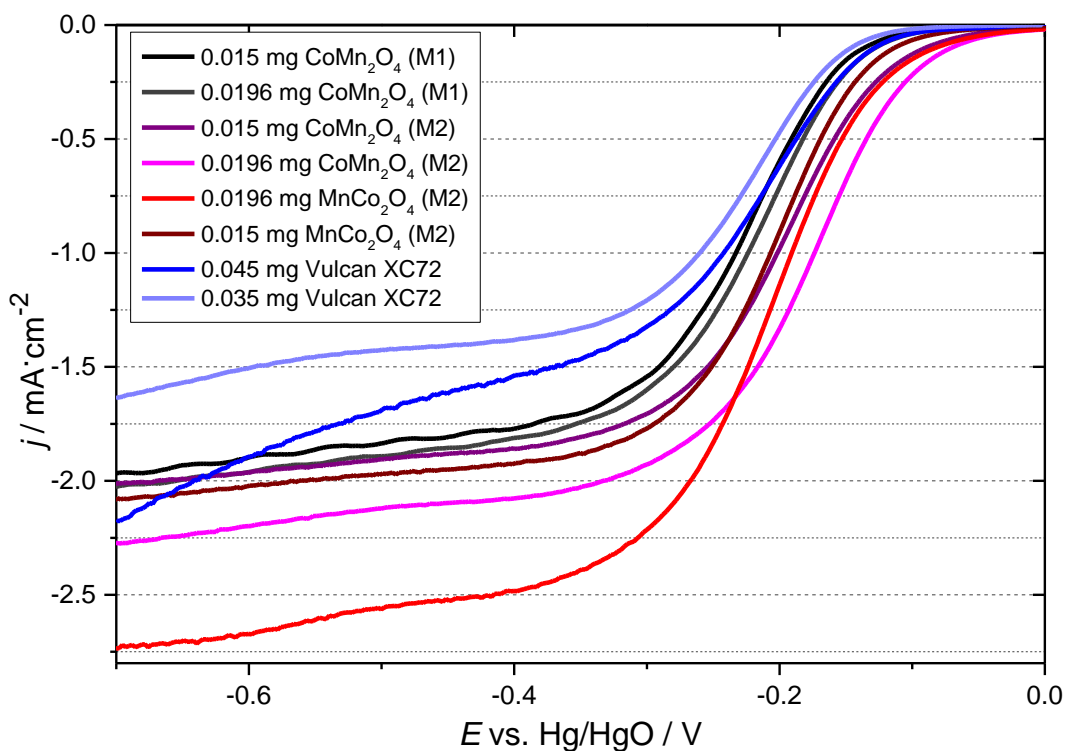


Figure 50: ORR voltammograms of the catalysts and Vulcan XC72 with different loadings, 0.1 M KOH, $v = 5$ mV/s, 1600 rpm, Sweep 5.

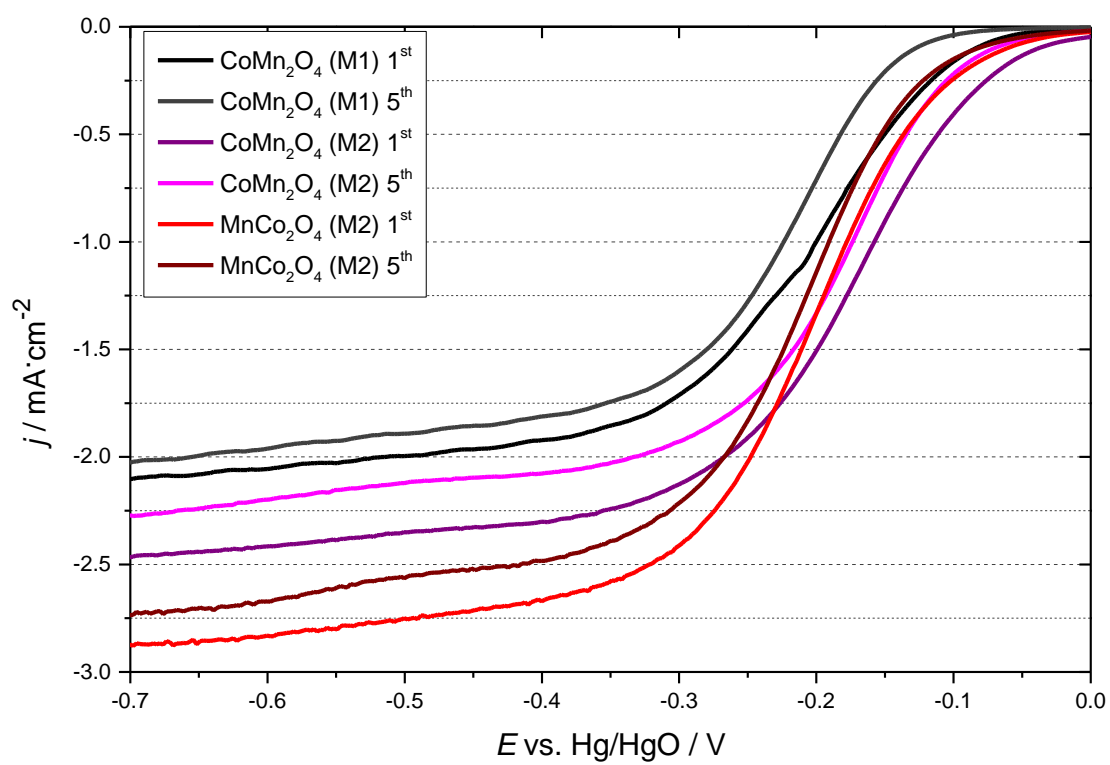


Figure 51: Comparison of the ORR voltammograms of the three catalysts ($c=0.0196$ mg) of the first and fifth sweep at 1600 rpm, 0.1 M KOH $v = 5$ mV/s.

For the Koutecky-Levich analysis, ORR measurements of the three catalysts are conducted at different rotation rates (100, 400, 900, 1600 and 2500 rpm) in 0.1 M KOH (Figures 52 and 53) as well as in 8 M KOH (Figures 59 and 60). As a reference, ORR voltammograms of Vulcan XC72 in 0.1 M KOH are also implemented (Figure 53, right). In these measurements, the influence of the rotation rate on the kinetics of the oxygen reduction reaction can be seen. With increasing rotation rate, the current density increases too, because of the decreased diffusion layer and increased electron transport.

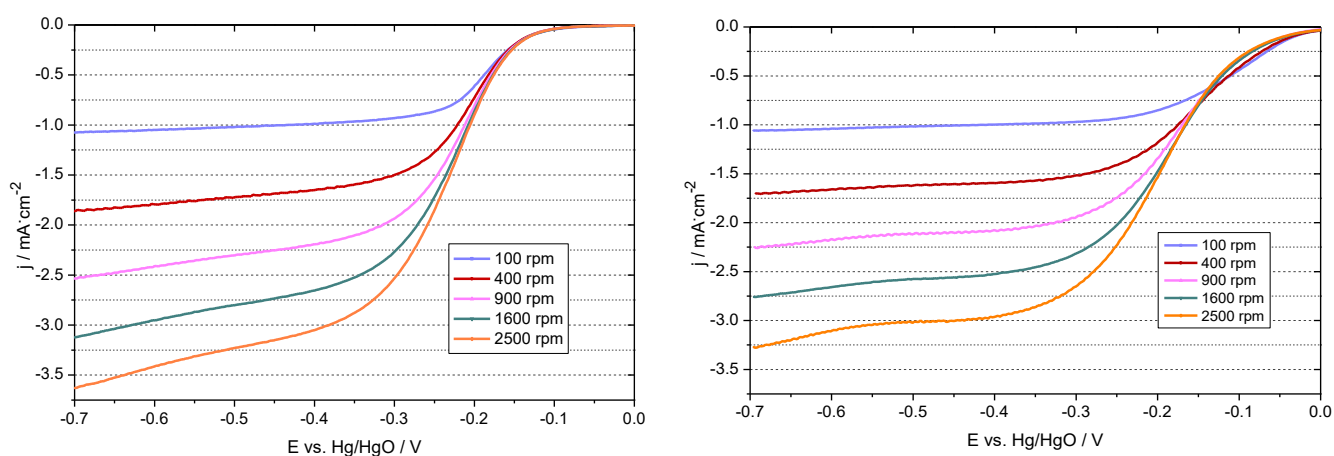


Figure 52: ORR voltammograms for Koutecky–Levich plot, CoMn_2O_4 (M1 (left) and M2 (right)) ($c = 0.0196$ mg), 0.1 M KOH, $v = 5$ mV/s.

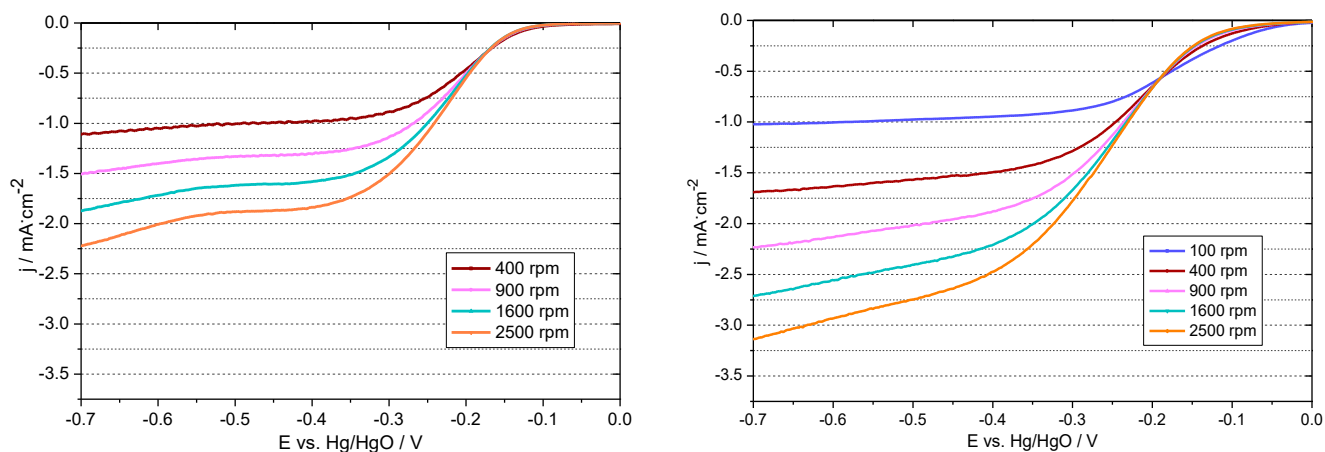


Figure 53: ORR voltammograms for Koutecky–Levich plot, MnCo_2O_4 ($c = 0.0196$ mg, left) and Vulcan XC72 ($c = 0.035$ mg, right), 0.1 M KOH, $v = 5$ mV/s.

The electrolyte of secondary zinc-air batteries is usually a strong alkaline one, thus the ORR measurements are also conducted in 8 M KOH. Figures 54 to 56 show the voltammograms of the ORR measurements in 8 M KOH at different catalyst loadings (0.015 and 0.0196 mg) compared to pure Vulcan XC72 (0.035 and 0.045 mg). The first peak at around -0.1 V is due to the Vulcan XC72. The second peak around -0.4 V is because of the H₂O₂ production at the glassy carbon disc²². At the lower catalyst loading (Figure 54), the highest current density can be obtained by the CoMn₂O₄ (M2) catalyst, whereas in the higher catalyst loading (Figure 55) by MnCo₂O₄ (M2). Both catalysts obtain similar current density at various loadings, which can be seen in Figure 56, where the comparison of the catalysts and Vulcan XC72 at different catalyst loadings is plotted.

Figure 57 shows a comparison of the voltammograms between the second and fifth sweep, since the first sweep always deviates from the following ones. It can be seen, that the current density decreases from the second to the fifth sweep. Figure 58 shows the comparison of the three catalysts and of Vulcan XC72 at different electrolyte concentrations (0.1 M and 8 M KOH). The measurements conducted in 0.1 M KOH achieve much higher current density than the one conducted in 8 M KOH that is due to the higher solubility of oxygen in 0.1 M KOH (Table 2).

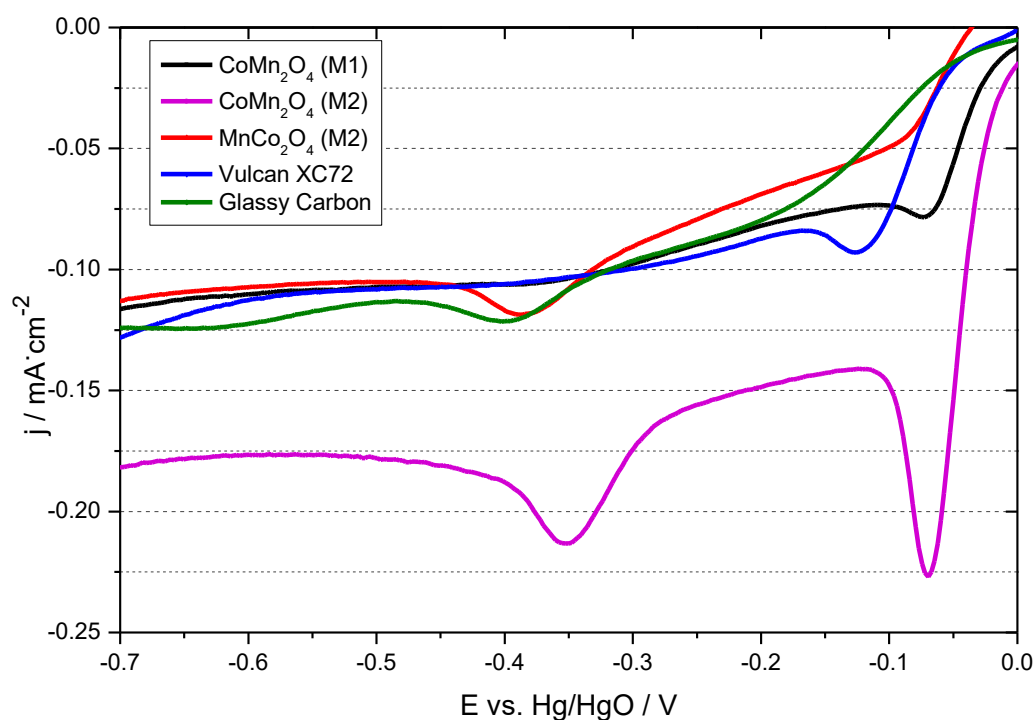


Figure 54: ORR voltammograms of the three catalysts ($c = 0.015$ mg) compared to Vulcan XC72 ($c = 0.035$ mg) and the pure glassy carbon disc, 8 M KOH, $v = 5$ mV/s, 1600 rpm, Sweep 5.

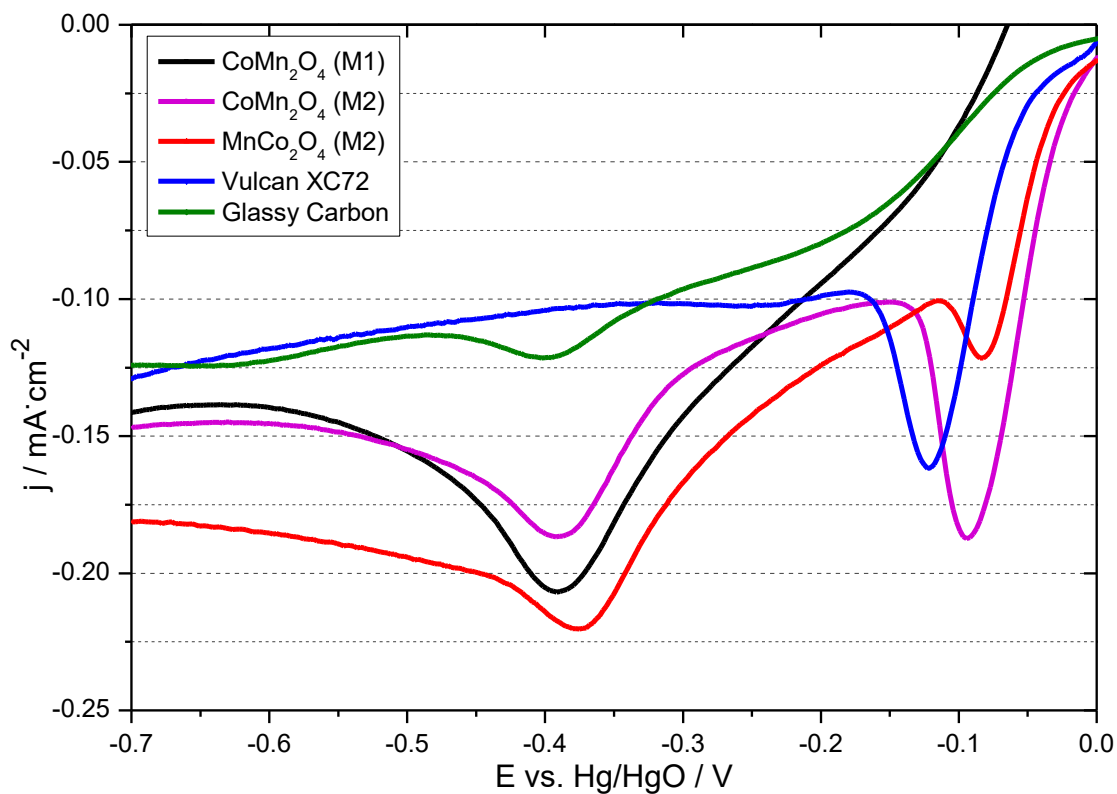


Figure 55: ORR voltammograms of the three catalysts ($c = 0.0196$ mg) compared to Vulcan XC72 ($c = 0.045$ mg) and to the pure glassy carbon disc, 8 M KOH, $v = 5$ mV/s, 1600 rpm, Sweep 5.

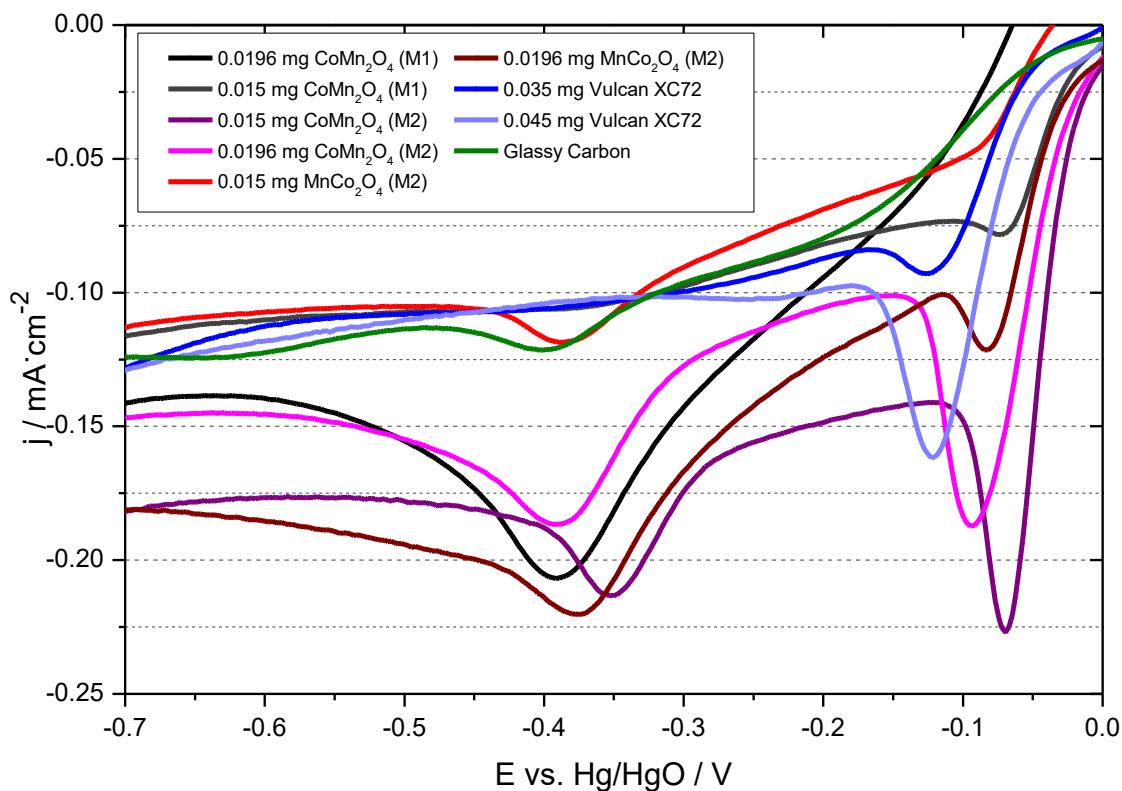


Figure 56: ORR voltammograms of the catalysts and Vulcan XC72 with different loadings and of the glassy carbon electrode, 8 M KOH, $v = 5$ mV/s, 1600 rpm, Sweep 5.

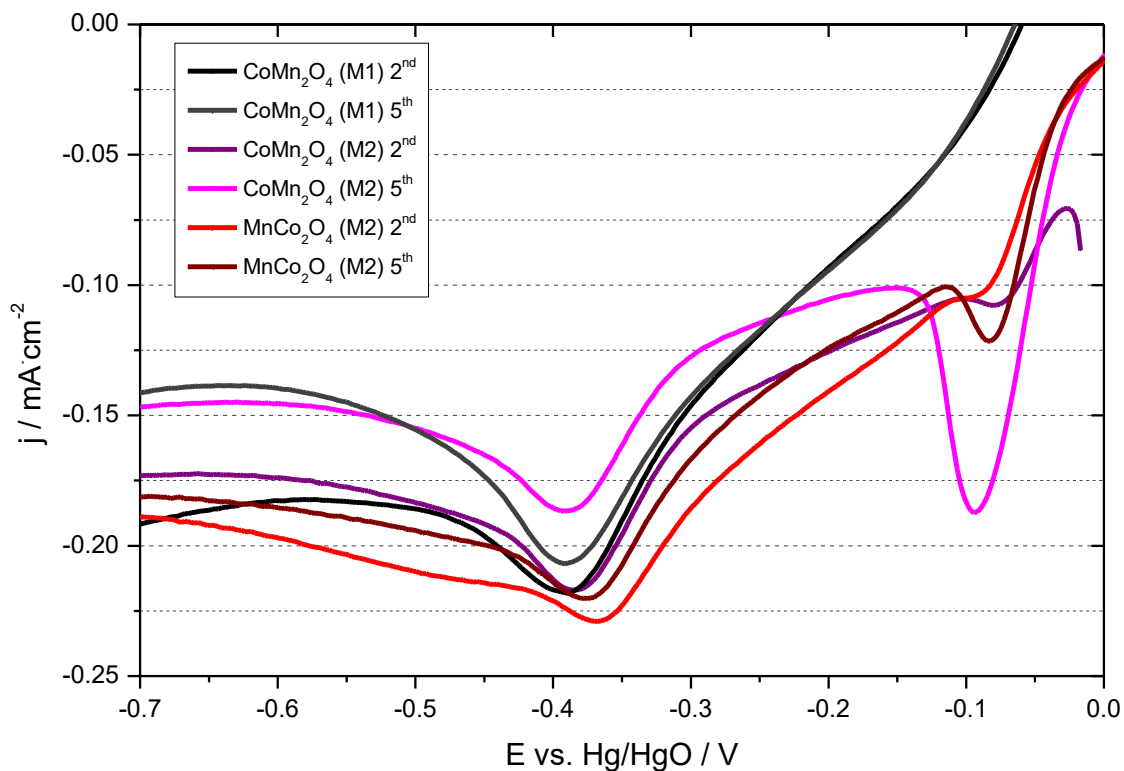


Figure 57: Comparison of the ORR voltammograms of the three catalysts ($c = 0.0196$ mg) of the second and fifth sweep, 8 M KOH, $v = 5$ mV/s, 1600 rpm.

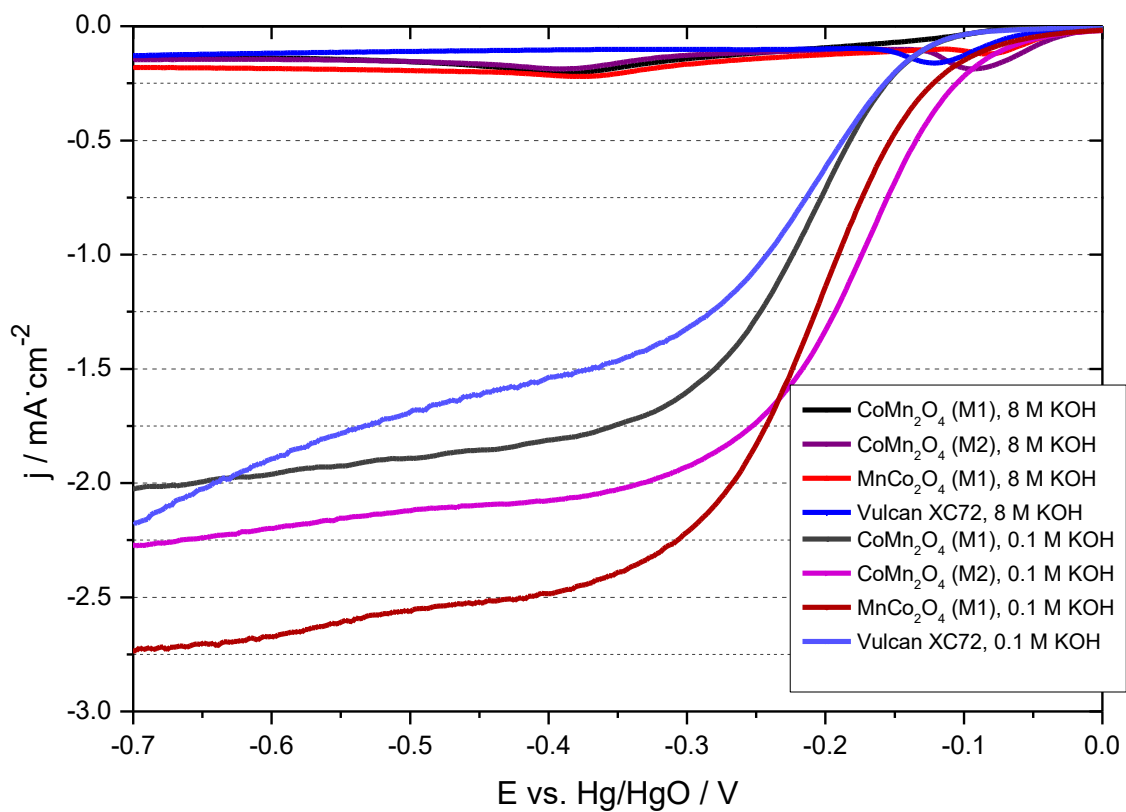


Figure 58: Comparison between the catalysts and the electrolyte concentration, $c = 0.0196$ mg, $v = 5$ mV/s, 1600 rpm, Sweep 5.

In the following Figures 59 and 60, the ORR measurements for the Koutecky-Levich Plot that are conducted at different rotation rates, are shown in 8 M KOH. The highest current density is achieved with the highest rotation rate. The comparison of the three catalysts shows that the MnCo_2O_4 (M2) catalyst has the highest current density which is in good agreement with the BET results. The overpotential of CoMn_2O_4 (M1) decreases with increasing rotation rate whereas for the other two catalysts it does not change. In case of the CoMn_2O_4 (M2) catalyst, there is no increase of limiting current density between the rotation rates 400 and 1600 rpm and therefore, these data are not used for the Koutecky-Levich plot.

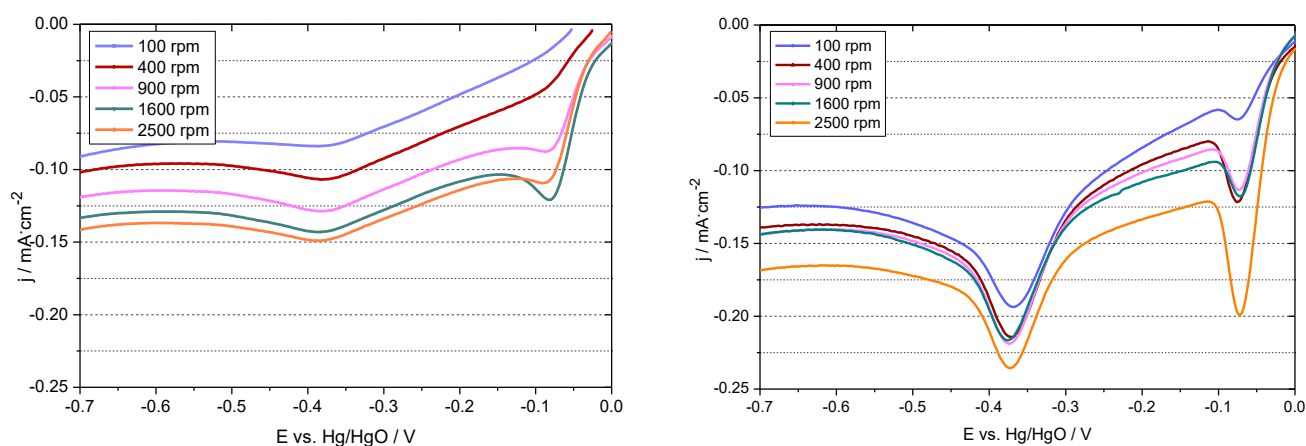


Figure 59: ORR voltammograms for the Koutecky–Levich plot, CoMn_2O_4 (M1) ($c = 0.0196$ mg, left), CoMn_2O_4 (M2) ($c = 0.0196$ mg, right), 8 M KOH, $v = 5$ mV/s.

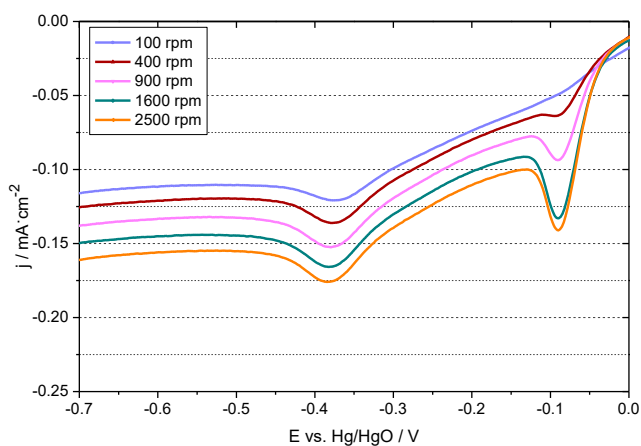


Figure 60: ORR voltammograms for the Koutecky–Levich plot, MnCo_2O_4 (M2) ($c = 0.0196$ mg), 8 M KOH, $v = 5$ mV/s.

4.2.4 Koutecky-Levich Plot

In the following Figure 61 and 62, the Koutecky-Levich plots of the three catalysts and of Vulcan XC72 in 0.1 M KOH, are shown. The reciprocal limiting current densities obtained during the ORR experiments (Figures 52 and 53), read off at -0.55 V, are plotted against the reciprocal square root of the rotation rate. From the slope of the Koutecky-Levich plot, the number of transferred electrons n is calculated according to the equation (27). The Koutecky-Levich plots are straight lines and as they do not intercept at the origin of coordinates, a kinetically limited reaction is obtained.

In Figure 63, a direct comparison of the Koutecky-Levich plots of the three catalysts is shown. The MnCo_2O_4 (M2) and CoMn_2O_4 (M2) catalyst intercepts the vertical axis at a slightly higher reciprocal current density than the other one, which suggests that these two have a higher kinetic limitation than the CoMn_2O_4 (M1).

Table 8 presents the number of calculated transferred electrons in comparison with the values of the literature. For the three catalysts, the results are between 3.3 and 3.6 and in good agreement with the literature. According to the obtained number of transferred electrons, a four-electron way is suggested for the ORR of the three catalysts (CoMn_2O_4 (M1/M2), MnCo_2O_4 (M2)) and a two-electron way in case of Vulcan XC72.

Table 8: The number of transferred electrons in 0.1 M KOH, calculated from the Koutecky-Levich Plot.

Catalyst	slope	n	Literature value
CoMn₂O₄ (M1)	2.63	3.45	3.4 ¹¹
CoMn₂O₄ (M2)	2.53	3.59	3.68 ¹²
MnCo₂O₄ (M2)	2.62	3.34	3.51 ¹²
Vulcan XC72	4.95	1.83	2 ⁵⁸

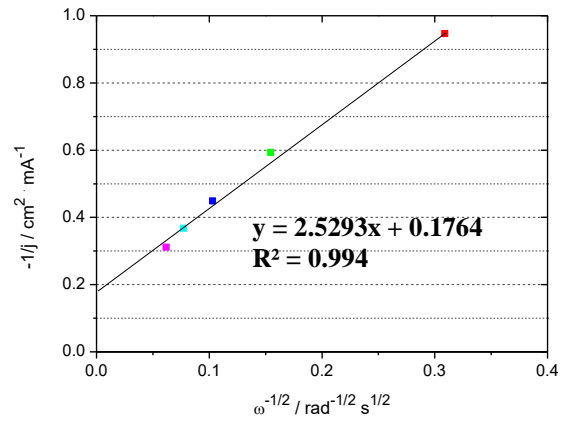
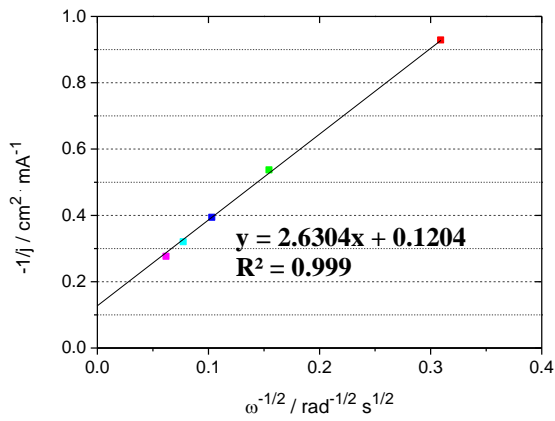


Figure 61: Koutecky-Levich Plot of CoMn_2O_4 (M1) ($c=0.0196$ mg) (left) and CoMn_2O_4 (M2) ($c=0.0196$ mg) (right), 0.1 M KOH, $v = 5$ mV/s.

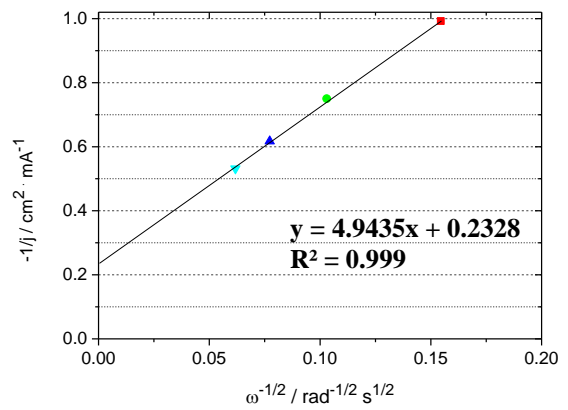
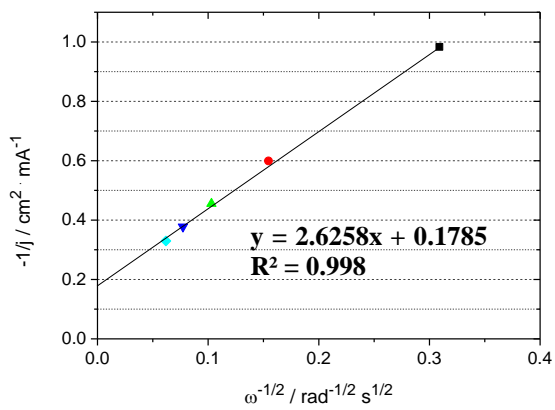


Figure 62: Koutecky-Levich Plot of MnCo_2O_4 (M2) ($c=0.0196$ mg) (left) and Vulcan XC72 ($c=0.035$ mg) (right), 0.1 M KOH, $v = 5$ mV/s.

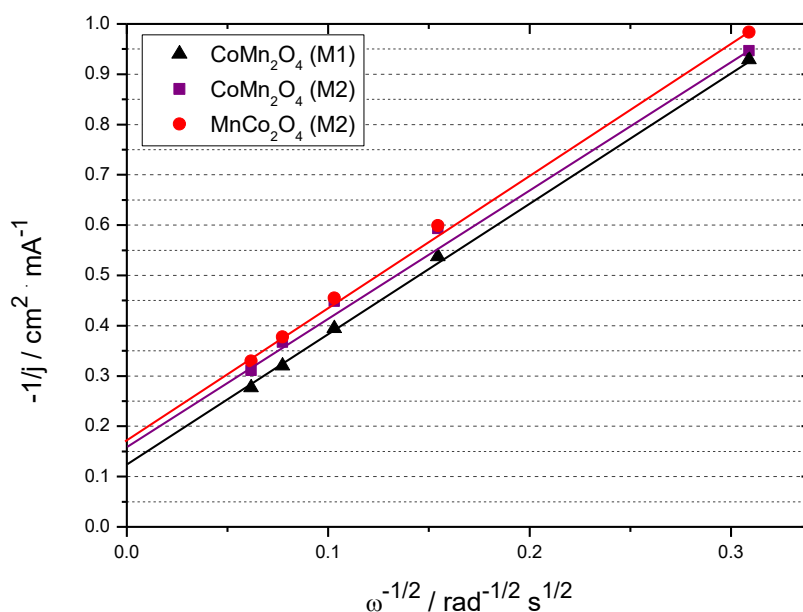


Figure 63: Comparison of the Koutecky-Levich Plots of the three catalysts in 0.1 M KOH, $v = 5 \text{ mV/s}$.

In the Figure 64, the Koutecky-Levich plots of the CoMn_2O_4 (M1) and MnCo_2O_4 (M2) catalysts in O_2 saturated 8 M KOH, are illustrated. The reciprocal limiting current density of 100 rpm is not used for the plot because it would not result in a straight line. The limiting current densities are obtained from the ORR voltammograms at -0.55 V , in Figure 59 (left) and Figure 60. The ORR voltammograms of CoMn_2O_4 (M2) (Figure 59, right) are not evaluated because the limiting current densities do not uniformly increase with increasing rotation rate. Figure 65 shows the comparison of the two Koutecky-Levich plots. Both catalysts intercept the vertical axis at a much higher value than in 0.1 M KOH. Table 9 presents the number of transferred electrons. In 8 M KOH, less electrons are transferred than in 0.1 M KOH, which is in good accordance with the lower current density achieved in 8 M KOH. The reduced number of transferred electrons in 8 M KOH is also described in the literature, where measurements with a Pt electrode were conducted and the number of transferred electrons was 0.99 and 1.87^{59, 60}.

Table 9: The number of transferred electrons in 8 M KOH, calculated from the Koutecky-Levich Plot.

Catalyst	slope	n
CoMn_2O_4 (M1)	32.41	0.53
MnCo_2O_4 (M2)	19.88	0.88

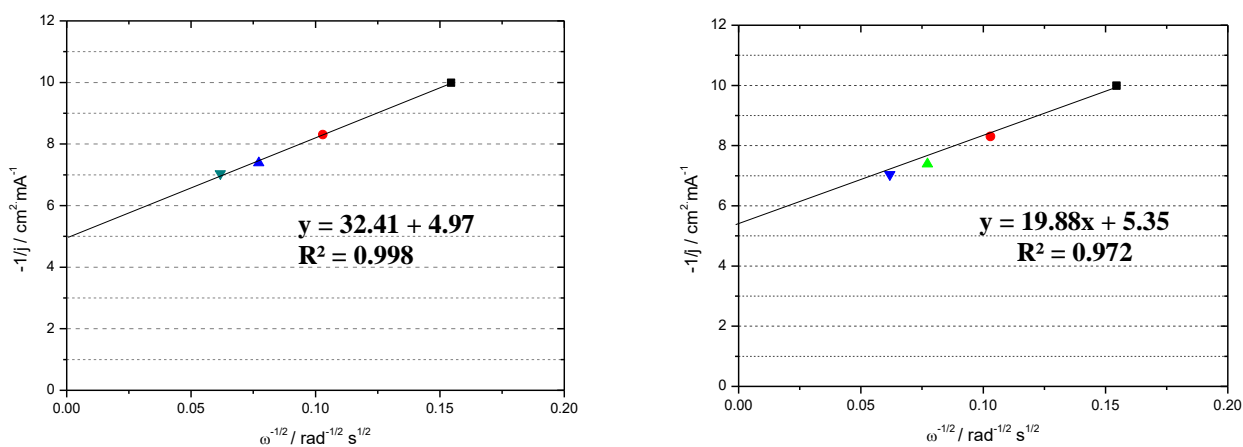


Figure 64: Koutecky-Levich Plot of CoMn_2O_4 (M1, (left)) and MnCo_2O_4 (M2, right), $c = 0.0196 \text{ mg}$, 8 M KOH , $v = 5 \text{ mV/s}$.

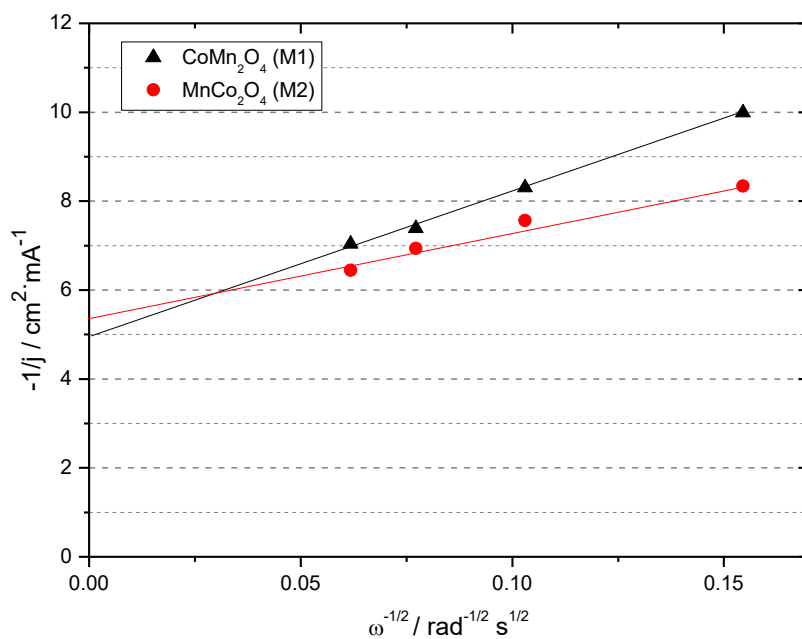


Figure 65: Comparison of the Koutecky-Levich Plots from the two catalysts in 8 M KOH , $v = 5 \text{ mV/s}$.

5 Conclusion

Three different catalysts (CoMn_2O_4 (M1/M2) and MnCo_2O_4 (M2)) were synthesized according to two different methods with the aim to develop a promising bifunctional catalyst for the air electrode of the secondary zinc-air battery. The physicochemical properties of the catalysts were analysed with X-ray diffraction (XRD), scanning electron microscopy (SEM/EDX) and Brunauer-Emmett-Teller (BET) measurements. The electrochemical behaviour has been investigated via cyclic voltammetry (CV) and linear sweep voltammetry (LSV) to study the oxygen evolution- (OER) and oxygen reduction reactions (ORR). The measurements were conducted in a three-electrode setup with a platinum counter electrode and a Hg/HgO reference electrode. A rotating disc electrode (RDE) was coated with the catalyst slurry as working electrode and the measurements were conducted in 0.1 M and 8 M KOH.

The synthesis of the catalysts was carried out with two different methods. For both methods, precursors were prepared. Concerning method M1, the precursor was amorphous MnO_2 , which was prepared via the reduction reaction of $\text{Mn}(\text{CH}_3\text{COO})_2$ with KMnO_4 . Then, it was further reduced with NaBH_4 to the CoMn_2O_4 catalyst. In case of method M2, the $\text{Co}_{0.33}\text{Mn}_{0.67}\text{CO}_3$ and $\text{Mn}_{0.33}\text{Co}_{0.67}\text{CO}_3$ precursors were prepared from cobalt acetate and manganese acetate with $(\text{NH}_4)_2\text{SO}_4$ and NH_4HCO_3 . Both carbonate precursors were prepared with the same method, but for the synthesis of $\text{Mn}_{0.33}\text{Co}_{0.67}\text{CO}_3$, the molar ratio of cobalt- to manganese acetate was reversed. Afterwards, they were annealed at 400°C to obtain the CoMn_2O_4 and MnCo_2O_4 catalysts.

The SEM images of the catalyst synthesized with the first method showed a crushed plate-like morphology. The other two catalysts had a microspheric morphology. The EDX measurements confirmed that only Co, Mn and O were present in different ratios. The CoMn_2O_4 (M1) showed a Co:Mn ratio of 1 to 2.5, the CoMn_2O_4 (M2) had 1 to 3.0 and the MnCo_2O_4 (M2) 1.9 to 1 ratio. The Rietveld refinement of the XRD measurement showed that the catalysts are phase pure samples. The BET results revealed that the CoMn_2O_4 (M1) catalyst synthesized with the first method has a smaller specific surface area (SSA) than the catalysts synthesized with the second method. In comparison with the literature, the CoMn_2O_4 (M2) and MnCo_2O_4 (M2) catalysts obtained a much higher SSA, 89.36 and $151.23 \text{ m}^2 \cdot \text{g}^{-1}$, respectively.

In the cyclic voltammetry measurements, an increase of the current density occurs at +0.7 V for all three catalysts and both catalyst loadings (0.015 and 0.0196 mg), which is due to the OER. The peak of the catalyst CoMn_2O_4 (M1) at + 0.3 V is related to the change of the oxidation state of $\text{Co}^{\text{II}} \leftrightarrow \text{Co}^{\text{III}}$. The peak at -0.3 V, which occurs for all three catalysts, is due to the ORR.

In case of the OER measurements, the best result in 0.1 M KOH was obtained with the CoMn_2O_4 (M1) catalyst. It had the highest current density and the lowest overpotential at both catalyst loadings. The comparison of several sweeps at 1600 rpm showed that the current density decreases and the overpotential of all three catalysts increases with increasing sweep number. The comparison between the rotation rates of 1600 and 400 rpm showed that there was an additional decrease of current density at lower rotation rate. In 8 M KOH, the current density is much higher than in the 0.1 M KOH, due to increased ionic conductivity in higher electrolyte concentration. The overpotentials were decreased by approximately 100 mV in the higher concentration. The best result in 8 M KOH was obtained with the MnCo_2O_4 (M2) catalyst, which has the highest SSA. The comparison between the first and fifth sweep of the catalysts in 8 M KOH showed that there is no increase of the overpotential and only a small decrease of the current density at the fifth sweep.

The ORR measurements conducted in 0.1 M KOH, revealed the MnCo_2O_4 catalyst as the one with the highest current density. The highest overpotential in 0.1 M KOH have CoMn_2O_4 (M1) and the Vulcan XC72. The current density of all three catalysts was around 2 mA/cm^2 for the lower catalyst loading, whereas Vulcan XC72 showed a much lower current density. Concerning the higher catalyst loading, the current density is between 2 and 2.75 mA/cm^2 . For the comparison between the first and fifth sweep, the same behaviour as for the OER can be observed. The current density decreases and the overpotential increases with increasing sweep number. In 8 M KOH, the highest current density was obtained from CoMn_2O_4 (M2) at the lower catalyst loading and at the higher one, MnCo_2O_4 (M2) surpassed the others. The peaks obtained at -0.1 V and -0.4 V in 8 M KOH can be referred to the Vulcan XC72 and the production of H_2O_2 at the glassy carbon electrode, respectively. In 8 M KOH, much lower current densities than in 0.1 M KOH were obtained, due to the lower solubility of oxygen.

The ORR voltammograms at different rotation rates, which were conducted for the analysis of the Koutecky-Levich plots, showed almost equidistant limiting current densities in 0.1 M KOH. In the higher electrolyte concentration, this behaviour was no longer observable for all catalysts. The result of the Koutecky-Levich analysis indicated kinetically limited processes. In 0.1 M KOH, the calculated number of transferred electrons of all catalysts lies in the range of 3.3 to 3.6, which assumes that the ORR is a four-electron process. In the case of 8 M KOH, the amount of transferred electrons is in the range of 0.5 to 0.9 and a two-electron process is more likely. The best catalyst for the ORR in 0.1 M KOH is CoMn_2O_4 (M2), which transferred 3.59 electrons. In 8 M KOH, MnCo_2O_4 (M2) transferred the highest amount of electrons.

6 References

- (1) Li, Y.; Dai, H. Recent Advances in Zinc-Air Batteries. *Chemical Society Reviews*. 2014, pp 5257–5275.
- (2) Guney, M. S.; Tepe, Y. Classification and Assessment of Energy Storage Systems. *Renew. Sustain. Energy Rev.* **2017**, 75 (November 2016), 1187–1197.
- (3) Wang, Z. L.; Xu, D.; Xu, J. J.; Zhang, X. B. Oxygen Electrocatalysts in Metal-Air Batteries: From Aqueous to Nonaqueous Electrolytes. *Chem. Soc. Rev.* **2014**, 43 (22), 7746–7786.
- (4) Alotto, P.; Guarnieri, M.; Moro, F. Redox Flow Batteries for the Storage of Renewable Energy: A Review. *Renew. Sustain. Energy Rev.* **2014**, 29, 325–335.
- (5) Dusastre, V.; Arciό, A. S.; Bruce, P.; Scrosati, B.; Tarascon, J.-M.; Van Schalkwijk, W. Nanostructured Materials for Advanced Energy Conversion and Storage Devices. *Mater. Sustain. Energy* **2012**, 4 (May), 148–159.
- (6) Rahman, M. A.; Wang, X.; Wen, C. High Energy Density Metal-Air Batteries: A Review. *J. Electrochem. Soc.* **2013**, 160 (10), A1759–A1771.
- (7) Caramia, V.; Bozzini, B. Materials Science Aspects of Zinc-Air Batteries: A Review. *Mater. Renew. Sustain. Energy* **2014**, 3 (2).
- (8) Väyrynen, A.; Salminen, J. Lithium Ion Battery Production. *J. Chem. Thermodyn.* **2012**, 46, 80–85.
- (9) Mainar, A. R.; Leonet, O.; Bengoechea, M.; Boyano, I.; Meatza, I. de; Kvasha, A.; Guerfi, A.; Blazquez, J. A. Alkaline Aqueous Electrolytes for Secondary Zinc-Air Batteries: An Overview. *Int. J. Energy Res.* **2016**, 40, 1032–1049.
- (10) Fu, J.; Cano, Z. P.; Park, M. G.; Yu, A.; Fowler, M.; Chen, Z. Electrically Rechargeable Zinc–Air Batteries: Progress, Challenges, and Perspectives. *Adv. Mater.* **2017**, 29 (7).
- (11) Cheng, F.; Shen, J.; Peng, B.; Pan, Y.; Tao, Z.; Chen, J. Rapid Room-Temperature Synthesis of Nanocrystalline Spinel as Oxygen Reduction and Evolution Electrocatalysts. *Nat. Chem.* **2011**, 3 (1), 79–84.
- (12) Menezes, P. W.; Indra, A.; Sahraie, N. R.; Bergmann, A.; Strasser, P.; Driess, M. Cobalt-Manganese-Based Spinel as Multifunctional Materials That Unify Catalytic Water Oxidation and Oxygen Reduction Reactions. *ChemSusChem* **2015**, 8 (1), 164–167.
- (13) Hamlen, R. P.; Atwater, T. B. Metal/Air Batteries. In *Handbook of Batteries*; Linden,

- D., Reddy, T. B., Eds.; McGraw-Hill, 2002; pp 38.1-38.51.
- (14) Dahlquist, E. Nonorganic and Fossil Resources: Known and Estimated Resources. In *Natural Resources Available Today and in the Future*; Dahlquist, E., Hellstrandt, S., Eds.; Springer International Publishing: Cham, 2017; pp 180–206.
- (15) Lee, J. S.; Kim, S. T.; Cao, R.; Choi, N. S.; Liu, M.; Lee, K. T.; Cho, J. Metal-Air Batteries with High Energy Density: Li-Air versus Zn-Air. *Adv. Energy Mater.* **2011**, *1* (1), 34–50.
- (16) Girishkumar, G.; McCloskey, B.; Luntz, A. C.; Swanson, S.; Wilcke, W. Lithium-Air Battery: Promise and Challenges. *J. Phys. Chem. Lett.* **2010**, *1* (14), 2193–2203.
- (17) Linden, D. Basic Concepts. In *Handbook of Batteries*; Linden, D., Reddy, T. B., Eds.; McGraw-Hill, 2002; pp 1.3-1.18.
- (18) Chawla, N. Recent Advances in Air-Battery Chemistries. *Mater. Today Chem.* **2019**, *12*, 324–331.
- (19) Omondi, S. List of Countries by Zinc Production <https://www.worldatlas.com/articles/list-of-countries-by-zinc-production.html> (accessed Jul 15, 2019).
- (20) Cheng, F.; Chen, J. Metal-Air Batteries: From Oxygen Reduction Electrochemistry to Cathode Catalysts. *Chem. Soc. Rev.* **2012**, *41* (6), 2172–2192.
- (21) Yang, D.; Zhang, L.; Yan, X.; Yao, X. Recent Progress in Oxygen Electrocatalysts for Zinc-Air Batteries. *Small Methods* **2017**, *1700209* (i), 1700209.
- (22) Si, F.; Zhang, Y.; Yan, L.; Zhu, J.; Xiao, M.; Liu, C.; Xing, W.; Zhang, J. Electrochemical Oxygen Reduction Reaction. In *Rotating Electrode Methods and Oxygen Reduction Electrocatalysts*; Elsevier B.V., 2014; pp 133–170.
- (23) Bragg W. H. The Structure of Magnetite and Spinels. *Nature* **1915**, *95*, 561.
- (24) Meyer, H.-J. Festkörperchemie. In *Riedel Moderne Anorganische Chemie*; Meyer, H.-J., Ed.; De Gruyter, 2012; pp 315–319.
- (25) Zhao, Q.; Yan, Z.; Chen, C.; Chen, J. Spinels: Controlled Preparation, Oxygen Reduction/Evolution Reaction Application, and Beyond. *Chem. Rev.* **2017**, *117* (15), 10121–10211.
- (26) Sickafus, K. E.; Wills, J. M.; Grimes, N. W. Structure of Spinel. *J. Am. Ceram. Soc.* **1999**, *82* (12), 3279–3292.
- (27) Inkson, B. J. Scanning Electron Microscopy (SEM) and Transmission Electron Microscopy (TEM) for Materials Characterization. In *Materials Characterization Using Nondestructive Evaluation (NDE) Methods*; Elsevier Ltd, 2016; pp 17–43.

- (28) Henning, S.; Adhikari, R. Scanning Electron Microscopy, ESEM, and X-Ray Microanalysis. In *Microscopy Methods in Nanomaterials Characterization*; 2017; pp 1–30.
- (29) Egerton, R. F. *Physical Principles of Electron Microscopy*; Springer, New York, NY, 2005.
- (30) Pereira-da-silva, M. D. A.; Ferri, F. A. Scanning Electron Microscopy. In *Nanocharacterization Techniques*; Elsevier Inc., 2017; pp 1–35.
- (31) Epp, J. X-Ray Diffraction (XRD) Techniques for Materials Characterization. In *Materials Characterization Using Nondestructive Evaluation (NDE) Methods*; Elsevier Ltd, 2016; pp 81–124.
- (32) Massa, W. *Kristallstrukturbestimmung 8. Auflage*; 2015.
- (33) Dinnebier, R. E.; Billinge, S. J. L. *Powder Diffraction: Theory and Practice*; RSC Publishing, 2008.
- (34) Lamas, D. G.; Neto, M. D. O.; Kellermann, G.; Craievich, A. F. X-Ray Diffraction and Scattering by Nanomaterials. In *Nanocharacterization Techniques*; Elsevier Inc., 2017; pp 111–182.
- (35) Thommes, M.; Kaneko, K.; Neimark, A. V.; Olivier, J. P.; Rodriguez-Reinoso, F.; Rouquerol, J.; Sing, K. S. W. Physisorption of Gases, with Special Reference to the Evaluation of Surface Area and Pore Size Distribution (IUPAC Technical Report). *Pure Appl. Chem.* **2015**, *87* (9–10), 1051–1069.
- (36) Naderi, M. Surface Area : Brunauer–Emmett–Teller (BET). In *Progress in Filtration and Separation*; 2015; pp 585–608.
- (37) Sing, K. S. W.; Everett, D. H.; Haul, R. A. W.; Moscou, L.; Pierotti, R. A.; Rouquérol, J.; Siemieniewska, T. Reporting Physisorption Data for Gas/Solid Systems with Special Reference to the Determination of Surface Area and Porosity. *Pure Appl. Chem.* **1985**, *57* (4), 603–619.
- (38) Brunauer, S.; Deming, L. S.; Deming, W. E.; Teller, E. On a Theory of the van Der Waals Adsorption of Gases. *J. Am. Chem. Soc.* **1940**, *62* (7), 1723–1732.
- (39) Ramachandran, V. S.; Beaudoin, J. J. *Handbook of Analytical Techniques in Concrete Science and Technology*; Ramachandran, V. S., Beaudoin, J. J., Eds.; Noyes Publications: Ottawa, 2001.
- (40) Storck, S.; Bretinger, H.; Maier, W. F. Characterization of Micro- and Mesoporous Solids by Physisorption. *Appl. Catal.* **1998**, *174*, 137–146.
- (41) Belsorp, User's Manual (BELMaster / BELsim), Ver.2.3.1; 2014.

- (42) Rouquerol, J.; Avnir, D.; Fairbridge, C. W.; Everett, D. H.; Haynes, J. M.; Pernicone, N.; Ramsay, J. D. F.; Sing, K. S. W.; Unger, K. K. Recommendations for the Characterization of Porous Solids (Technical Report). *Pure Appl. Chem.* **1994**, *66* (8), 1739–1758.
- (43) Barrett, E. P.; Joyner, L. G.; Halenda, P. P. The Determination of Pore Volume and Area Distributions in Porous Substances. I. Computations from Nitrogen Isotherms. *J. Am. Chem. Soc.* **1951**, *73* (1), 373–380.
- (44) Zoski, C. G.; Zoski, C. G.; Liu, B. *Handbook of Electrochemistry*; Elsevier B.V.: Amsterdam, The Netherlands, 2007.
- (45) Elgrishi, N.; Rountree, K. J.; McCarthy, B. D.; Rountree, E. S.; Eisenhart, T. T.; Dempsey, J. L. A Practical Beginner's Guide to Cyclic Voltammetry. *J. Chem. Educ.* **2018**, *95* (2), 197–206.
- (46) Wang, J. *Analytical Electrochemistry, Third Edition*; Wiley VCH, 2006.
- (47) Pine Research Instrumentation, I. Modulated Speed Rotator (MSR) User Guide. **2015**, *1* (919).
- (48) Bard, F. *Electrochemical Methods, Fundamentals and Applications*; 2009; Vol. 60.
- (49) Pletcher, D.; Greff, R.; Peat, R.; Peter, L. M.; Robinson, J. *Instrumental Methods in Electrochemistry*; Woodhead Publishing Limited, 2001; Vol. 13.
- (50) González-García, J.; Expósito, E.; Montiel, V.; Nikolic, J.; Iniesta, J. Theoretical Concepts and Applications of a Rotating Disk Electrode. *J. Chem. Educ.* **2009**, *77* (9), 1191.
- (51) Du, C.; Tan, Q.; Yin, G.; Zhang, J. Rotating Disk Electrode Method. In *Rotating Electrode Methods and Oxygen Reduction Electrocatalysts*; Elsevier B.V., 2014; pp 171–198.
- (52) Cheng, F.; Su, Y.; Liang, J.; Tao, Z.; Chen, J. MnO₂-Based Nanostructures as Catalysts for Electrochemical Oxygen Reduction in Alkaline Media. *Chem. Mater.* **2010**, *22* (3), 898–905.
- (53) Zhang, D.; Wu, J. F.; Mao, L. Q.; Okajima, T.; Kitamura, F.; Ohsaka, T.; Sotomura, T. Hydrodynamic Chronocoulometric Estimation of Diffusion Coefficients and Saturated Concentrations of Dioxygen in KOH Solutions. *Indian J. Chem. - Sect. A Inorganic, Phys. Theor. Anal. Chem.* **2003**, *42* (4), 801–806.
- (54) Hsueh, K.-L.; Gonzalez, E. R.; Srinivasan, S. Electrolyte Effects on Oxygen Reduction Kinetics at Platinum: A Rotating Ring-Disc Electrode Analysis. *Electrochim. Acta* **1983**, *28*, 691–697.

- (55) FIZ Karlsruhe. ICSD Databank <https://icsd.fiz-karlsruhe.de/search/basic.xhtml> (accessed Apr 15, 2019).
- (56) Senthil Kumar, S. M.; Soler Herrero, J.; Irusta, S.; Scott, K. The Effect of Pretreatment of Vulcan XC-72R Carbon on Morphology and Electrochemical Oxygen Reduction Kinetics of Supported Pd Nano-Particle in Acidic Electrolyte. *J. Electroanal. Chem.* **2010**, *647* (2), 211–221.
- (57) Tavares, A. C.; Cartaxo, M. A. M.; da Silva Pereira, M. I.; Costa, F. M. Electrochemical Study of Spinel Oxide Systems with Nominal Compositions Ni_{1-x}Cu_xCo₂O₄ and NiCo_{2-y}Cu_yO₄. *J. Solid State Electrochem.* **2003**, *5* (1), 57–67.
- (58) Lima, F. H. B.; Calegario, M. L.; Ticianelli, E. A. Investigations of the Catalytic Properties of Manganese Oxides for the Oxygen Reduction Reaction in Alkaline Media. *J. Electroanal. Chem.* **2006**, *590* (2), 152–160.
- (59) Jin, W.; Du, H.; Zheng, S.; Xu, H.; Zhang, Y. Comparison of the Oxygen Reduction Reaction between NaOH and KOH Solutions on a Pt Electrode: The Electrolyte-Dependent Effect. *J. Phys. Chem. B* **2010**, *114* (19), 6542–6548.
- (60) Yan, W. Y.; Zheng, S. L.; Jin, W.; Peng, Z.; Wang, S. N.; Du, H.; Zhang, Y. The Influence of KOH Concentration, Oxygen Partial Pressure and Temperature on the Oxygen Reduction Reaction at Pt Electrodes. *J. Electroanal. Chem.* **2015**, *741*, 100–108.

7 Appendix

Chemicals

Manganese acetate tetrahydrate ($\text{Mn}(\text{CH}_3\text{COO})_2 \cdot 4 \text{H}_2\text{O}$)

>99%

Merck

Art.-Nr.: A516721, CAS: 638-38-0

Kaliumpermanganate (KMnO_4)

>99%

Riedel-de Haën

Art.-Nr.: 31404, CAS: 7722-64-7

Cobaltous chloride Hexahydrate ($\text{CoCl}_2 \cdot 6 \text{H}_2\text{O}$)

>98%

Art.-Nr.: 60820, CAS: 7646-79-9

Sodium borohydride (NaBH_4)

$\geq 96\%$

Fluka Analytical

Sodiumhydroxide (NaOH)

99.3%

VWR Chemicals

Cobalt acetate tetrahydrate ($\text{C}_4\text{H}_6\text{CoO}_4 \cdot 4 \text{H}_2\text{O}$)

Art.-Nr: 1001383761 CAS: 6147-53-1

Ammonium sulfate (NH₄)₂SO₄

>99.5%

Merck

Art-Nr.: A626617, CAS: 7783-20-2

Ammonium bicarbonate (NH)₄HCO₃

≥99%

Carl Roth GmbH & Co. KG

Art-Nr: T871.2, CAS: 1066-33-7

Carbon Black (VXC72R)

CARBOT

CAS-Nr.: 1333-86-4

Nafion®, perfluorinated resin, aqueous dispersion

10 wt% in H₂O

Aldrich Chemistry

Art.-Nr.: 527114-25ML; CAS-Nr.: 31175-20-9

Potassium Hydroxide (KOH)

≥ 85 % p.a.

Carl Roth GmbH & Co. KG

Art-Nr.: 6781.5; CAS-Nr.: 1310-58-3

Propanol-2 (Isopropanol)

≥ 99.8 % p.a.

Chem-Lab NV

Art-Nr.: CL00.0906.2500; CAS-Nr.: 67-63-0

List of Abbreviations

AE	auger electrons
BSE	backscattered electrons
BET	Brunauer-Emmett-Teller method
BJH	Barrett-Joyner-Halenda method
CV	Cyclic Voltammetry
EDX	Energy dispersive X-ray Diffraction
FEP	fluorinated ethylene propylene
fcc	face centered cubic
GC	glassy carbon
Hg/HgO	Mercury/Mercury oxide
IUPAC	International Union of Pure and Applied Chemistry
IR	infrared
ICSD	Inorganic Crystal Structure Database
LSV	linear sweep voltammetry
n	transferred electrons
OER	Oxygen Evolution Reaction
ORR	Oxygen Reduction Reaction
PTFE	polytetrafluoroethylene
PVDF	polyvinylidene fluoride
RDE	rotating disc electrode
RHE	reversible hydrogen electrode
RT	room temperature
SE	secondary electrons
SEM	Secondary Electron Microscopy
SHE	standard hydrogen electrode
SSA	specific surface area
XRD	X-Ray Diffraction

List of Figures

Figure 1: Comparison of the theoretical energy densities of different secondary battery types with gasoline ^{16, 17, 18}	3
Figure 2: A schematic illustration of the secondary zinc-air battery. ¹⁵	5
Figure 3: A schematic illustration of the performance-limiting phenomena that can occur on the zinc electrode: a) dendrite formation, b) shape change, c) passivation and d) hydrogen evolution. ¹⁰	9
Figure 4: Crystal structure of the CoMn ₂ O ₄ and MnCo ₂ O ₄ catalyst with different octahedral and tetrahedral sites (ICSD ⁵⁵)	11
Figure 5: A schematic illustration of a secondary electron microscope (left) and a scheme of the interaction volume of the primary electrons with the specimen (right) ^{27, 28}	13
Figure 6: A typical EDX spectrum of the CoMn ₂ O ₄ (M2) catalyst.	14
Figure 7: An illustration of the atomic energy levels according to the emission of characteristic X-ray radiation (left) and a schematic illustration of the setup of a X-ray tube (right).....	15
Figure 8: Geometrical illustration for the derivation of the Bragg equation.....	17
Figure 9: X-ray diffractograms of an amorphous material (left) and a crystalline material (right).....	17
Figure 10: The five types of adsorption isotherms according to Brunauer-Emmett-Teller ³⁶	19
Figure 11: Illustration of the meniscus which appears during the capillary condensation ⁴¹ ...	21
Figure 12: A typical pore size distribution graph from samples with different pore sizes. ³⁹ .	23
Figure 13: Potential-time curve of the linear sweep voltammetry (left) and a linear sweep voltammogram of a reversible reaction ($O + ne^- \leftrightarrow R$) (right). ⁴⁸	24
Figure 14: Potential-time signals during a cyclic voltammetry experiment (left) ⁴⁶ and an illustration of a cyclic voltammogram of a reversible reaction (right) ^{44, 49}	25
Figure 15: Illustration of the RDE and the resulting convective stream lines, side view (left) and from below the disc (right) ⁴⁹	27
Figure 16: Voltammograms at different rotation rates acquired with a Pt disk electrode, in O ₂ saturated 0.5 M H ₂ SO ₄ solution, $v = 5$ mV/s ⁵¹	29
Figure 17: ORR Voltammograms at different rotation rates (left) and the Koutecky-Levich plot determined at different potentials (right).	30

Figure 18: The dried amorphous MnO ₂ precursor.	32
Figure 19: MnO ₂ precursor mixed with CoCl ₂ *6 H ₂ O (left), the resulting product after the reduction with NaBH ₄ (right).	33
Figure 20. The synthesis of Co _{0.33} Mn _{0.67} CO ₃ at different stages: a) the mixture at the beginning, containing only Co(CH ₃ COO) ₂ *4 H ₂ O and Mn(CH ₃ COO) ₂ *4 H ₂ O, b) after the addition of (NH ₄) ₂ SO ₄ , c) after 2 h of stirring, d) after the addition of (NH ₄)HCO ₃ , e) after 4h of stirring.	34
Figure 21: The Co _{0.33} Mn _{0.67} CO ₃ precipitate before (a) and (b) after drying at 60°C and (c) after annealing at 400 °C to obtain CoMn ₂ O ₄	35
Figure 22: The catalyst suspension after 30 min of ultrasonically mixing (left) and the drying step of the applied catalyst (right).	38
Figure 23: A schematic illustration of the three-electrode assembly.	39
Figure 24: XRD diffractograms of the three catalysts, CoMn ₂ O ₄ (M1/M2) and MnCo ₂ O ₄ (M2) in comparison with literature data ⁵²	41
Figure 25: SEM images of amorphous MnO ₂ (left) and CoMn ₂ O ₄ (M1, right) at 1.000 fold magnification.	43
Figure 26: SEM images of amorphous MnO ₂ (left) and CoMn ₂ O ₄ (M1, right) at 5.000 fold magnification.	43
Figure 27: SEM images of CoMn ₂ O ₄ (M2, left) and MnCo ₂ O ₄ (M2, right) at 1.000 fold magnification.	44
Figure 28: SEM images of CoMn ₂ O ₄ (M2, left) and MnCo ₂ O ₄ (M2, right) at 20.000 fold magnification.	44
Figure 29: Area of the SEM picture, where the EDX spectrum of the amorphous MnO ₂ (left) and CoMn ₂ O ₄ (M1, right) is taken.	45
Figure 30: Area of the SEM picture, where the EDX spectrum of CoMn ₂ O ₄ (M2, left) and MnCo ₂ O ₄ (M2, right) is taken.	46
Figure 31: The adsorption isotherms of the catalysts and Vulcan XC72.	48
Figure 32: Comparison of the cyclic voltammograms of the three catalysts (c = 0.015 mg) and the pure electrode coated with Vulcan XC72 (c = 0.035 mg), 0.1 M KOH, v = 10 mV/s, cycle 2.	49
Figure 33: Comparison of the cyclic voltammograms of the three catalysts (c = 0.0196 mg) and the pure electrode coated with Vulcan XC72(c = 0.045 mg), 0.1 M KOH, v = 10 mV/s, cycle 2.	50

Figure 34: Cyclic voltammograms of CoMn_2O_4 (M2, $c = 0.0196$ mg), cathodic/anodic sweep only, 0.1 M KOH, $v = 10$ mV/s, 3 cycles.....	50
Figure 35: Comparison of the cyclic voltammograms of the three catalysts ($c = 0.015$ mg) and the pure electrode coated with Vulcan XC72 ($c = 0.035$ mg), 8 M KOH, $v = 10$ mV/s, cycle 2.	51
Figure 36: Comparison of the cyclic voltammograms of the three catalysts ($c = 0.0196$ mg) and the pure electrode coated with Vulcan XC72 ($c = 0.045$ mg), 8 M KOH, $v = 10$ mV/s, cycle 2.	52
Figure 37: OER voltammograms of the three catalysts ($c = 0.015$ mg) and Vulcan XC72 ($c = 0.035$ mg), 0.1 M KOH, $v = 5$ mV/s, 1600 rpm, Sweep 5.	54
Figure 38: OER voltammograms of the three catalysts ($c = 0.0196$ mg) and Vulcan XC72 ($c = 0.045$ mg), 0.1 M KOH, $v = 5$ mV/s, 1600 rpm, Sweep 5.	54
Figure 39: OER voltammograms of the catalysts and Vulcan XC72 at different catalyst loadings in 0.1 M KOH, $v = 5$ mV/s, 1600 rpm, Sweep 5.....	55
Figure 40: Comparison of the OER voltammograms of the first and fifth Sweep of the three catalysts ($c = 0.0196$ mg) in 0.1 M KOH, at the 1st and 5th Sweep at 1600 rpm, $v = 5$ mV/s.	55
Figure 41: OER voltammograms of the three catalysts ($c = 0.0196$ mg) at different rotation rates, 0.1 M KOH, $v = 5$ mV/s, Sweep 5 (1600 rpm) and Sweep 6 (400 rpm).	56
Figure 42: OER voltammograms of the three catalysts ($c = 0.015$ mg) and Vulcan XC72 ($c = 0.035$ mg), 8 M KOH, $v = 5$ mV/s, 1600 rpm, Sweep 5.	56
Figure 43: OER voltammograms of the three catalysts ($c = 0.0196$ mg) and Vulcan XC72 ($c = 0.045$ mg), 8 M KOH, $v = 5$ mV/s, 1600 rpm, Sweep 5.	57
Figure 44: OER voltammograms of the catalysts and Vulcan XC72 at different loadings, 8 M KOH, $v = 5$ mV/s, 1600 rpm, Sweep 5.	57
Figure 45: Comparison of the OER voltammograms of the catalysts ($c = 0.0196$ mg), in different electrolyte concentrations, $v = 5$ mV/s 1600 rpm, Sweep 5.	58
Figure 46: Comparison of the OER voltammograms first and fifth Sweep of the three catalysts ($c = 0.0196$ mg), in 8 M KOH, $v = 5$ mV/s, 1600 rpm.	58
Figure 47: OER voltammograms of the three catalysts ($c = 0.0196$ mg) at different rotation rates, 8 M KOH, $v = 5$ mV/s, Sweep 5 (1600 rpm) and Sweep 6 (400 rpm).	59
Figure 48: ORRs voltammograms of the catalysts ($c = 0.015$ mg) in comparison with Vulcan XC72 ($c = 0.035$ mg), 0.1 M KOH, $v = 5$ mV/s 1600 rpm, Sweep 5.	60

Figure 49: ORR voltammograms of the catalysts ($c = 0.0196$ mg) in comparison with Vulcan XC72 ($c = 0.045$ mg), 0.1 M KOH, $v = 5$ mV/s, 1600 rpm, Sweep 5.	61
Figure 50: ORR voltammograms of the catalysts and Vulcan XC72 with different loadings, 0.1 M KOH, $v = 5$ mV/s, 1600 rpm, Sweep 5.	61
Figure 51: Comparison of the ORR voltammograms of the three catalysts ($c=0.0196$ mg) of the first and fifth sweep at 1600 rpm, 0.1 M KOH $v = 5$ mV/s.	62
Figure 52: ORR voltammograms for Koutecky–Levich plot, CoMn_2O_4 (M1 (left) and M2 (right)) ($c = 0.0196$ mg), 0.1 M KOH, $v = 5$ mV/s.	63
Figure 53: ORR voltammograms for Koutecky–Levich plot, MnCo_2O_4 ($c = 0.0196$ mg, left) and Vulcan XC72 ($c = 0.035$ mg, right), 0.1 M KOH, $v = 5$ mV/s.....	63
Figure 54: ORR voltammograms of the three catalysts ($c = 0.015$ mg) compared to Vulcan XC72 ($c = 0.035$ mg) and the pure glassy carbon disc, 8 M KOH, $v = 5$ mV/s, 1600 rpm, Sweep 5.	64
Figure 55: ORR voltammograms of the three catalysts ($c = 0.0196$ mg) compared to Vulcan XC72 ($c = 0.045$ mg) and to the pure glassy carbon disc, 8 M KOH, $v = 5$ mV/s, 1600 rpm, Sweep 5.	65
Figure 56: ORR voltammograms of the catalysts and Vulcan XC72 with different loadings, 8 M KOH, $v = 5$ mV/s, 1600 rpm, Sweep 5.....	65
Figure 57: Comparison of the ORR voltammograms of the three catalysts ($c = 0.0196$ mg) of the second and fifth sweep, 8 M KOH, $v = 5$ mV/s, 1600 rpm.....	66
Figure 58: Comparison between the catalysts and the electrolyte concentration, $c = 0.0196$ mg, $v = 5$ mV/s, 1600 rpm, Sweep 5.....	66
Figure 59: ORR voltammograms for the Koutecky–Levich plot, CoMn_2O_4 (M1) ($c = 0.0196$ mg, left), CoMn_2O_4 (M2) ($c = 0.0196$ mg, right), 8 M KOH, $v = 5$ mV/s.....	67
Figure 60: ORR voltammograms for the Koutecky–Levich plot, MnCo_2O_4 (M2) ($c = 0.0196$ mg), 8 M KOH, $v = 5$ mV/s.	67
Figure 61: Koutecky-Levich Plot of CoMn_2O_4 (M1) ($c=0.0196$ mg) (left) and CoMn_2O_4 (M2) ($c=0.0196$ mg) (right), 0.1 M KOH, $v = 5$ mV/s.....	69
Figure 62: Koutecky-Levich Plot of MnCo_2O_4 (M2) ($c=0.0196$ mg) (left) and Vulcan XC72 ($c=0.035$ mg) (right), 0.1 M KOH, $v = 5$ mV/s.....	69
Figure 63: Comparison of the Koutecky-Levich Plots of the three catalysts in 0.1 M KOH, $v = 5$ mV/s.	70

Figure 64: Koutecky-Levich Plot of CoMn_2O_4 (M1, (left)) and MnCo_2O_4 (M2,right), $c = 0.0196$ mg, 8 M KOH, $v = 5$ mV/s.....	71
Figure 65: Comparison of the Koutecky-Levich Plots from the two catalysts in 8 M KOH, $v = 5$ mV/s.	71

List of Tables

Table 1: The composition of the catalyst suspensions.	38
Table 2: The used values for the calculation of the transferred electrons.....	40
Table 3: Lattice constants of the catalysts CoMn_2O_4 (M1/M2) and MnCo_2O_4 (M2) compared to ICSD ⁵⁵ and literature ^{11,12}	42
Table 4: The mean value of the chemical composition (at.%) of MnO_2 and the catalysts.	46
Table 5: The mean values of the chemical composition (wt.%) of MnO_2 and the catalysts....	46
Table 6: The chemical ratios of the three catalysts and of the amorphous MnO_2 precursor....	46
Table 7: Specific surface area (SSA) compared with the literature and the results of the BJH analysis.	47
Table 8: The number of transferred electrons in 0.1 M KOH, calculated from the Koutecky-Levich Plot.	68
Table 9: The number of transferred electrons in 8 M KOH, calculated from the Koutecky-Levich Plot.	70